DELFT UNIVERSITY OF TECHNOLOGY
FACULTY: CIVIL ENGINEERING AND GEOSCIENCES

MSC THESIS PROJECT
AESM7000

ASSESSING THE POTENTIAL FOR NON-WELL BORE RECHARGE: THE ROLE OF STRATIGRAPHIC ARCHITECTURE AND CONNECTIVITY ON CROSS FLOW NEAR THE B WELL BORE

Author:
Tim van Eijck (5864453)

August 12, 2025

Abstract

This thesis explores whether vertical stratigraphic cross flow from the A zone to the C1 zone of the Upper Slochteren Member can occur without wellbore crossflow, and under what conditions such recharge is plausible. The study focuses on the B-well in the L-field, Dutch offshore North Sea, where production resumed after a shut-in period, and pressure behavior suggested possible recharge. Four different basecase models were constructed using Rapid Reservoir Modeling (RRM), each representing a different degree of vertical connectivity across the B zone. These models were then transferred to Computer Modeling Group (CMG) software, where dynamic multiphase simulations were performed to assess gas flow between the zones of the Upper Slochteren Member.

The results show that stratigraphic recharge from A to C1 is possible, but highly sensitive to the internal architecture of the B zone. Increased vertical connectivity across the B zone consistently show earlier pressure communication and higher gas fluxes into the C1 zone. Sensitivity analyses were conducted on porosity, vertical permeability, and gas relative permeability to test their influence on flow behavior. These parameters affected not only the rate of gas migration, but also the degree of pressure redistribution across the model, which influences the gas rates even further. Capillary pressure and water saturation were also found to control gas mobility, particularly in low-permeability or heterolithic intervals. The findings do not fully support the hypothesis that stratigraphic recharge explains the observed pressure response in the reservoir, but suggest it may account for part of it. Additionally, the results emphasize the importance of considering vertical heterogeneity and capillary forces when evaluating near-wellbore connectivity.

Acknowledgment

First, I would like to thank my daily supervisor at ONE-Dyas, Nordin Tippersma, for his support throughout the entire process of my thesis. His guidance and feedback not only helped me bring this thesis to its current form, but also taught me to approach my work in a different and more effective way. Secondly, I want to thanks Dinesh and Maazen for their thoughts and opinions on my thesis and all the laughs we had at the office. I would also like to thank Gerlof Visser for giving me the opportunity to conduct my research at ONE-Dyas. In addition, I am grateful to all other colleagues at ONE-Dyas, not only for their assistance, but also for the many enjoyable moments during my time there. In particular, I would like to thank Peter Matev for his help in providing access to all necessary data and feedback and Barry, Thijs and Clare for their constructive feedback.

I would also like to thank my two supervisors from TU Delft, Allard Martinius and Sebastian Geiger. Without their guidance and feedback, it would not have been possible to deliver this thesis in its current form. The effort that both supervisors have invested in me is greatly appreciated, and I would wholeheartedly recommend this duo to any other student looking for thesis guidance. In addition, I would like to thank Mathias Erdtmann for his help with CMG.

Finally, I would like to thank my mother and my family for their constant support, both direct and indirect, which has meant more to me than words can express.

To everyone who contributed in any way to this project: thank you.

Contents

List of Abbreviations

CCS = Carbon Capture and Storage
SPB = South Permian Basin
SNSB = Southern North Sea Basin
BPU = Base Permian Unconformity
PLT = Production Logging Tool
RRM = Rapid Reservoir Modelling
N:G = net-to-gross
N = North
S = South
W = West
E = East
Kv = Vertical permeability
Kh = Horizontal permeability
SBIM = Sketch-Based Interface Modeling
SSTVD = Sea-Level True Vertical Depth CMG = Computer Modeling Group
SW = Water Saturation
Pc = Capillary Pressure
Sgr = Residual gas Saturation
Krg = Relative gas permeability

List of Figures

1 Introduction

The Upper Slochteren member, consisting of the A, B, C1, C2 and C3 zones, of the Rotliegend Group in the Dutch North Sea is known for its good reservoir quality, characterized by relatively good porosity and permeability. This makes it an attractive target not only for hydrocarbon production but also for future subsurface applications, such as CO_2 and hydrogen storage and/or geothermal systems ([Grötsch et al., 2011, van Uijen, 2013, Kombrink and Patruno, 2020, Mijnlieff, 2020, Doornenbal et al., 2010, Ziegler, 1990]). However, due to the high complexity of the Upper Slochteren depositional architecture and heterogeneity, flow pathways within the Upper Slochteren are not fully understood. This limits predictive capabilities and affects the efficiency of (future) subsurface operations.

The B well, operated by ONE-Dyas, is a gas producing well and exemplifies these complexities and highlights the intricate relationship between geological heterogeneity and structural controls on subsurface connectivity influencing flow migration. The B well is the focus of this thesis. The B well was in production from 1995 to 2009 and resumed production in 2021. Since recommencing production, the well has been producing intermittently which was not expected after such a short period. Based on internal investigations and back-of-the-envelope calculations, ONE-Dyas hypothesized that that the A-zone is recharging the C1 and C3 zones via crossflow through the wellbore. While recharge occurring solely through the well via crossflow is a plausible scenario, an alternative explanation is that the C1 and C3 zones are recharged by the A-zone via stratigraphic connectivity within the Upper Slochteren member itself: vertical flow pathways formed by connected elements. Additionally, a combination of both migration pathways cannot be ruled out.

This thesis therefore tests the hypothesis that recharge from the A-zone to the C1 and C3 zones occurs via stratigraphical vertical cross flow, independently of crossflow through the wellbore. Additionally, a sensitivity analysis on reservoir parameters will be done to investigate how stratigraphical cross flow can be enhanced and in which situations stratigraphical cross flow is plausible. To assess this, the following research questions will be addressed:

Main question

How do different architectural connectivity scenarios between the Upper Slochteren zones and reservoir parameters influence vertical cross flow in the near wellbore area?

Sub-questions

- What are the sedimentological and stratigraphical characteristics of the Upper Slochteren zones in the B well area?

- Which factors influence the reservoir quality and how do they affect connectivity?

- How does the number and spatial configuration of vertical connectivity zones affect flow behavior?

- How do parameters, such as vertical permeability, porosity, capillary pressures and water saturation determine the possibility of stratigraphical cross flow?

- Which parameters enhance vertical cross flow?

- Can the recharge of the C1- and C3-zones from the A-zone be explained by stratigraphical vertical cross flow?

These questions will be addressed using a combination of conceptual modeling and flow simulation. First, architectural models representing various connectivity scenarios will be constructed in Rapid Reservoir Modeling (RRM). These models will then be transferred to CMG, where dynamic simulations are performed to evaluate flow behavior. The simulation results will serve as the basis for testing the proposed hypothesis. The study will focus on a reasonable timescale to enable comparison with the effects of the 10 year shut-in period.

1.1 Area of Interest

The SPB stretches east-west from Poland to England and N-S from Denmark to Belgium. This basin can be divided into three main sub-basins: the Anglo-Dutch, North German, and Central Polish basins ([Doornenbal et al., 2010] (figure 1).

Figure 1: The Southern Permian Basin, which stretches East-West from Poland to England and N-S from Denmark to Belgium ([Doornenbal et al., 2010])

The Anglo-Dutch Basin, also known as the Southern North Sea Basin (SNSB), includes the Mid North Sea High and spans a large part of the Dutch sector. The SNSB in the Dutch area is divided into multiple regions, each designated by a letter, such as A, B, E, F, G, K, L, M, P, Q and S (figure 2). Within some areas, wells have been drilled for the exploration of hydrocarbons. However, these wells not only provide crucial information on hydrocarbon systems, but also offer valuable data to investigate the potential of the subsurface for future energy applications, such as CO_2 and hydrogen storage or geothermal energy. The B well, located in region L, is such a well and data from this specific well is used for this research.

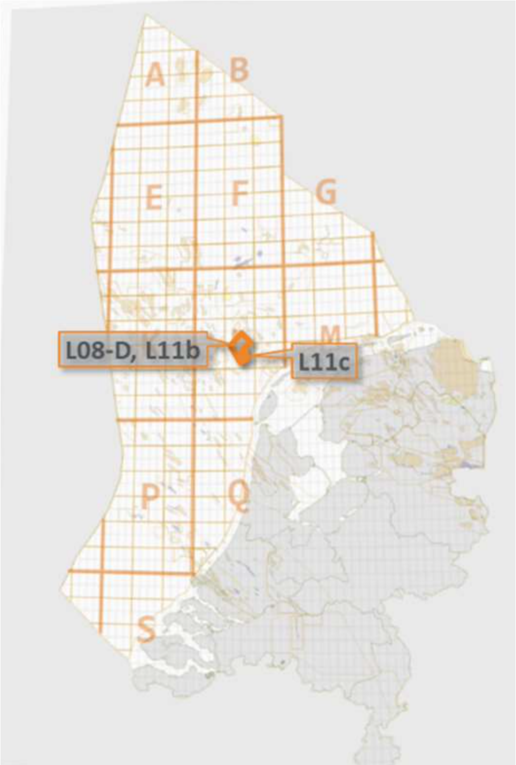

Figure 2: Overview of the Dutch North Sea and its sections. Indicated with orange and grey, the location of the L11b platform. From ONE-Dyas

2 Structural and Stratigraphical history

To accurately develop the architecture of the sandstones within the Slochteren Formation, it is important to get an understanding of the deformation and stratigraphical history of the area. Reservoir connectivity is influenced by multiple factors, including faulting, permeability and stratigraphy. Faults play a critical role in shaping both the connectivity and permeability of reservoirs ([Larue and Hovadik, 2006, Xue et al., 2021, Doornenbal et al., 2010, Trevena, 1989]). Fault zones can have contrasting effects on permeability; they may act as barriers that reduce flow by significantly lowering the permeability of sandstone layers, thereby negatively impacting reservoir connectivity ([Busch et al., 2019a, Trevena, 1989, Busch et al., 2019b]). Conversely, faults can enhance permeability by creating critical flow pathways that facilitate fluid migration, thereby improving connectivity in gas-bearing sandstones ([Lyu et al., 2017]). It's of great importance to get an idea of the stratigraphical SNSB infill to better understand and predict connectivity scenarios. Porosity and permeability are both important lithology characteristics which influence the degree of connectivity and fluid/gas flow within the reservoirs ([Wang et al., 2021]).

2.1 Tectonic Events

The SPB is marked by five main tectonic events which shaped the overall structure of the basin: The Caledonian Orogeny, the Variscan Orogeny, the post-Variscan Orogeny, Pangea break-up and the Alpine Orogeny. The five tectonic events together with the overall stratigraphy can be tracked in figure 3.

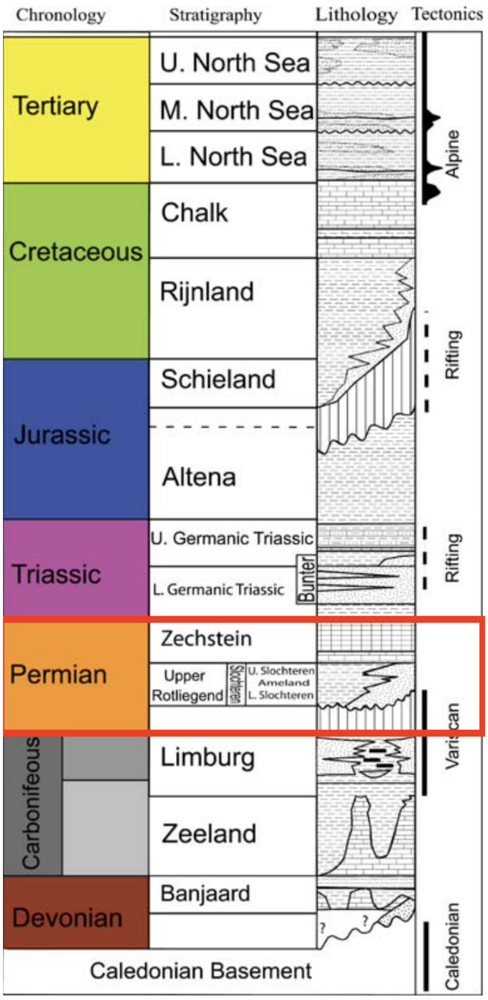

Figure 3: Tectono-stratigraphical chart for the Netherlands. The Permian stratigraphy, which contains the Upper Rotliegend Group and is the main focus of this research, is embodied in red. Modified from [De Jager, 2007].

The Caledonian Orogeny is characterized by the closure of the Iapeltus Ocean, separating Baltica and Avalonia from Laurentia, and the Tornquist Ocean, separating Avalonia and Baltica (figure 4) ([Simon et al., 2019]). The Caledonian Orogeny occurred around 455 million years ago and formed Caledonian orogenic belt, characterized by NW-SE and NE-SW trending strike-slip and thrust faults ([Gee et al., 2008, Haaland, 2018]). These structures influenced the subsequent geological framework of the North Sea region.

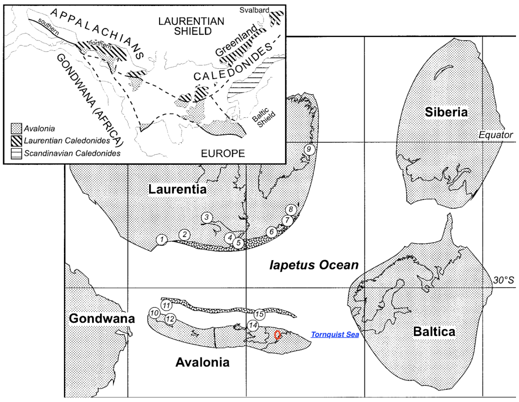

Figure 4: Schematic representation of the continents and its separating oceans/seas during the Caradoc (c. 455ma). The red dot indicated the location of the study area. Modified from [McKerrow et al., 2000].

Following the Caledonian Orogeny, the closure of the Rheic Ocean due to the convergence of Laurussia and Gondwana resulted in the Variscan Orogeny, culminating in the formation of Pangea ([Ziegler, 1982, Ziegler, 1990, Borgh et al., 2018, Horn et al., 2021]). This led to an extensional regime in the Southern North Sea, forming linked half-grabens controlled by inherited Caledonian structures ([Fraser and Gawthorpe, 1990, Coward, 1993]).
As compression exceeded extension in the Late Carboniferous, inversion structures formed, and fault-controlled subsidence dominated, marking the Post-Variscan Orogeny phase. The Base Permian Unconformity (BPU) developed due to thermal uplift in the Southern North Sea Area ([Ziegler, 1982, Ziegler et al., 2004, Doornenbal et al., 2010, Borgh et al., 2018, Lauwerier, 2021]). The BPU consisted of multiple unconformities creating a 40-60myr hiatus between the Carboniferous and Permian rocks ([Geluk et al., 2007, Borgh et al., 2018]). Subsequent thermal subsidence led to extensive Rotliegend sedimentation ([Gaupp and Okkerman, 2011]). The Rotliegend was deposited following the Late Carboniferous - Early Permian transition, during which extensional tectonics dominated the SNSB. Thermal uplift and subsidence influenced fault-controlled basins, with NW-SE trending normal faults and inherited Variscan structures shaping the basin's architecture ([Ziegler, 1982, Pharaoh et al., 2010, Borgh et al., 2018]). Due to extensional faulting in the SNSB, rotational fault blocks could arise. Later Triassic rifting reactivated these structures, causing block faulting and sedimentary differentiation ([Gaupp and Okkerman, 2011]). In the Upper Slochteren in the L11 field, a tilted fault block is observed ([Gras et al., 2016]). The Rotliegend sediments marked the Permian stratigraphy and will be discussed in the Rotliegend subchapter.

The Post-Variscan Orogeny is followed up by the break-up of Pangea. During the Jurassic, rifting intensified across the North Sea resulting in the break-up of Pangea during Middle Jurassic times. However, in the SNSB, this period was characterized by a period of relative tectonic stability ([Pharaoh et al., 2010, Lott et al., 2010]). The main tectonic structures of the SNSB developed during the Late Jurassic-Early Cretaceous, with Cimmerian rifting driving north-to-south extensional faulting and subsidence ([Heybroek, 1975, Schroot, 1991]). Intensified rift extension led to thermal doming in the region, triggering renewed movement along NW-SE trending faults ([Gaupp and Okkerman, 2011]).

The tectonic patterns established during the Jurassic were followed until the Late Creatceous. The tectonic regime change resulted in Alpine Orogeny During the Late Cretaceous, where tectonic activity shifted with the onset of subduction and seafloor spreading. This introduced compressional stresses in the SPB area with NW-SE oriented strike slip faulting, resulting in inversion, uplift, folding and reactivation of faults formed during earlier tectonic events ([Gaupp and Okkerman, 2011]). The Alpine Orogeny is the last tectonic event that shaped the area. The stresses of the Alpine Orogeny reshaped the Southern North Sea Basin (SNSB) causing alternating uplift and subsidence ([Ziegler, 1990, Knox et al., 2010]).

2.2 Rotliegend

The Permian stratigraphy is marked by the Rotliegend. The depositional environment of the Rotliegend varied widely, encompassing aeolian dunes and interdunes, dry sandflats with sheetflood deposits, damp sandflats and wadis, wet sandflats, and eventually transitioning to mudflats and playa-lake deposits ([Gaupp and Okkerman, 2011]). The Rotliegend consist of three groups: Lower Rotliegend, volcanics and Upper Rotliegend I and II ([Gast et al., 2010]). In this thesis, the terms "Upper Rotliegend," "Rotliegend Group," or simply "Rotliegend" will specifically refer to the Upper Rotliegend Group II, as the Lower Rotliegend Group and Upper Rotliegend I are not present in the SNSB ([Gast et al., 2010]). The Upper Rotliegend has been deposited following climatically forced cycles and the cyclicity is primary driven by fluctuation in base-level or lake-level ([Gast et al., 2010]). The Upper Rotliegend is primary made up of a mix of fluvial and aeolian sandstones and playa sediments. The Upper Rotliegend consist of the Slochteren and Silverpit Formation. The Slochteren Formation consist of the Lower and Upper Slochteren Members ([Witmans et al., 2010, De Jong et al., 2020])(figure 3). The Slochteren Formation has been deposited in in environments ranging from aeolian dunes and sandflats to fluvial systems ([Geluk, 2005, Donselaar et al., 2011]). The Slochteren Formation varies from playa mudflats and sandflats with aeolian dune deposits to sandstones and conglomerates of fluvial and aeolian origin [Geluk, 2005, De Jong et al., 2020, De Jong et al., 2019, Donselaar et al., 2011]). The Silverpit Formation consist of claystones, siltstones, and extensive evaporites-rich lake deposits and is subdivided into three members corresponding to these three compositions ([De Jong et al., 2019, Donselaar et al., 2011, De Jong et al., 2020]). In the study area the Slochteren Formation serves as a great reservoir due to its well-developed characteristics. The stratigraphic variability of the Slochteren formation plays a crucial role in fluid migration pathways, with implications for applications such as carbon capture and storage (CCS), geothermal energy, and gas exploration. For this study, the sandstones of the Upper Slochteren member will be the main target.

3 Conceptual Model

To interpret and develop a scientific robust depositional model and determine its flow migration, geological characteristics and layers of the B well should be determined in a conceptual model. This conceptual model provides the foundation for reconstructing the depositional history of the Upper Slochteren Member and serves as a framework for subsequent reservoir characterization. In the conceptual model, the depositional environments of the different zones are determined based on well correlation and related studies. It establishes a structured approach to identifying facies distributions, sedimentary structures, and architectural elements, ensuring a systematic interpretation of reservoir heterogeneity. Additionally, the conceptual model acts as a bridge between geological observations and modeling in RRM, ensuring consistency in facies interpretations. Certain sedimentary structures occur exclusively in specific depositional environments and exhibit location-specific characteristics such as thickness, length, and size. These structures provide insights into sediment transport processes, flow energy, and depositional settings, facilitating an understanding of the primary sedimentological controls on reservoir quality. The depositional environment determines the primary depositional texture (grain size, sorting, bedding, and more) and controls the initial porosity and permeability of the facies ([Bell et al., 2018]). These primary textures not only influence initial reservoir properties but also dictate the degree of subsequent diagenetic alteration, playing a key role in determining reservoir quality ([Li et al., 2023]). Therefore, accurate facies classification and depositional environment characterization are fundamental to predicting reservoir connectivity and flow migration.

3.1 Area

The depositional environment system of the Rotliegend during the Permian in the Dutch North Sea area is interpreted as a continental arid to semi-arid system with fluvial, aeolian and lacustrine settings ([Felder, 2010])(figure 5). The system contained a fluvial plain, ergs, ergs margins in the south and a playa margin, playa and a lake in the north (figure 5).

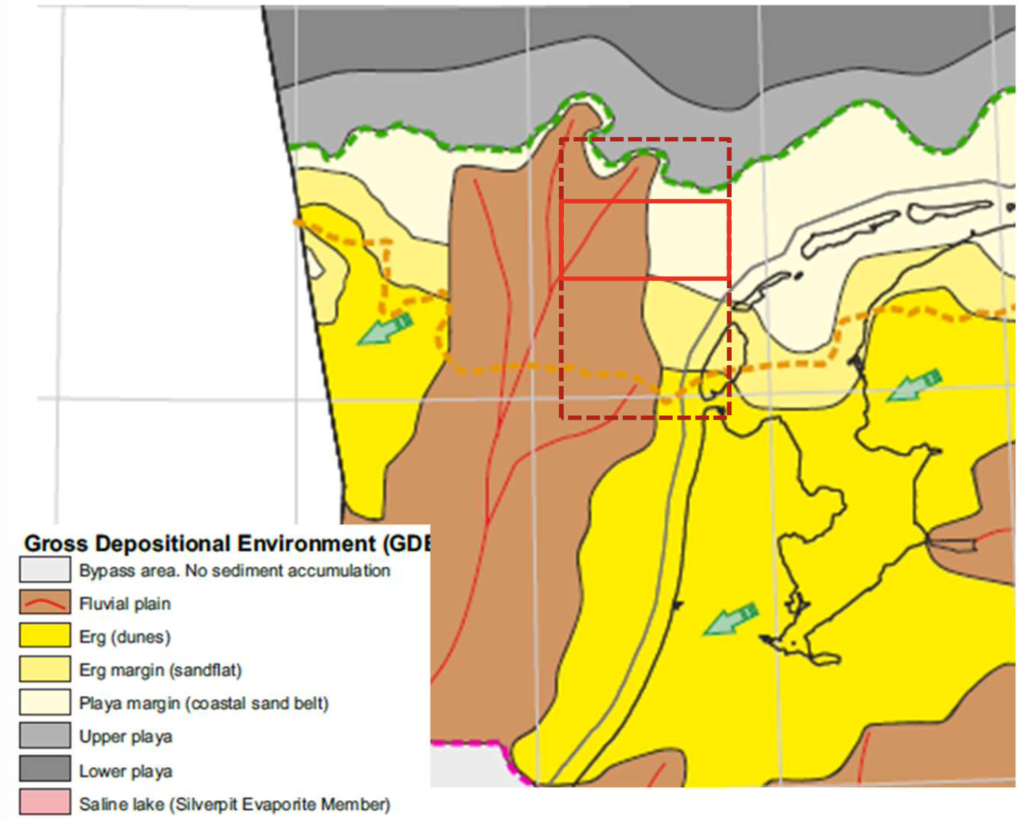

Figure 5: Overview of the depositional environments of the Netherlands and North Sea during Slochteren depositions times (from: [Felder, 2024]).

The Slochteren Formation represents a fluvially dominated succession, deposited in a fluvial environment, and the study area is located to the east of the fluvial axis ([Felder, 2024]) (figure 5). The area in which the B well is located, is part of the terminal fan in the northern fluvial plain ([Felder, 2024, Felder, 2010]). Within a terminal fan, the properties of architectural elements differ due to proximal-distal changes resulting in sedimentary differences influencing reservoir quality. Proximal areas tend to be dominated by coarser-grained, amalgamated channel bodies with high net-to-gross ratios, whereas distal environments exhibit more heterogeneity due to increased fine-grained sediment input and periodic flooding events ([Fisher et al., 2008]). The study of [Felder, 2024] showed that the proximal-distal changes of the terminal fan are gradual but systematic and include changes in sediment/water ratios, sand/shale ratios, dimensions and grain size. To further analyze these proximal-distal changes, a sedimentological analogue will be used with the Lake Eyre basin in Australia. The principle of Uniformitarianism provides a methodological basis for employing this modern analogue, allowing the usage of a sedimentological analogue. The Naeles Delta, part of the Lake Eyre Basin (3.6), is an arid-terminal fan system with ephemeral fluvial, aeolian, and lacustrine influence, just as the depositional environment of the Slochteren Formation ([Felder, 2024, Felder, 2010, Lang et al., 2004]) (figure 6). This modern depositional system provides critical insights into sediment dispersal patterns, avulsion dynamics, and facies transitions, offering a comparative framework for interpreting ancient fluvial deposits in the study area.

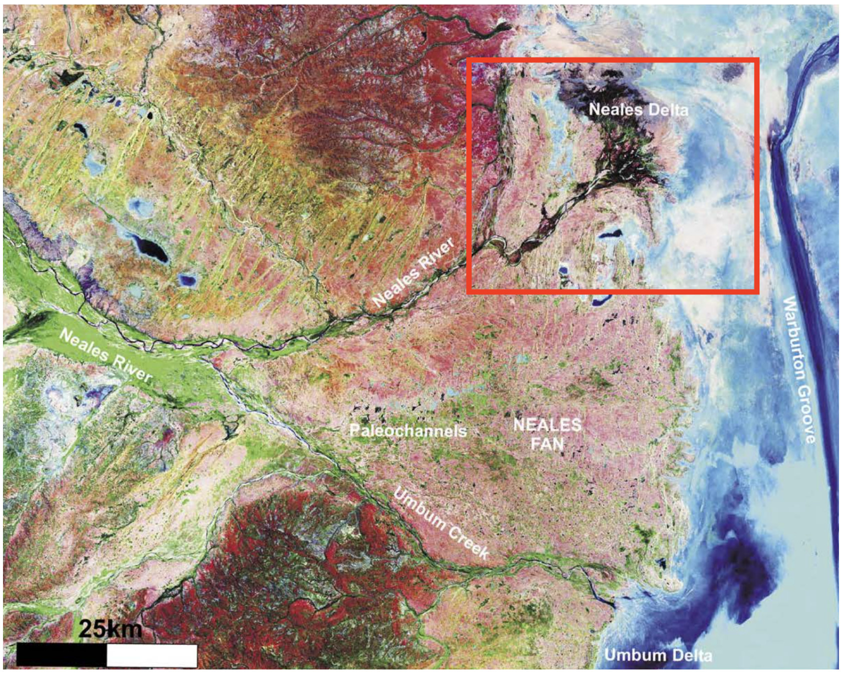

Figure 6: Satellite image (1990) of the Naeles Fan, part of the Lake Eyre Basin. Embarked in red is the Naeles Delta and is the analogue area of the Upper Slochteren Member. Modified from [Lang et al., 2004].

In the Lake Eyre Basin, the Neales Delta is the terminal fan that exhibits sedimentary characteristics analogous to the Upper Slochteren Member. In the proximal area of the terminal fan of the Neales delta, the channels exhibit high net-to-gross sand deposits, with larger, coarser-grained sediments forming thick amalgamated deposits, while the channel sand bodies in the distal area gradually transition into isolated, finer-grained splay and delta mouth bar deposits. The sediment grain size of the distal deposits decreases rapidly from medium-coarse sand to fine sand, silt, and eventually muds ([Lang et al., 2004]). Such spatial trends are expected to be present within the Upper Slochteren Member, where depositional cycles are characterized by systematic shifts in grain size, sediment sorting, and accommodation space creation. The proximal deposits tend to be more laterally extensive, forming large, interconnected sand sheets due to limited accommodation space. The distal deposits, however, exhibit increased heterogeneity due to the presence of interbedded fine-grained floodplain and playa sediments. This results in more pronounced reservoir compartmentalization, affecting connectivity and fluid flow behavior ([Lang et al., 2004]).

However, differences in sediment supply rates, subsidence patterns, and climatic conditions must be acknowledged when applying this analogue to the Slochteren system. While the Neales Delta is a suitable comparison, caution should be exercised in directly extrapolating its characteristics to the study area without considering potential depositional-scale variations.

3.2 Depositional Zones

The Slochteren formation, has been deposited in the range of a fluvial system but distal-proximal changes, induced by autogenic and allogenic processes, resulted in differences within the formation. The Upper Slochteren member has been target in this study and shows both lateral and vertical depositional differences. These differences are created by (slight) environmental differentiations. Therefore, within this member, different zones can be distinguished based on their environmental characteristics. The Upper Slochteren member consist of three zones: the A, B and C zone where the C zone consist of the C1, C2 and C3 zones (figure 7). In figure 7, a well log of the B well is illustrated, in which zone A is named as USL A, B as USL B, and C3 as USL C3. From now on when in a figure USL X is shown, where X is A, B, C1, C2 or C3, it represents the zone of X. The A, B, C1, C2 and C3 zones represent three different depositional cycles: The A zone, B and C1 zones and C2 and C3 zones, in which the sands of A, C1 and C3 occur at the top of each cycle. The three cycles, A, B to C1, and C2 to C3, correspond to three phases of S-N fan progradation. With each successive cycle, the study area's position within the fan system becomes progressively more distal ([Felder, 2024]). [Felder, 2024] also defined the system by a gradual rise in flooding or playa water levels.

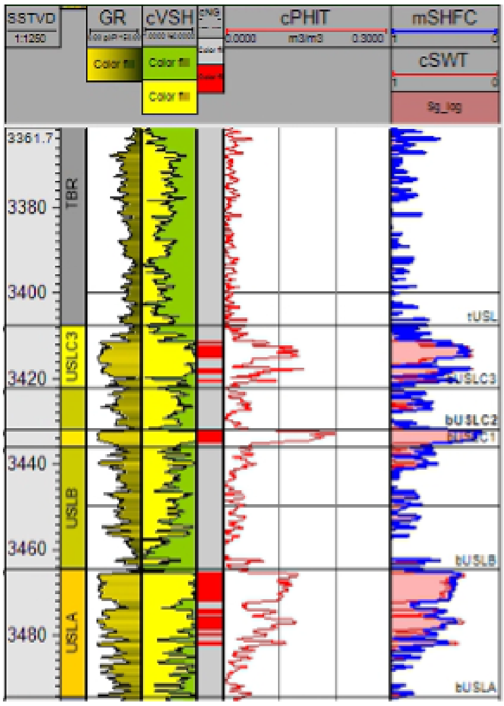

Figure 7: Well log of the B well. The Upper Slochteren Member can be seen from depth 3494 till 3408 SSTVD. The Slochteren Member starts its succession with the A zone (USL A), followed by the B Zone (USL B) and C zone (USL C3. The two layers between the B and C3 zones, are the C1 and C2 zone from bottom to top.

The B well is located in the area marked by the L11b-A10, L11b-A06, L11b-A08 and L11-14 wells, making its environment determination based on other wells their characteristics possible but difficult (8). Since the variability of deposits and their corresponding structures and elements is high in this area, some assumptions should be made during interpretation. For the well B there will be considered that architectural elements and sedimentary structures are similar to the elements and structures from corresponding depositional environments and from surrounding wells (e.g. (non) amalgamating channels, crevasses). A general overview with all assumptions will be given in chapter 4.3. With the help of the well log of the B well and references, the depositional environment will be determined based on its characteristics and surrounding known environments in chapter 5.1 .

3.2.1 A-zone

The A zone is the first cycle deposited in the area and forms the base of the Upper Slochteren member. [Felder, 2024] described the depositional environments of the A zone in the area and provided more detailed environmental interpretations for surrounding wells. The overall environment varies from fan to distal fan in the L11 block ([Felder, 2024]) (figure 8). In the entire L11 block, the base of the A zone was deposited during a fan front and mud flat environment and its depositions are characterized by isolated and thin unconfined sands ([Felder, 2024]). During the deposition of the center of the A zone, the environment slightly changed laterally resulting in different depositions in the North and South. The environment in the Southeast of the 11 blocks (L11-16) changed from fan front and mudflat to a distal fan overlain by fan environment while the environment in the North of the 11-block (L11bA06-L11bA08) changed to fan front and distal fan environments, overlain by mudflats ([Felder, 2024]). The most common architectural elements present in the Southeast distal fan environment were thin channels and abandoned channels, sometimes separated by thin clay layers ([Felder, 2024]). In the North, the distal fan consisted of channels, crevasses and abandoned channels and were overlain by mudflats. The environment of the top of the A zone changed in the North from distal fan to fan environment while in the Southeast a fan environment was present ([Felder, 2024]). The fan deposits in the North were less amalgamated and thinner channels with crevasses present, while in the Southeast the channels were thicker and more amalgamated ([Felder, 2024]). Variations in thicknesses and volume of architectural elements in the A zone are common in the area and an overview of the thicknesses and volumes of the architectural elements (channels, amalgamated channels, crevasses) for wells in the area are given in figures 11 to 14.

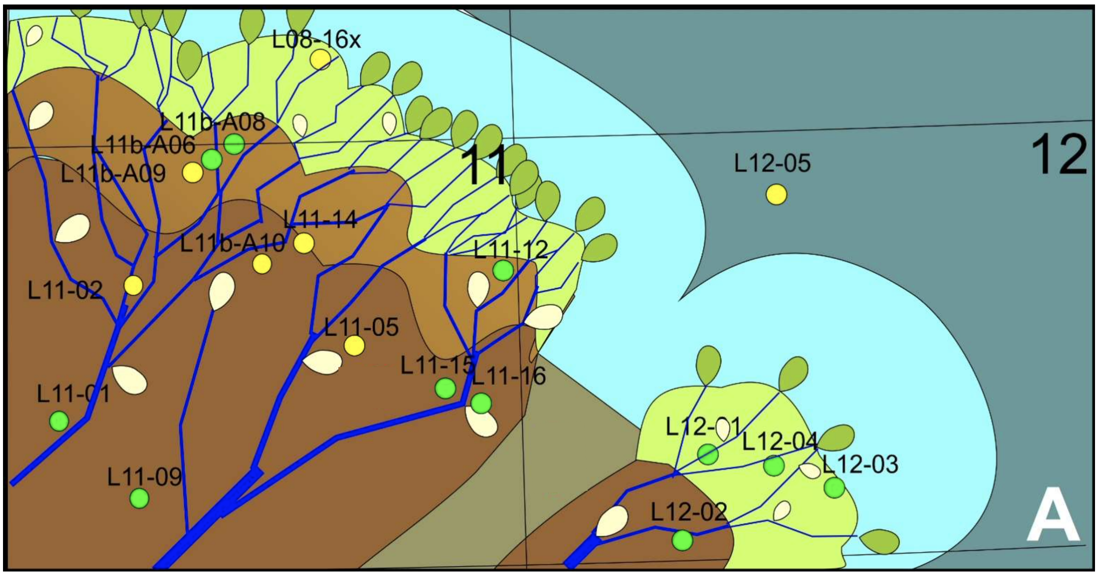

Figure 8: Overall overview of depositional environment of the Upper Slochteren A zone. The B well is located near the L11bA10 well. Dark Brown: Fan (high sediment load), Light brown: Fan (low sediment load, Light green: Distal Fan, Dark Green (Mouthbar element), light blue: Fan Front, dark blue: mudflat. From: [Felder, 2024]

3.2.2 B- and C1-zones

The B- and C1-zones together constitute the second depositional cycle of the Upper Slochteren Member within the L-block. The depositional environments present during the formation of both zones ranged from mudflat to fan settings ([Felder, 2024]). The B zone was primarily deposited in a mudflat environment in the northern region. However, moving southeastward, the upper layer of the B-zone became increasingly dominated by fan-front deposits, which overlie the mudflats ([Felder, 2024]). In the southeastern area, the overlying fan-front deposits are thicker than those associated with the mudflat environment. The architectural elements of the B zone fan-front deposits include isolated channels, terminal lobes and crevasses. The deposition of the C1-zone indicates a lateral shift in the depositional environment, transitioning from a mudflat in the north and a fan-front in the southeast to a distal fan in the north and a fan with a low sediment load in the southeast ([Felder, 2024]) (figure 9). Well log data from wells in the region reveal that the thickness of the C1 zone varies (figure 11). Deposits in the northern area exhibit heterogeneity, characterized by thin channels and crevasse-related elements. In contrast, the fan deposits in the southeast are dominated by thick, amalgamated channels and abandoned channels ([Felder, 2024]). Variations in thicknesses and volume of architectural elements in the C1-zone are common in the area and an overview of the thicknesses and volumes of the architectural elements (channels) for wells in the area are given in figures 11 to 14.

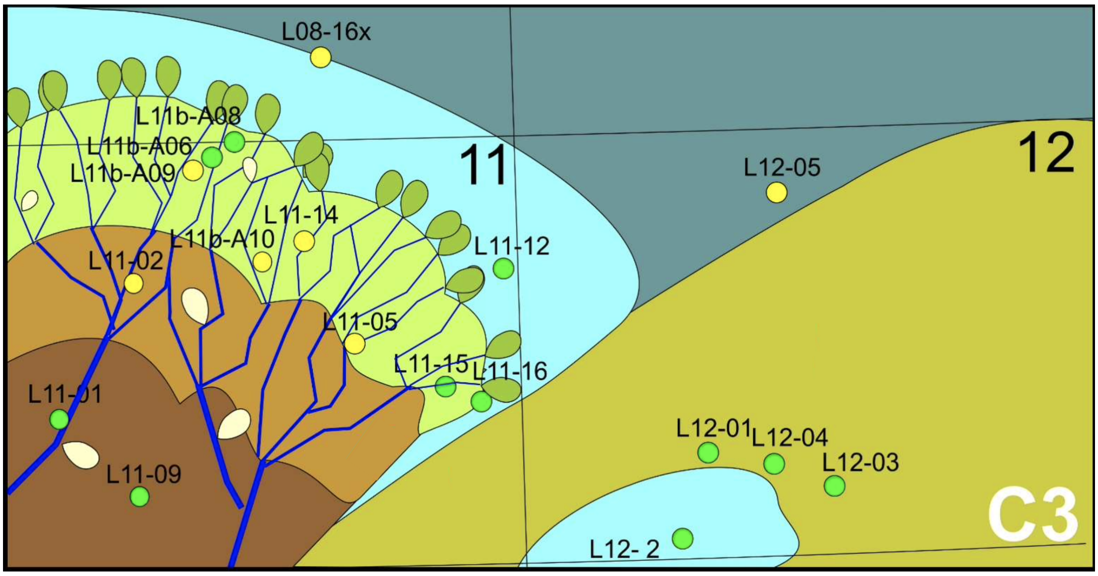

Figure 9: Overall overview of depositional environment of the Upper Slochteren C1 zone. The B well is located near the L11bA10 well. Dark Brown: Fan (high sediment load), Light brown: Fan (low sediment load, Light green: Distal Fan, Dark Green (Mouthbar element), light blue: Fan Front, dark blue: mudflat. From: [Felder, 2024]

3.2.3 C2- and C3-zones

The final depositional cycle of the three that comprise the Upper Slochteren Member in the L block consists of the C2- and C3-zones. The depositional environments during this cycle ranged from mudflat to fan-front and distal fan settings ([Felder, 2024]). The C2-zone was deposited in a mudflat environment at its base, transitioning to a fan-front environment at the top in the northern region. In contrast, in the southeastern area, a bigger part of the C2-zone was deposited under fan-front conditions ([Felder, 2024]). Well log data from the L-block, spanning from the north to the southeast, indicate thickness variations within the C2-zone. The fan-front deposits of the C2-zone contain isolated channel elements ([Felder, 2024]). The C3-zone predominantly represents distal fan deposition and overlies the C2-zone. In the southeastern area, the base and central portions of the C3-zone were deposited in a fan-front environment, with distal fan conditions only occurring at the top ([Felder, 2024]). The C3 zone exhibits significant heterogeneity, characterized by thin channels, crevasse deposits, and abandoned channels intercalated with clay drapes ([Felder, 2024])(Figure 10). Channels in the northern region of the study area are thinner than those in the southeast, where crevasse features appear more frequent. Well B is situated near the L11bA10 well, suggesting that its depositional environment may be characterized by either a distal fan or a fan (low sediment load). This environmental variation could imply the presence of amalgamated channels ([Felder, 2024, Lang et al., 2004]). Variations in thicknesses and volume of architectural elements in the C3 zone are common in the area and an overview of the thicknesses and volumes of the architectural elements (channels) for wells in the area are given in figures 11 to 14.

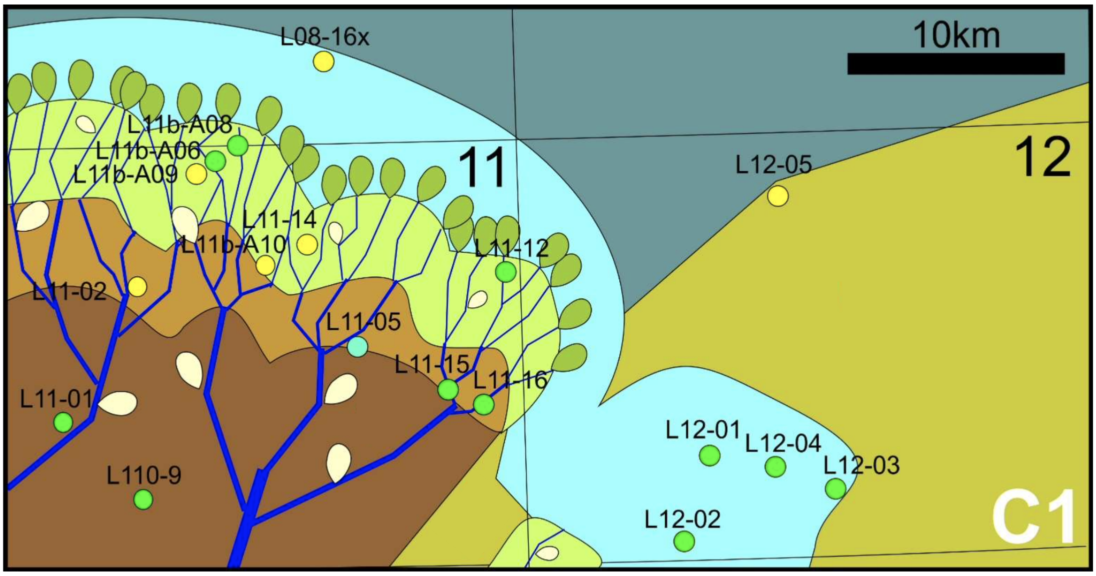

Figure 10: Overall overview of depositional environment of the Upper Slochteren C3 zone. The B well is located near the L11bA10 well. Dark Brown: Fan (high sediment load), Light brown: Fan (low sediment load, Light green: Distal Fan, Dark Green (Mouthbar element), light blue: Fan Front, dark blue: mudflat. From: [Felder, 2024]

3.3 Reservoir Connectivity and Recharge

Connectivity is an important characteristic of a reservoir that needs to be understood to improve gas (hydrogen, carbondioxide, methane) and fluid movements within a reservoir. Connectivity refers to the part of the reservoir that is connected to the well through direct contact or interconnected bodies; areas not connected to the well cannot be used effectively. With better analyzation of reservoir connectivity both the lateral continuity and geological basis of the reservoir can be determined to improve and enhance development strategies ([Xue et al., 2021, Larue and Hovadik, 2006, Hovadik and Larue, 2007]). An important note to take into account is that connectivity provides an indication of flow potential within a reservoir but does not prove flow potential ([Hovadik and Larue, 2007]). Reservoir connectivity is a complex function consisting of several variables classified into three stages ([Ainsworth, 2005]). The first stage is called depositional or static connectivity and is characterized by the net-to-gross ratio and the architectures defined by geobodies and sandstone bodies. The second stage is structural connectivity and is defined by structural parameters, such as faults and fault interconnections. And lastly, the third stage is dynamic connectivity characterized by permeability and porosity of the reservoir ([Ainsworth, 2003, Ainsworth, 2005, Ainsworth, 2006, Larue and Hovadik, 2006, Hovadik and Larue, 2007]).

The first stage, the depositional connectivity, is defined by several parameters such as sand/shale ratios, geobody geometries, geobody distributions and net-to-gross ratios ([Ainsworth, 2003, Ainsworth, 2005, Ainsworth, 2006, Larue and Hovadik, 2006, Hovadik and Larue, 2007, Xue et al., 2021]). The net-to-gross (N:G) value of a reservoir is determined by the proportion of reservoir-quality rock to total rock volume and provides insight in both the lateral as vertical connectivity of a reservoir. The N:G value helps to assess the sand-to-shale ratio and predict connectivity, porosity and permeability. [Larue and Hovadik, 2006] determined that reservoirs with N:G values of 0.3 or more have stratigraphical connectivity's usually greater then 0.9 and N:G values of 0.3 or less show little to no sign of connectivity (lower then 0.2). However, connectivity is not determined by N:G values only. Other factors influence the connectivity as well, such as the channel width to channel thickness ratios. Reservoirs with high width to thickness ratios still achieve high connectivity with low N:G ratio. On the contrary, reservoirs with parallel channel deposits, mudstone beds and/or compartmentalization with high N:G ratio could show low connectivity ratios ([Larue and Hovadik, 2006]). It is therefore crucial to understand depositional connectivity to comprehend reservoir behavior and to assess the likelihood of wells being connected and in communication with sandstone bodies directly or with interconnected sandbodies further away from the well ([King, 1990, Ainsworth, 2005, Xue et al., 2021]). The second stage, structural connectivity, is influenced by structural factors such as syn- and post-depositional faulting, fault geometry, and the transmissibility properties of faults ([Ainsworth, 2005, Ainsworth, 2006, Xue et al., 2021]).

On one hand, faults and folding can create structural barriers within the reservoir, reducing connectivity. On the other hand, faults and folding may enhance connectivity by linking compartmentalized reservoir sections ([Larue and Hovadik, 2006]). The third stage, dynamic connectivity, is completely shaped by permeabilities of the reservoir. Permeability can be related to porosity and both properties influence fluid-flow behavior of the reservoir ([Ainsworth, 2005, Xue et al., 2021]). The reservoir connectivity of the well B is mostly determined by the depositional connectivity and dynamic connectivity by [Felder, 2024] since the near well reservoir of the B well is not heavily influenced by faults. However, microstructures could enhance the connectivity within the reservoir.

There are two types of connectivity described by [Larue and Hovadik, 2006]: sandbody or geobody connectivity and reservoir connectivity. Sandbody connectivity corresponds to the fraction of the reservoir that is connected internally, while reservoir-to-well connectivity refers to the fraction of the reservoir that is directly linked to the wells ([Larue and Hovadik, 2006]). Both connectivity types are important to understand to explain the recharge behavior of the Upper Slochteren Zones in the B wellbore area. Since there is a fraction of the reservoir directly connected to the well, and the far field reservoir which is connected internally. In this study, the focus will be on the near well bore area. Reservoir connectivity plays a key role in determining and predicting recharge behavior in reservoirs. During extraction or injection of a fluid or gas, pressure differences are created in the subsurface. Injection and extraction processes must be conducted within a specific pressure range to maximize efficiency. If this range is exceeded, the process must be halted until the pressure returns to the operational range. In the case of pressure differences, fluids and gasses flow from high pressure zones to low pressure zones until the pressure is equalized throughout the reservoir. The flow of gas from high to low pressure zones (=recharge) is enhanced when sand bodies are (inter)connected with each other. The amount of time it takes for the pressure to be equalized throughout the reservoir depends on the rate the fluid or gas flows from the high-pressure zone to the lower pressure zone, also known as permeability of the connected sandstone bodies. The recharging behavior (quick or slow recharge) of a reservoir determines the rate that injection or extraction can take place. To effectively evaluate the potential of subsurface reservoirs for various applications and predict flow behavior within the reservoir, it is essential to map and define the connectivity of sandstone bodies and understand the architecture of these connected sandstones ([King, 1990, Larue and Hovadik, 2006]).

Based on the architectural elements described above, the reservoir zones can be interpreted in terms of their influence on the connectivity of the sandstone body and the 3D flow behavior. The degree of lateral and vertical connectivity varies across zones and is directly related to the presence, size, and arrangement of geobodies such as amalgamated channels, crevasses, and mudflats.

The top of the A-zone is one of the gas bearing layers within the Upper Slochteren and consist mainly of amalgamated channels which increase connectivity potential. This enhances both horizontal and vertical flow potential. The B-zone is dominated by mud deposits, which generally lower its flow potential and make it less heterogeneous. However, the presence of channels and crevasses can locally enhance connectivity and provide limited vertical pathways.The C1-zone, like the A-zone, contains amalgamated channels and displays significant heterogeneity in both porosity and permeability. Despite this variability, the sand deposits in this zone are laterally and vertically connected, allowing flow movement.The C2-zone comprises predominantly mudflat deposits interspersed with channel and crevasse elements. These elements increase internal connectivity, enhancing flow movement within the zone. The C3-zone begins with crevasse deposits at the base followed by a coarsening-upward sequence of channels. This stratigraphy supports vertical connection between sand bodies and imporves overall connectivity potential within the zone.

Understanding the scale and arrangement of these heterogeneities is critical for evaluating 3D connectivity and forms the basis for the architectural scenarios tested in this study.

3.4 Controls on Reservoir Quality

Reservoir quality is defined by its characteristics and flow pathways. Reservoir quality can be predicted on different scales. At the largest scale, the volume and type of deposit and connectivity are the main controlling factors ([Bell et al., 2018, Lan et al., 2016]). In the case of the B well, sandstone is the reservoir rock, and its reservoir quality is determined by porosity and permeability ([Porten et al., 2016, Bell et al., 2018]). The porosity of a reservoir concerns the volume of gas or fluid in place and permeability determines the rate at which the gas or fluid flows ([Gluyas and Swarbrick, 2021]). As described in the study of [Bell et al., 2018], porosity and permeability are both determined by primary sedimentological textures and mineralogy. Several studies have showed that architectural elements play a key role in controlling primary sedimentary structures influencing permeability, porosity, sandstone connectivity and flow pathways ([Liu et al., 2017, Bell et al., 2018, Porten et al., 2016, Hovadik and Larue, 2007, Xue et al., 2021]). The distribution, shape and volume of architectural elements can impact the lateral and vertical heterogeneity influencing the reservoir quality and flow migration. Besides the architectural elements, the presence of mud drapes or pore-filling clays impact the reservoir quality as well ([Bell et al., 2018]). Thicker sand channels are less compartmentalization and contain less barriers, resulting in overall better permeability with fewer heterogeneity, while thinner (more amalgamated) channels are more compartmentalized with internal barriers which negatively influence permeability and increases heterogeneity. The channel deposits of the B well mainly consist of sandstone layers separated by mud/clay drapes, which are called baffles. The study area consists of four main architectural elements containing thick and thin channels, amalgamated channels, crevasses and abandoned channels. The clay content in the reservoir zones, determine for a large part whether a zone has a high reservoir quality. Facies with high pore-filling clay content have lower reservoir quality, while facies with low pore-filling clay have better reservoir quality ([Bello et al., 2021]). High clay content is often observed with fine grain sizes and low clay content with coarser grain sizes ([Bello et al., 2021]).

3.5 Trends in Area

To ensure the development of realistic models, depths, dip and thickness trends must be considered and incorporated during the modeling of the B well. The depth trends of the A, B, and C zones of the Upper Slochteren Member are determined using existing well log data from surrounding wells within the L-block. Observations in the L-block reveal depth trends along the West-East (W-E), North-South (N-S), Southwest-Northeast (SW-NE), and Northwest-Southeast (NW-SE) orientations. The W-E, N-S, and NW-SE trends indicate progressively shallower depths where the A, B, and C zones are located. Among these, the NW-SE trend exhibits a slightly steeper dip compared to the N-S trend, with the W-E trend having the lowest dip magnitude. The overall trend suggests that depth decreases more sharply when moving southward than when moving eastward. Conversely, the SW-NE trend displays the opposite pattern, where the zones are found at slightly greater depths. These trends reflect a tilted and gently warped 3D surface, with the shallowest depths of the Upper Slochteren Member's A, B, and C zones occurring in the southeast of the study area.

The thicknesses of the Upper Slochteren zones vary within the L-block. However, no trend for thickness variations is observed. The thickness differences could be explained by (local) differences in geological environments, accumulation space, compression differences, faults or other (location specific) geological phenomenon.

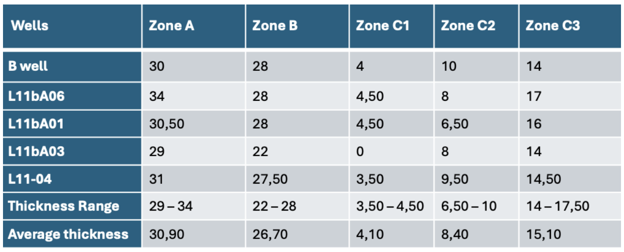

Wells	Zone A	Zone B	Zone C1	Zone C2	Zone C3
B well	30	28	4	10	14
L11bA06	34	28	4,50	8	17
L11bA01	30,50	28	4,50	6,50	16
L11bA03	29	22	0	8	14
L11-04	31	27,50	3,50	9,50	14,50
Thickness Range	29 – 34	22 – 28	3,50 – 4,50	6,50 – 10	14 – 17,50
Average thickness	30,90	26,70	4,10	8,40	15,10

Figure 11: Table showing the thicknesses, thickness range and average (in SSTVD) of the Upper Slochteren zones for wells in the L-field.

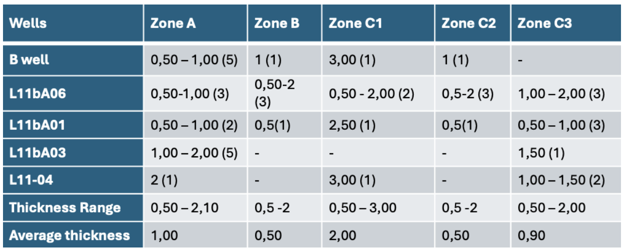

Wells	Zone A	Zone B	Zone C1	Zone C2	Zone C3
B well	0,50 – 1,00 (5)	1 (1)	3,00 (1)	1 (1)	-
L11bA06	0,50-1,00 (3)	0,50-2 (3)	0,50 - 2,00 (2)	0,5-2 (3)	1,00 – 2,00 (3)
L11bA01	0,50 – 1,00 (2)	0,5(1)	2,50 (1)	0,5(1)	0,50 – 1,00 (3)
L11bA03	1,00 – 2,00 (5)	-	-	-	1,50 (1)
L11-04	2 (1)	-	3,00 (1)	-	1,00 – 1,50 (2)
Thickness Range	0,50 – 2,10	0,5 -2	0,50 – 3,00	0,5 -2	0,50 – 2,00
Average thickness	1,00	0,50	2,00	0,50	0,90

Figure 12: Table showing the thickness (number of channels) and thickness range and average of channels (in SSTVD) in the Upper Slochteren zones for wells in the L-field

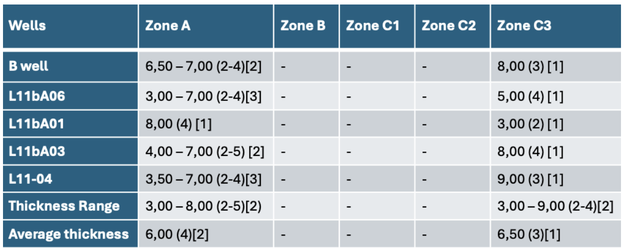

Wells	Zone A	Zone B	Zone C1	Zone C2	Zone C3
B well	6,50 – 7,00 (2-4)[2]	-	-	-	8,00 (3) [1]
L11bA06	3,00 – 7,00 (2-4)[3]	-	-	-	5,00 (4) [1]
L11bA01	8,00 (4) [1]	-	-	-	3,00 (2) [1]
L11bA03	4,00 – 7,00 (2-5) [2]	-	-	-	8,00 (4) [1]
L11-04	3,50 – 7,00 (2-4)[3]	-	-	-	9,00 (3) [1]
Thickness Range	3,00 – 8,00 (2-5)[2)	-	-	-	3,00 – 9,00 (2-4)[2]
Average thickness	6,00 (4)[2]	-	-	-	6,50 (3)[1]

Figure 13: Table showing the thickness of amalgamated channels (number of channels within amalgamation) [number of amalgamated channels) and thickness range and average in the Upper Slochteren zones for wells in the L-field

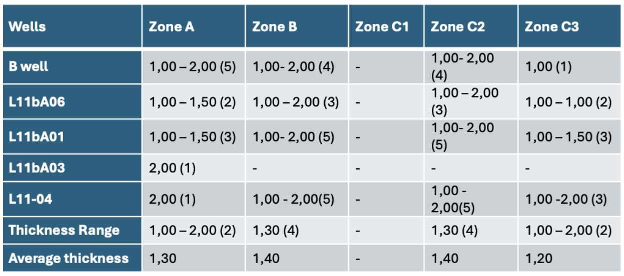

Wells	Zone A	Zone B	Zone C1	Zone C2	Zone C3
B well	1,00 – 2,00 (5)	1,00- 2,00 (4)	-	1,00- 2,00 (4)	1,00 (1)
L11bA06	1,00 – 1,50 (2)	1,00 – 2,00 (3)	-	1,00 – 2,00 (3)	1,00 – 1,00 (2)
L11bA01	1,00 – 1,50 (3)	1,00- 2,00 (5)	-	1,00- 2,00 (5)	1,00 – 1,50 (3)
L11bA03	2,00 (1)	-	-	-	-
L11-04	2,00 (1)	1,00 - 2,00(5)	-	1,00 - 2,00(5)	1,00 -2,00 (3)
Thickness Range	1,00 – 2,00 (2)	1,30 (4)	-	1,30 (4)	1,00 – 2,00 (2)
Average thickness	1,30	1,40	-	1,40	1,20

Figure 14: Table showing the thicknesses and thickness range and average of crevasses (in SSTVD) in the Upper Slochteren zones for wells in the L-field

3.6 Lake Eyre Analogue

As before mentioned serves the Lake Eyre Basin as a good analogue of the depositional environments of the Upper Slochteren member zones. With the help of the Lake Eyre analogue, a rough estimation can be made of the architectural element's length of the Upper Slochteren member. The length and width derived from the analogue together with the determined thicknesses and volumes from the well logs (figures 11 to 14), provide a good and realistic basis for the creation of various architectural scenarios for the Upper Slochteren zones. The channels within the main channel complex of the Neales Delta/Terminal Splay ranges in width between 50 and 150 meters and present crevasses in the Neales Delta area have lengths ranging from 10 to a maximum of 4000 meter and widths ranging 10 to a maximum of 250 meter ([Lang et al., 2004]).

3.7 Vertical and Horizontal Permeability

The vertical permeability and porosity values of the B well have been determined by ONE-Dyas and are provided in an Excel sheet. In this excel sheet, the porosity and permeability values are determined at 0,152m intervals. The porosity and permeability of the several layers are appointed based on the average values that were given in the excel sheet. The properties of the elements of the B and C2 zones are determined based on well log interpretation and the porosity and permeability values found on corresponding depths. The properties of elements of the A, C1 and C3 zones are determined based on average values (figure 15).
However, there are no horizontal permeability data available for the Upper Slochteren zones from ONE-Dyas. Horizontal permeability is a key parameter for characterizing reservoir behavior, particularly in understanding lateral fluid flow, which also influences vertical flow behavior. The Upper Slochteren Member is known for its high degree of heterogeneity, largely caused by the presence of numerous baffles interbedded with channel sandstones. This configuration suggests that horizontal permeability is generally higher than vertical permeability, as supported by previous studies ([Philip et al., 2012, Goupil et al., 2022]). Vertical permeability is more strongly affected by these internal baffles, while horizontal flow pathways remain relatively less obstructed. As a result, it is reasonable to assume an anisotropy ratio (Kv/Kh) of much less than 1.0 for these zones. [Philip et al., 2012] investigated anisotropy factors in sandstones of the Niger Delta and reported values ranging between 0.5 and 0.9. For Rotliegend sandstones (Groningen gas field), other studies have adopted even lower ratios, with [van Oeveren et al., 2017] using a value of 0.25. In industry practice, it is often assumed that the vertical permeability is approximately 0.1 of the horizontal permeability ([Monsees, 2021, Cannon, 2024, Gibbons et al., 1993]). Moreover, some studies indicate that sandstones with higher horizontal permeability values (typically above 100 mD) tend to retain relatively high vertical permeability as well ([Monsees, 2021, Philip et al., 2012]).

Given the broad range of anisotropy values reported in both academic and industry sources, it is not feasible to assign a single definitive anisotropy factor without introducing a degree of uncertainty. Therefore, in this study, average values of known anisotropy factors are used to estimate horizontal permeability from the known vertical permeability: a ratio of $Kv/Kh = 0.5$ is applied to deposits with $100mD > Kv > 10mD$ and a ratio of $Kv/Kh = 0.4$ is assigned when $Kv < 10mD$. By selecting these values, this study aligns with findings reported in both academic literature and industry practice.
The vertical and horizontal permeabilities and porosity of the elements and layers are given in figure 15. For an overview of the detailed input of the permeability and porosity values, see 10.

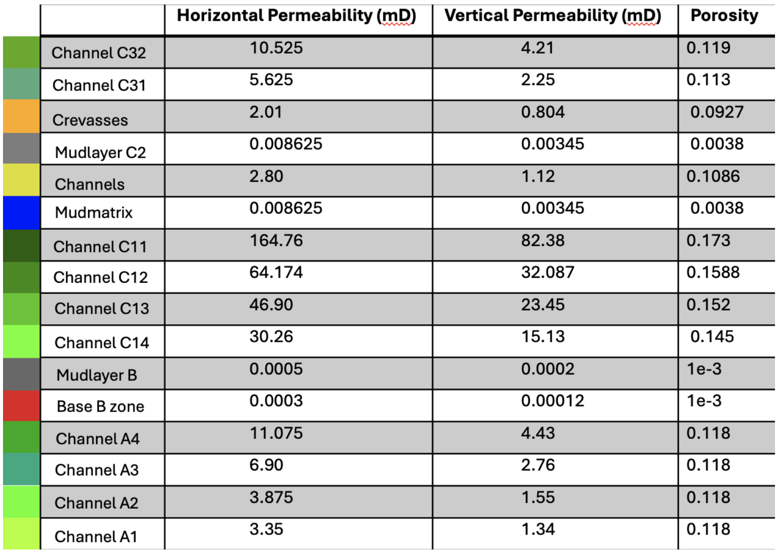

		Horizontal Permeability (mD)	Vertical Permeability (mD)	Porosity
🟩	Channel C32	10.525	4.21	0.119
🟩	Channel C31	5.625	2.25	0.113
🟧	Crevasses	2.01	0.804	0.0927
⬛	Mudlayer C2	0.008625	0.00345	0.0038
🟨	Channels	2.80	1.12	0.1086
🟦	Mudmatrix	0.008625	0.00345	0.0038
🟩	Channel C11	164.76	82.38	0.173
🟩	Channel C12	64.174	32.087	0.1588
🟩	Channel C13	46.90	23.45	0.152
🟩	Channel C14	30.26	15.13	0.145
⬛	Mudlayer B	0.0005	0.0002	1e-3
🟥	Base B zone	0.0003	0.00012	1e-3
🟩	Channel A4	11.075	4.43	0.118
🟩	Channel A3	6.90	2.76	0.118
🟩	Channel A2	3.875	1.55	0.118
🟩	Channel A1	3.35	1.34	0.118

Figure 15: Table showing the horizontal and vertical permeability and the porosity of the layers and elements in the RRM and CMG models.

3.8 Capillary Pressure

The reservoir of the B well contains two immiscible fluid phases: gas and water. Flow behavior within this two-phase system is strongly influenced by the saturation levels of each phase and their interactions [Pereira, 2019]). Saturation values determine the total amount of gas and water within the pore space ([McPhee et al., 2015]). In addition to the absolute permeability of the rock, relative permeability influences the ability of gas to flow within the reservoir as well. Relative permeability is dependent on water saturation and absolute permeability and varies per rock type ([Honarpour and Mahmood, 1988]. In this study, relative permeability curves were derived from measured core data provided by ONE-Dyas. This data consisted of plots of the the water saturation versus the relative permeability.

Beyond effective and relative permeability, capillary pressure is another critical factor governing flow dynamics in gas-water reservoirs. Capillary pressure between water and gas defines the pressure threshold that must be exceeded for gas to displace water from the pore and flow through the pore space; this arises because interfacial tension prevents gas from invading small, water-filled pores unless sufficient pressure is applied ([Ren et al., 2022]). This threshold is represented by the drainage capillary pressure curve. In contrast, the imbibition capillary pressure curve describes the pressure difference required for water to displace gas from the pore space. Capillary pressure has a pronounced impact on the phase distribution of fluid mixtures and governs key aspects of fluid flow within porous media ([Zhang et al., 2017]). Therefore, it is necessary to determine capillary pressure values across different geological units and saturation conditions. Capillary pressure is typically calculated using the Leverett J-function, which expresses its dependence on permeability, porosity, interfacial tension, contact angle, and the dimensionless J-function. Base case capillary curves of comparable geological units (eg sand- and shales/mud-rich units) from the literature were used to determine the J-function value that was used to calculate the capillary pressure ([Abdoulghafour et al., 2020, Alipour K et al., 2022]) (figures 16 and 17). These J-function values were then applied to compute capillary pressure curves tailored to each rock type. The properties together with the formulas that were used to calculate the capillary pressures are given in figure 16. For the permeability and porosity values used in these calculations, average values from each RPT (rock property table in figure 16) were applied.

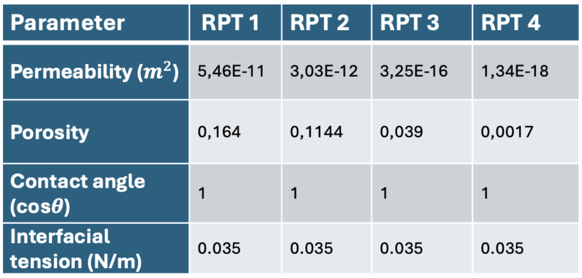

Parameter	RPT 1	RPT 2	RPT 3	RPT 4
Permeability (m^2)	5,46E-11	3,03E-12	3,25E-16	1,34E-18
Porosity	0,164	0,1144	0,039	0,0017
Contact angle (cosθ)	1	1	1	1
Interfacial tension (N/m)	0.035	0.035	0.035	0.035

$$P_c = \frac{\sigma \cdot \cos\theta}{\sqrt{k/\phi}} \cdot J(S_{we})$$

Figure 16: Table showing the input which was used to calculate the capillary pressures

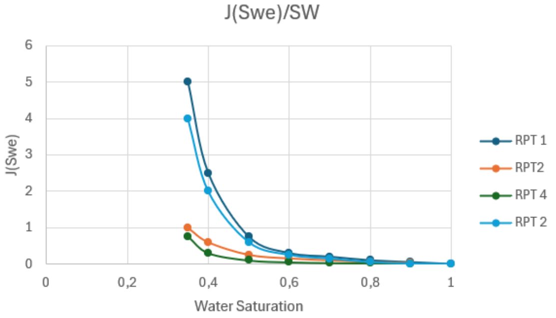

Figure 17: Graphs showing the J-Function (J(Swe)) value at different water saturations for all rocktypes

4 Methodology

Most of the created numerical models of the Earth's subsurface contain many uncertainties, due to geological heterogeneity distribution ([Jacquemyn et al., 2021]).Accurately representing geological heterogeneity is essential for a wide range of subsurface applications, including the assessment of resource distribution, the development of geothermal and hydrocarbon reservoirs, and evaluating the suitability of formations for CO_2 storage ([Geiger et al., 2009, Sun et al., 2008, Graham et al., 2018, Jacquemyn et al., 2021]). Additionally, the stratigraphic architecture determines whether the connectivity of a reservoir is sufficient and how flow migrates within the reservoir. Before flow simulations can be made, depositional models should be created. To quickly create these various models, Rapid Reservoir Modelling (RRM) will be used since it can create depositional models relatively quickly. An example of its interface is shown in figure 18. For a detailled step-by-step overview of the activities, see appendix 10.3.

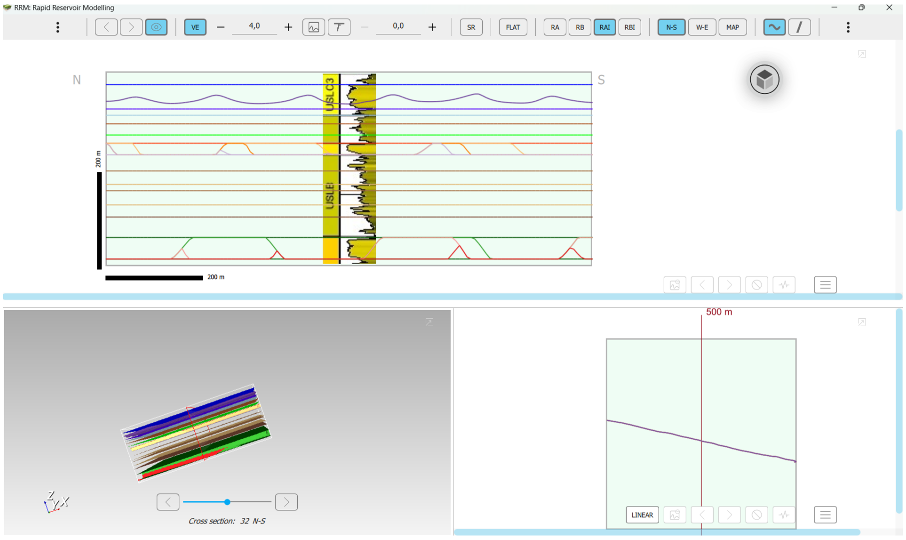

Figure 18: Screenshot of the interface of RRM. The top center window is the window in which the horizons can be sketched in either NS and WE direction, the left bottom window shows the model in 3D and in the right bottom window the trajectories of the horizons can be sketched. Above the windows, the tools are located. From left to right: undo, redo, VE (Vertical Exaggeration), Apply VE to image, Dip Angle Guide, SR (Sketch Region), FLAT (Flattening of horizon), RA (Remove Above), RB (Remove Below), RAI (Remove Above Intersected), RBI (Remove Below Intersected), N-S (North-South), W-E (West-East), MAP (Map View), Sketch Stratigraphy and Sketch Structure.

RRM is a Sketch-Based Interface Modelling (SBIM) approach for intuitively creating geological models in 3D, enabling the quick visualization and representation of geological concepts and ideas in three-dimensional models ([Jacquemyn et al., 2021]). SBIM enables the efficient sketching of geological concepts by using surfaces, such as faults, fractures, stratigraphic features, facies and lithological boundaries, to represent geological architecture and heterogeneity ([Huysmans and Dassargues, 2011, Jacquemyn et al., 2021]). After the depositional models of the reservoir are created in RRM, the models will be transferred to CMG to run flow simulations and to test whether (vertical) cross flow near the B wellbore area is possible. An example of the interface of CMG Results is shown in figure 24.

The data used in this thesis, is provided by ONE-Dyas and is collected by tests, drillings, studies from consultants and analyzing boreholes. These activities provided interpretations of depositional environments, well logs, stratigraphical records, permeability and porosity values, seismic images, net/gross and sand/shale ratios and core characteristics. The grid and its corresponding properties of the created RRM models can be saved as .grdecl file. These .grdecl files can be opened in Petrel and transferred to RESCUE files. These RESCUE files can be loaded into the Builder application of Computer Modeling Group (CMG).

4.1 Rapid Reservoir Modeling

Before constructing the base case model, the model dimensions—specifically its length and height—were defined. The spatial scale of the model must align with the objective of this study: to assess the potential for vertical cross-flow in the near-wellbore area. Based on this objective, the models domain was set to 1 km × 1 km horizontally and 100 m vertically. Since the Upper Slochteren member is highly heterogeneous, a grid size of 200x200x100 has been chosen to capture this heterogeneity. Following the model's cale determination, a static basecase model will be created in RRM containing horizons, dividing the zones and defining the zone's thicknesses. Additionally, the zones will be divided into subzones, indicting intern zonal differences in environment and/or characteristics. From thereon with the basecase model as starting point, several models will be created based on architectural element variations, which occur as described in Chapter Conceptual model.

To define a realistic basecase model, data of the B well is used. In order to load data into RRM, a well log file from the B well is processed into a JPG file. The loaded well log file in RRM acts as a realistic guidance to determine the thickness of the zones across the model and is located in the center of the model (figure 19). The thickness of the zones is assumed to be even across the model, thus the boundaries between the zones are straight lines (Assumption 2). Besides the zone's thicknesses, the well log of the B well provides information about the present elements and acts as a guidance for sketching the elements with their corresponding thicknesses. The width of the architectural elements is determined from analogues, as described in the chapter 3.6 and these values will be used to determine the 3D form of the elements.

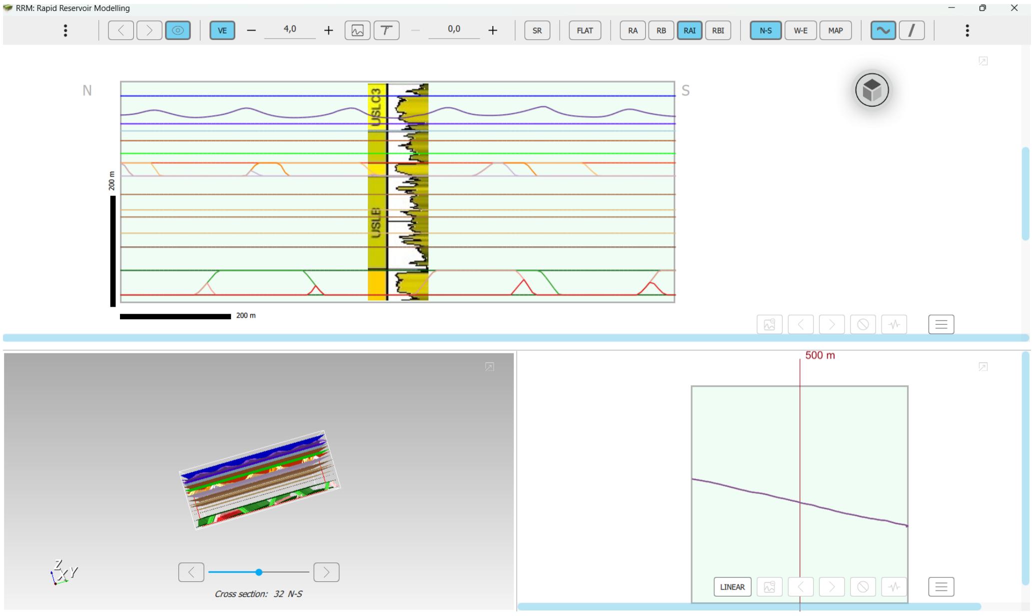

Figure 19: Illustration of the central placement of the B well in the model.

Starting from the base case, the A, C1, C3, and parts of the B and C2 zones are sketched, as these zones remain continuous across all scenarios (based on Assumptions 14 and 15). This forms a revised 'base case' scenario. The A zone is entirely composed of channel sands, represented by four different channel types that vary in properties (permeability and porosity) (Assumptions 3 and 5). The B zone begins with a basal mud layer, followed by three layers containing varying architectural elements, separated by two intervening mud layers. The C1 zone consists entirely of channel sands, also characterized by four distinct channel types based on property variations (permeability and porosity) (Assumption 3 and 5). The C2 zone begins with a mud layer, transitions into a layer with architectural elements, and ends with another muddy layer. Finally, the C3 zone starts with a crevasse deposit at the base, followed by two channel sand layers showing a coarsening-upward trend. The entire A, C1, C3-zones consist of continuous layers (green in figure 20), which means that in each scenario they are equal. The B- and C2-zones, consist of both continuous and non-continuous layers (green and blue respectively in figure 20). The variations in architectural elements are sketched within the non-continuous layers to test the effect of vertical connectivity on flow behaviour.

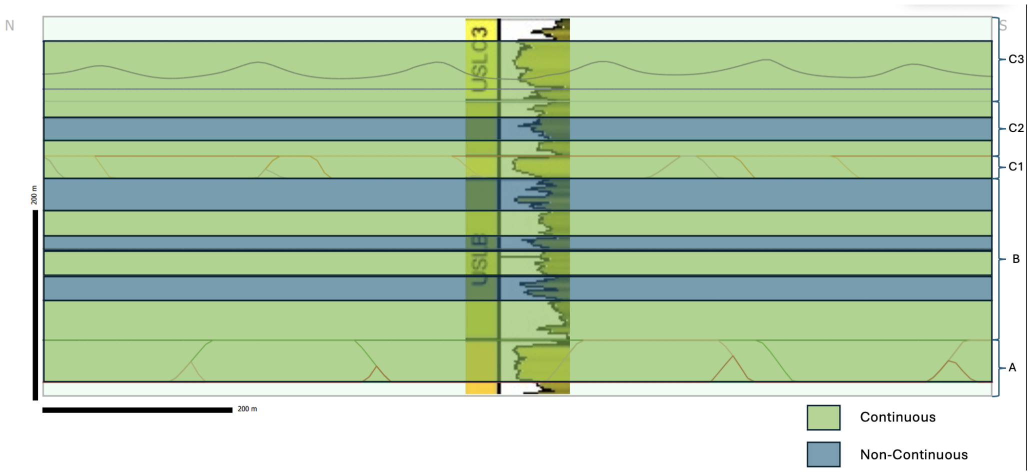

Figure 20: An illustration of the basecase model in which the continuous and non-continuous layers are being highlighted. The continuous layers are displayed in green, which means that those layers aren't varying in the different scenarios. The non-continuous layers (parts of the B and C2 zones) are displayed in blue, which means that those layers are varying in the different scenarios.

From this revised basecase on, the different scenarios are constructed based on varieties in the layers of the B and C2 zones with architectural elements present. The B zone has three layers in which these varieties occur, and the C2 zone has one layer. Four scenarios of the B and C2 zones are made based on the varieties in the amount of vertical connectivity zones between elements (channels and/or crevasses with each other):

- Scenario 1: In the first scenario, the architectural elements are vertical connected in three locations within each of the three B-zone layers and the C2 layer.

- Scenario 2: In the second scenario, the architectural elements are vertical connected in two locations within each of the three B-zone layers and the C2 layer

- Scenario 3: In the third scenario, the architectural elements are vertical connected in one location within each of the three B-zone layers and the C2 layer.

- Scenario 4: In the fourth scenario, the architectural elements are not vertical connected in each of the three B-zone layers and the C2 layer.

These four scenarios represent a family of models designed to test how variations in stratigraphical architecture influence recharge behavior in the near-wellbore area. Each scenario reflects a different configuration of vertical connectivity between sandstone bodies (e.g., channels and crevasses) in the B and C2 zones, thereby capturing a range of plausible geological uncertainties.

The scenarios range from three connectivity locations (scenario 1) to a completely disconnected case (scenario 4), with two and one connectivity location(s) points for scenarios 2 and 3, respectively (figure 21). These variations can be interpreted as the best- and worst-case scenarios for vertical stratigraphical crossflow since higher connectivity locations within a layer increase the likelihood of pressure communication and fluid movement between stratigraphical zones.

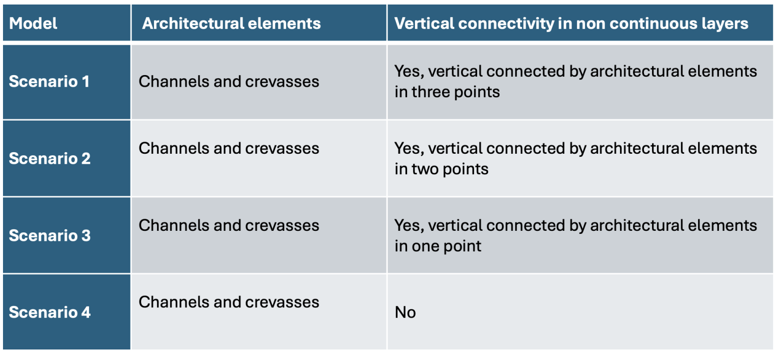

Model	Architectural elements	Vertical connectivity in non continuous layers
Scenario 1	Channels and crevasses	Yes, vertical connected by architectural elements in three points
Scenario 2	Channels and crevasses	Yes, vertical connected by architectural elements in two points
Scenario 3	Channels and crevasses	Yes, vertical connected by architectural elements in one point
Scenario 4	Channels and crevasses	No

Figure 21: Table representing an overview of which architectural elements are present in each scenarios and whether these architectural elements are vertically connected

By analyzing flow behavior across this range of scenarios, the study aims to evaluate whether vertical recharge from the A to the C1 zone is feasible under different assumptions of the connectivity of the sandstone body. This approach enables a qualitative understanding of how uncertainty in stratigraphical architecture, the four scenarios, may affect reservoir communication and recharge behavior in the near well-bore area.

4.2 Computer Modeling Group - IMEX

To test the effect of the different scenarios created in RRM on flow behavior in the Upper Slochteren Member, flow simulations were run in CMG. The RRM models were exported as .grdecl files and converted to RESCUE files using Petrel. These RESCUE files contain the grid dimensions and corresponding properties such as porosity and permeability. The exported grid size is 200 × 200 × 100 (x, y, z).

CMG is widely used in both industry and research to simulate flow behavior in geological models. Several applications within CMG were used in this thesis: Builder, cEDIT, IMEX, and Results. Builder was used to load the RRM models in RESCUE format, creating the simulation grid and assigning petrophysical properties such as porosity and permeability. The interface of Builder and its key windows are shown in figure 22.

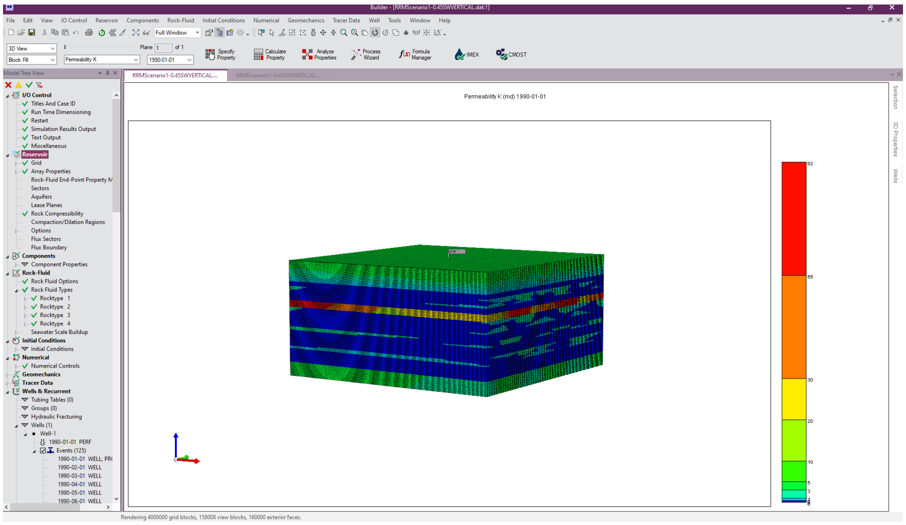

Builder - [RRMScenario1-0.45SWVERTICAL.dat:1]

3D View

Block Fill

Plane 1 of 1

Permeability K

1990-01-01

Full Window

Permeability K (md) 1990-01-01

Rendering 4000000 grid blocks, 158008 view blocks, 160000 exterior faces.

Figure 22: An illustration of the Builder interface. In the large window in the center, the 3D model is shown. At the left, the tree panel with its different input options is shown.

The simulation-ready input decks were then saved as .dat files and opened in cEDIT, where all inputs from

Builder are accessible as editable code. The interface of the cEDIT application is shown in figure 23. cEDIT was used to make manual adjustments to parameters. IMEX was used to perform the actual flow simulations using a gas-water formulation. IMEX is the blackoil simulator, which was used to simulate the models.

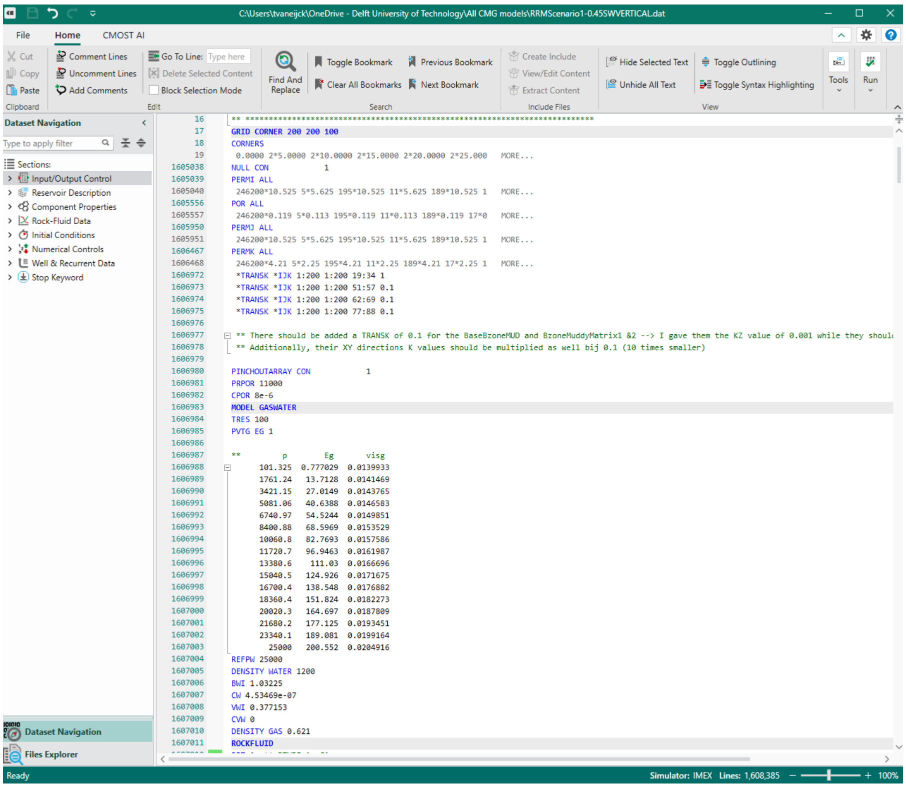

```
** ************************************************************************
GRID CORNER 200 200 100
CORNERS
 0.0000 2*5.0000 2*10.0000 2*15.0000 2*20.0000 2*25.000   MORE...
NULL CON            1
PERMI ALL
 246200*10.525 5*5.625 195*10.525 11*5.625 189*10.525 1   MORE...
POR ALL
 246200*0.119 5*0.113 195*0.119 11*0.113 189*0.119 17*0   MORE...
PERMJ ALL
 246200*10.525 5*5.625 195*10.525 11*5.625 189*10.525 1   MORE...
PERMK ALL
 246200*4.21 5*2.25 195*4.21 11*2.25 189*4.21 17*2.25 1   MORE...
 *TRANSK *IJK 1:200 1:200 19:34 1
 *TRANSK *IJK 1:200 1:200 51:57 0.1
 *TRANSK *IJK 1:200 1:200 62:69 0.1
 *TRANSK *IJK 1:200 1:200 77:88 0.1

 ** There should be added a TRANSK of 0.1 for the BaseBzoneMUD and BzoneMuddyMatrix1 &2 --> I gave them the KZ value of 0.001 while they shoul
 ** Additionally, their XY directions K values should be multiplied as well bij 0.1 (10 times smaller)

PINCHOUTARRAY CON           1
PRPOR 11000
CPOR 8e-6
MODEL GASWATER
TRES 100
PVTG EG 1

**          p        Eg       visg
      101.325  0.777029  0.0139933
      1761.24   13.7128  0.0141469
      3421.15   27.0149  0.0143765
      5081.06   40.6388  0.0146583
      6740.97   54.5244  0.0149851
      8400.88   68.5969  0.0153529
      10060.8   82.7693  0.0157586
      11720.7   96.9463  0.0161987
      13380.6    111.03  0.0166696
      15040.5   124.926  0.0171675
      16700.4   138.548  0.0176882
      18360.4   151.824  0.0182273
      20020.3   164.697  0.0187809
      21680.2   177.125  0.0193451
      23340.1   189.081  0.0199164
        25000   200.552  0.0204916
REFPW 25000
DENSITY WATER 1200
BWI 1.03225
CW 4.53469e-07
VWI 0.377153
CVW 0
DENSITY GAS 0.621
ROCKFLUID
```

Figure 23: An illustration of part of the cEDIT interface. The code of the input decks of Builder can be shown here and be adjusted. Additionally, new input decks can be added wirth code, increasing modeling speed.

Results was used to visualize simulation output, such as pressure and saturation values, and to extract time series such as gas/water production, gas/water volume and cumulative tracer. The interface of the Results application is shown in figure 24.

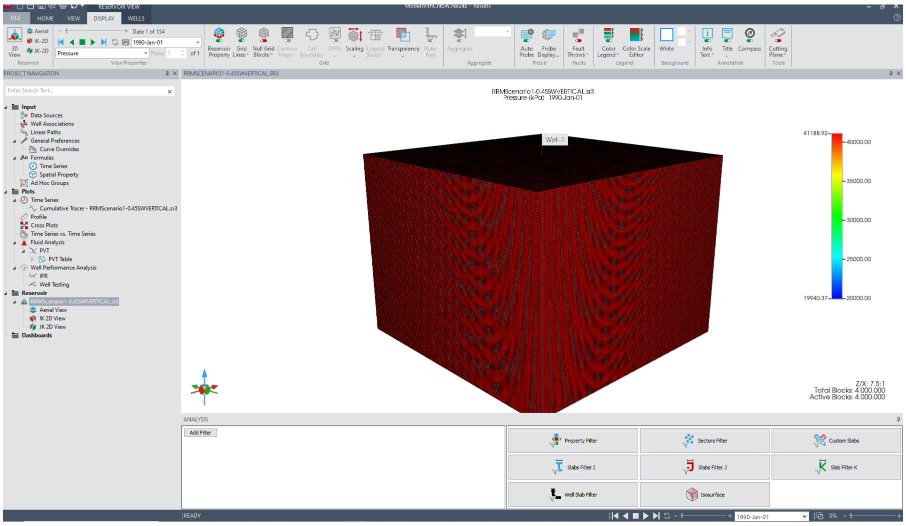

Figure 24: An illustration of part of the Results interface. The 3D view of the simulated model is now opened in which the pressure changes over time can be visually observed by changing the timeline at the top left. In the left window, plots can be made under Plots-Time Series/Profile.

Finally, cEDIT and IMEX were used to perform manual sensitivity analysises in order to test the influence of specific parameters on flow behaviour.

In Builder, the simulator was set to IMEX and the RESCUE file was then imported, after which the depth of the first layer (4750 m), the thickness of each layer (1 m), rock compressibility values, PVT diagrams, and SWGT tables were entered manually in the “Array Properties”, "Rock Compressibility", “Components” and “Rock-Fluid” windows respectively. Well placement, perforation depths, and the production scheme were added in the “Well and Recurrent” window. A homogeneous water saturation was applied across the entire model due to the absence of reliable water saturation data at the start of production. Production follows the historical field schedule, which began in 1990 and continued until 2009. After this period, the well was shut in for ten years to simulate a recharge phase, after which production was resumed in 2019. Once the input deck was complete, the model was saved as a .dat file and opened in cEDIT for further modifications. The layer structure of the model matches that of the models built in RRM. The stratigraphic zones included are, from top to bottom: C3, C2, C1, B, and A. The total modeled thickness of the Upper Slochteren Member is 100 meters, corresponding to 100 vertical grid cells, each 1 meter thick. The C3 zone is 19 meters thick and corresponds to grid cells 1 to 18. The C2 zone is 15 meters thick (grid cells 19 to 34), the C1 zone is 6 meters thick (grid cells 35 to 40), the B zone is 39 meters thick (grid cells 41 to 88), and the A zone is 12 meters thick (grid cells 89 to 100).

In Builder and cEDIT, four different rock types were defined and assigned to the model using the Rock-Fluid window. These rock types correspond to different SWGT tables that define the relative permeability to gas and water (krg and krw) at different water saturations. The SWGT tables are based on porosity-dependent data provided by ONE-Dyas. Rock type 1 was assigned to the C1 zone, while rock type 2 was used for both the A and C3 zones. The C2 and B zones were subdivided based on geological interpretation into continuous and discontinuous units (figure 20. The discontinuous layers were assigned to rock type 3 and the continuous layers to rock type 4 (figures 20 and 26). The capillary pressures at certain water saturations were calculated with the Leverette J-Function (figures 16, 17 and 25).

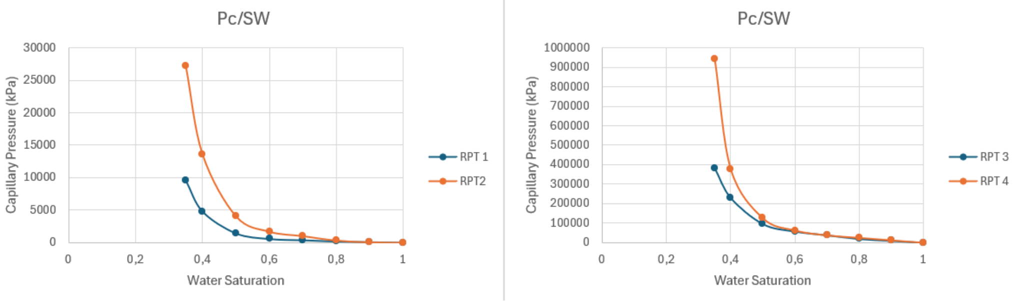

Figure 25: Graphs illustrating the capillary pressure distribution over water saturation for the rocktypes

To test communication between the A and C1 zones, only the C3 and C1 zones were perforated. The entire C1 zone was perforated, while only selected depths were perforated in the C3 zone.
Additionally, the model is divided into different sectors. Sectors provide information about the net flux and gas volume of that specific sector. The entire C-zone (C1, C2 and C3) has been specified as one sector, the B zone consist of three sectors (B1, B2 and B3) and the A-zone consist of one sector as well (figure 27). With this method, the volume of gas that moves out of the A zone can be tracked in each scenario, together with the fluxes out and into the B and C sectors. This method provides information from which flow behaviour, communication and the influence of certain parameters can be determined.

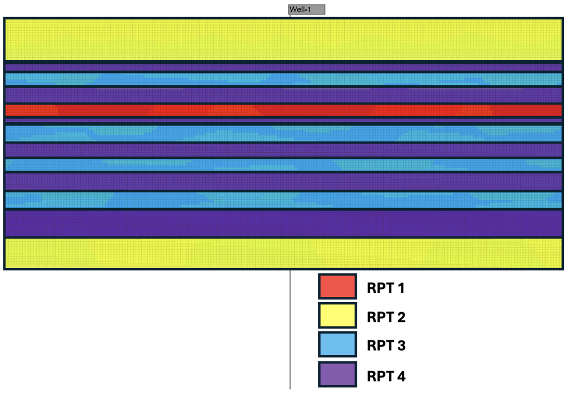

Figure 26: Overview of the rocktypes that has been assigned to the layers. RPT 1 (red) to the A zone, RPT 2 (yellow) to the A and C3 zones, and RPT 3 (blue) and RPT 4 (purple) to the B and C2 zones.

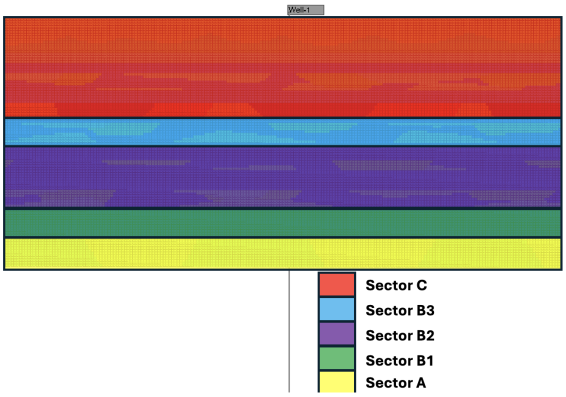

Figure 27: Overview of all the sectors that were assgined to certain layers. Sector C (red) contains the entire C zone, sectors B3 (blue), B2 (purple) and B1 (green) the B zone, and sector A (yellow) the A zone.

The initialization setting has been set to *VERTICAL which means CMG equilibrates the pressure automatically based on a single reference pressure (28). The water saturation has been uniformly defined with the *SWINIT keyword and has been set to 0.35. The pressure gradient with this setting has been defined at 2kPa/m. Additioally, the capillary pressure values were scaled by this setting in order to maintain equilibrium across the simulations. The input described above will serve as the basecase CMG code for the four RRM scenarios (figure 28). The basecase will test the influence of vertical connectivity on flow behaviour.

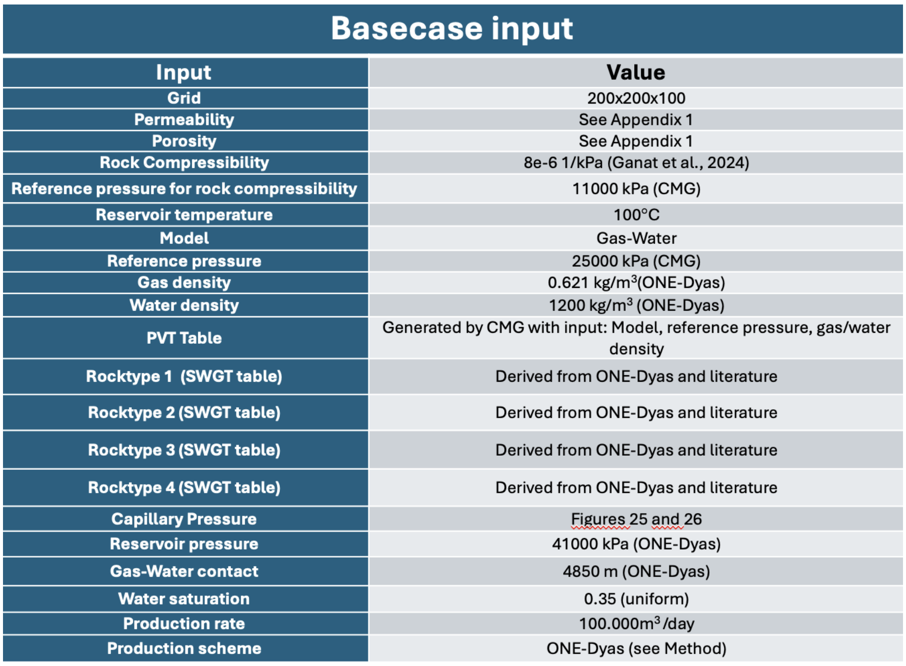

Basecase input	
Input	**Value**
Grid	200x200x100
Permeability	See Appendix 1
Porosity	See Appendix 1
Rock Compressibility	8e-6 1/kPa (Ganat et al., 2024)
Reference pressure for rock compressibility	11000 kPa (CMG)
Reservoir temperature	100°C
Model	Gas-Water
Reference pressure	25000 kPa (CMG)
Gas density	0.621 kg/m^3(ONE-Dyas)
Water density	1200 kg/m^3 (ONE-Dyas)
PVT Table	Generated by CMG with input: Model, reference pressure, gas/water density
Rocktype 1 (SWGT table)	Derived from ONE-Dyas and literature
Rocktype 2 (SWGT table)	Derived from ONE-Dyas and literature
Rocktype 3 (SWGT table)	Derived from ONE-Dyas and literature
Rocktype 4 (SWGT table)	Derived from ONE-Dyas and literature
Capillary Pressure	Figures 25 and 26
Reservoir pressure	41000 kPa (ONE-Dyas)
Gas-Water contact	4850 m (ONE-Dyas)
Water saturation	0.35 (uniform)
Production rate	100.000m^3 /day
Production scheme	ONE-Dyas (see Method)

Figure 28: Table containing the input for the basecase simulations in CMG IMEX.

In addition, on the four basecase scenarios,s further sensitivity simulations were carried out to systematically investigate which model parameters influence and determine vertical cross-flow and recharge behaviour between the A and C1 zones. Five parameters are varied to test their influence on flow behaviour:

- Vertical Permeability (Applied to the B- and C2-zones)
- Porosity (Applied to the B- and C2-zones)
- Initial Water Saturation (Applied to the B- and C2-zones)
- Capillary Pressure (Applied to all rocktypes)
- Residual gas saturation (Applied to all rocktypes)

The five parameters were independently varied in the .dat file, which was then simulated with IMEX. The effects of porosity, permeability, and water saturation are evaluated using multipliers. The vertical permeability was multiplied with the help of the TRANSK keyword. The porosity was scaled by 0.1 and 4 and this has been done with the MOD IJK keyword. The vertical permeability has been multiplied by 0.1, 10 and 100 to investigate the influence of increasing vertical permeability. Since vertical crossflow and communication between the A and C1 zones are primarily controlled by the properties of the B zone, vertical permeability and water saturations are only varied within the B zone.
The sensitivity analysis of vertical permeability and porosity was performed only for Scenario 4. The initial water saturation parameters is also manually adjusted for the other three scenarios, but for scenario 4 an extra run will be done to observe the trend of increased SW. An overview of the ranges of each parameter are given in figure 29.

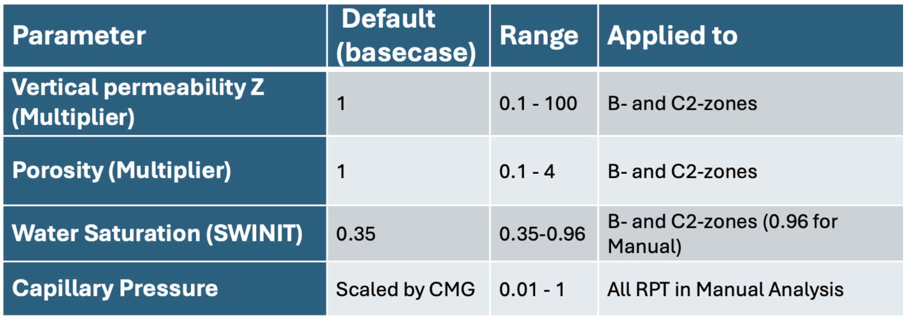

Parameter	Default (basecase)	Range	Applied to
Vertical permeability Z (Multiplier)	1	0.1 - 100	B- and C2-zones
Porosity (Multiplier)	1	0.1 - 4	B- and C2-zones
Water Saturation (SWINIT)	0.35	0.35-0.96	B- and C2-zones (0.96 for Manual)
Capillary Pressure	Scaled by CMG	0.01 - 1	All RPT in Manual Analysis

Figure 29: Table containing the parameters which are used for the sensitivity analyses

In addition to the sensitivity analyses mentioned above, an additional set of manual sensitivity analyses will be conducted for all scenarios to test the influence of capillary pressure on gas movement. First for the calculated capillary pressures, and then for the calculated pressure multiplied by 0.01. The calculated pressure will from now on be called normal capillary pressure. Furthermore, the influence of residual gas saturation will be tested manually through an additional simulation in scenario 4.
Additionally, to assess the impact of geological architecture and heterogeneity on flow behavior, an additional simulation was conducted in which the average permeability of each non-continuous layer from Scenario 4 was calculated and then assigned uniformly across the respective layers (figure 20). This approach removes the spatial variability associated with discrete architectural elements, while preserving the overall average permeability. By comparing this model to Scenario 4, it becomes possible to evaluate whether the spatial distribution of high-permeability features, rather than just their average properties, has a significant influence on gas flow and pressure redistribution.

An aquifer is added to the model to supply a realistic source of water. Two Fetkovich aquifers were implemented in the producing zones with a productivity index of 0.04 (C3) and 0.05 stb/day/psi (C1). This has been done to prevent the simulator from 'inventing' water through rock and fluid compressibility.

Although this modeling framework provides valuable information on potential stratigraphic communication, several limitations apply. Structural heterogeneities, such as micro-faults and small-scale fractures, were not included. Therefore, the results of the simulations should be interpreted as qualitative indicators of stratigraphic influence on flow behavior rather than as predictive forecasts. Additional simplifications and assumptions are outlined in Chapter 4.3.

4.3 Assumptions

During the construction of the models in RRM, several assumptions had to be made in order to construct realistic scenarios. Each assumption applies to all models. In case a scenario is explicit mentioned in a certain assumption, it applies to that scenario only. For justifications for the assumptions, see appendix.

4.3.1 RRM Assumptions

Assumption 1: Horizontal boundary surfaces
In reality, well data from the L11 block indicate a trend of shallower depths of the zones toward the south and east. This trend is more pronounced in the southward direction. For modelling purposes, this depth trend has been neglected, and all zone boundaries are assumed to be horizontal.

Assumption 2: Uniform thickness across zones
No consistent trend in thickness variation has been observed within the L11 block. While minor local variations in zone thickness exist across the area due to depositional processes, accommodation space, or structural influence, the model assumes each zone has a constant thickness.

Assumption 3: One Sketched Channel Represents Multiple Stacked Channels
In the model a single sketched channel may represent multiple stacked channels deposited over different timescales but in the same location for the A, C1 and C3 zones. These channels (sand layers) are separated by baffles (mud/clay drapes) that locally affect porosity and vertical permeability.

Assumption 4: Uniform channel trajectory and extent
Since the depositional environment is assumed to be consistent over time per zone, elements (crevasses and channels) are assumed to follow the same trajectory and continue beyond the model boundaries.

Assumption 5: TopA and C1 zones fully channelized with four channel types
The TopA and C1 zones are interpreted as fan environments. For modelling, they are assumed to consist entirely of channel deposits conform assumption 3: each channel may represent multiple channels of sand layers separated by baffles. Four types of channels are used to reflect varying degrees of heterogeneity induced by baffle content, ranging from moderate/good to excellent petrophysical properties.

Assumption 6: Two-layered channel structure C3 zone
The C3 zone is interpreted as distal fan deposits. These start with crevasse splays embedded in a low-quality matrix, followed by upward-coarsening channels. In the model, this is represented by two channel layers: the lower channels of finer sand and an upper channel of coarser sand, each with distinct reservoir properties. In this model, the base of the C3 zone is assumed to completely consist of crevasses overlaid by finer and coarser sandstones respectively.

Assumption 7: Fan front zones with variable vertical connectivity
Parts of the B and C2 zones are interpreted as fan front environments, consisting of crevasses and channels embedded in a muddy matrix. Well correlations show spatial variability in the presence of channels and crevasses. Four modelling scenarios are defined based on the degree of vertical connectivity between these elements in the B and C2 zones, ranging from connectivity (three points) to no connectivity between the elements. For the elements the best observed properties (derived from the B well data and their corresponding properties in the Por-Perm excel sheet), are chosen (see Method RRM chapter for further explanation).

Assumption 8: Use of Averaged Vertical Permeability and Porosity Values
Vertical permeability (Kv) and porosity values were provided by ONE-Dyas in the form of an Excel dataset, with measurements taken at regular 0.152 m intervals. To assign reservoir properties to regions within the RRM models, average Kv and porosity values were calculated per unit. For example, if a modeled layer within the B zone corresponds to 40 measured intervals in the dataset, the average of those 40 values was used to define the Kv and porosity of that layer in the model.

Assumption 9: Property Assignment Based on Channel Volume in the A and C1 Zones
In the channel-dominated A and C1 zones, four different channel types are distinguished, each with varying

volumes. For each channel type, average vertical permeability (Kv) and porosity values were calculated and assigned based on the relative volume the channel occupies within the zone. Specifically, the channel with the highest volume is assigned the highest permeability and porosity values, while the channel with the smallest volume receives the lowest values.

Assumption 10: Uniform Reservoir Properties Assigned to All Interpreted Crevasses
Within the well log of the B zone, a crevasse deposit was identified at a specific depth, where notably high vertical permeability (Kv) and porosity values were measured. In the model, all interpreted crevasse elements across the relevant zones (B and C2) are assigned the same reservoir properties as observed at this location.

Assumption 11: Uniform Reservoir Properties Assigned to All Interpreted Channels
Within the well log of the C2 zone, a channel deposit was identified at a specific depth, where notably high vertical permeability (Kv) and porosity values were measured. In the model, all interpreted crevasse elements across the relevant zones (B and C2) are assigned the same reservoir properties as observed at this location.

Assumption 12: Uniform Porosity Assigned to All Top A Channel Types
In the model, all four channel types within the Top A zone have been assigned the same porosity value.

Assumption 13: Exaggerated Element Dimensions for Modelling Purposes
In the model, architectural elements such as channels and crevasse splays are sketched slightly larger than they are likely to be.

Assumption 14: Fixed Properties for the A, C1, and C3 Zones Across All Scenarios
In all modelling scenarios, the A, C1, and C3 zones are kept constant in terms of geometry and reservoir properties. No internal variation is introduced between scenarios.

Assumption 15: Consistent Mud Layer Distribution in the B Zone Across All Scenarios
In all scenarios, the continuous mud rich layers within the B and C2 zones are assumed to be laterally continuous and consistent.

4.3.2 CMG Assumptions

Assumption 16: Uniform water saturation across the entire model
The water saturation is set to be equal at the start of the simulation (0.35).

Assumption 17: Constant production rate of 100,000 m^3/day during production periods

Assumption 18: Only the C1 and C3 zones are perforated; the A zone is left unperforated

Assumption 19: Zones are assigned distinct rock types based on lithological and petrophysical properties

Assumption 20: The capillary pressure curves are scaled by CMG for the Basecase simulations

Assumptions 21: Krg Gas mobility has been set to $SW<1.0$ for the Basecase simulations

5 Results

Results are obtained from two types of software: RRM and Computer Modeling Group (CMG) - IMEX. RRM provides the four connectivity scenarios and CMG provides flow simulations of those four scenarios.

5.1 Rapid Reservoir Modeling

The RRM models are sketched in 2D and in 3D and for each scenario, three screenshots of different cross sections are added to show the 3D trajectories and element evolution of the models: at 64NS (outer boundary), 32NS (center) and 0NS (outer boundary). To provide a clearer and more detailed overview of the elements and 3D trajectories, the models have been vertical exaggerated by factor 4. For an overview of the property values of the layers/architectural elements, 10 1 can be used.

5.1.1 Scenario 1

In the first scenario, the noncontinuous layers (figure 20) are vertically connected by architectural elements at three points (e.g. channels and/or crevasses). The connected architectural elements create vertical connected pathways within the layer. Figures 30 to 32 show the first scenario. The scenario starts at the base with the A zone consisting of four types of channels with varying properties (green). The A zone is overlain by the B zone which starts with a mud layer, marked in red. This mud layer is followed up by a sequence of three layers consisting of mud-rich deposits (blue) with architectural sand-rich elements (yellow and orange) alternated by two mud-rich layers without architectural elements (grey). The architectural sand rich elements are vertically connected on three locations. On top of the B zone, the C1 zone is marked which mainly consist of four types of channels with varying properties. The mud-rich deposits (blue) with architectural elements (orange and yellow) and the mud-rich layer (grey) illustrate the C2 layer. The sequence ends with the C3 starting with crevasses (orange) and followed by two types of channels (green).

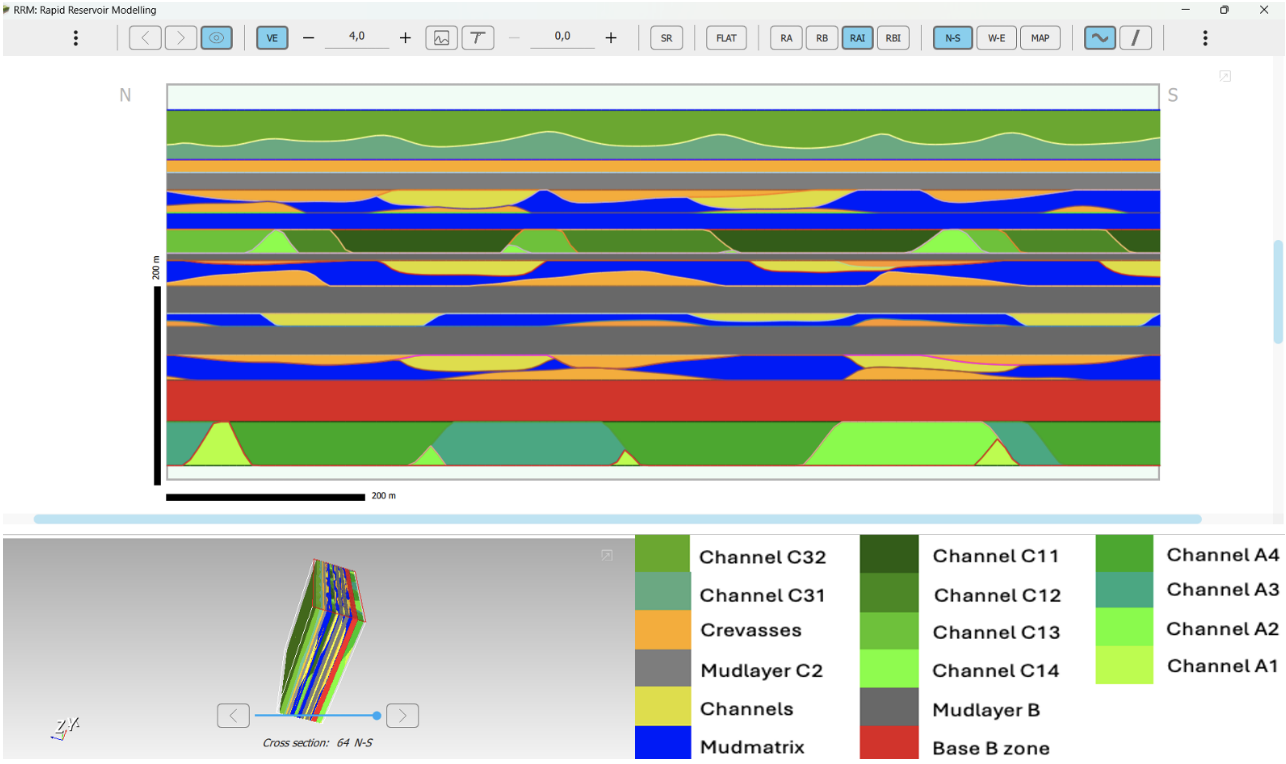

Figure 30: Scenario 1 in cross-section NS64, with three vertical connectivity zones in the non-continuous layers

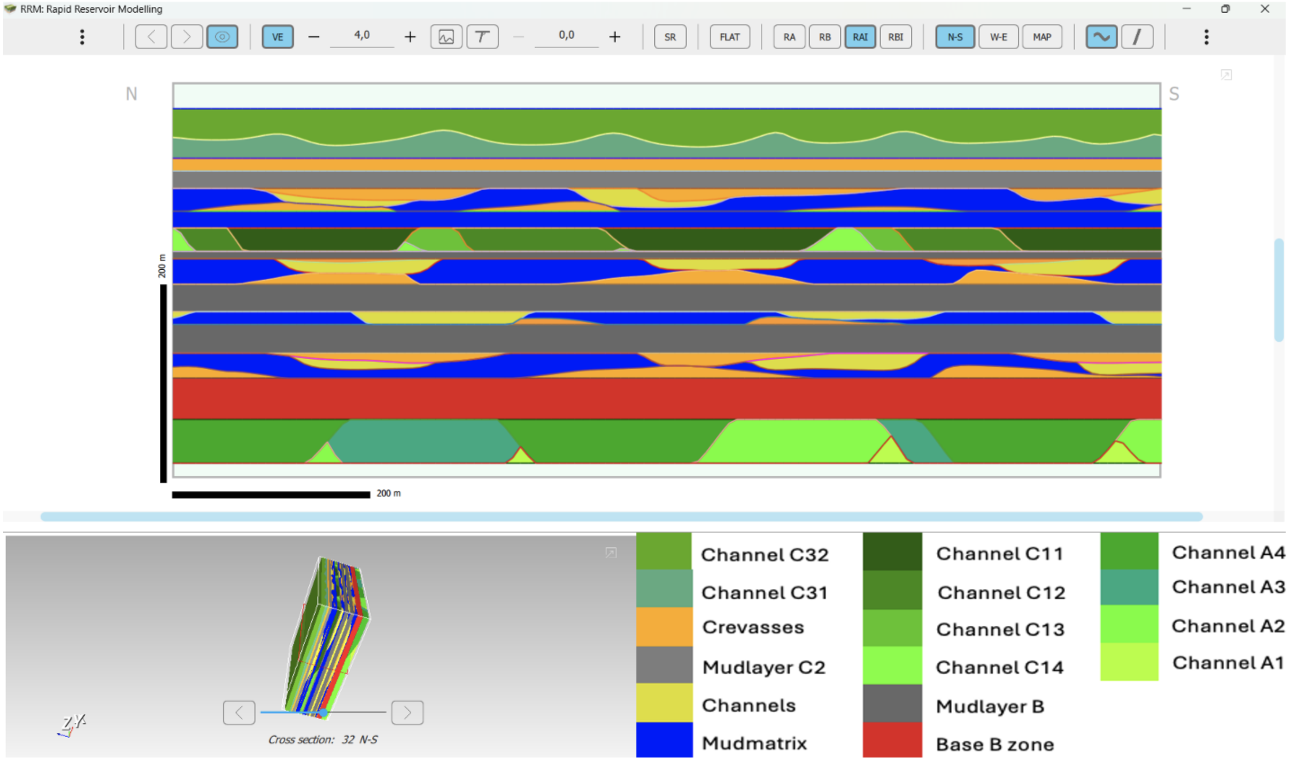

Cross section: 32 N-S

Figure 31: Scenario 1 in cross-section NS32, with three vertical connectivity zones in the non-continuous layers

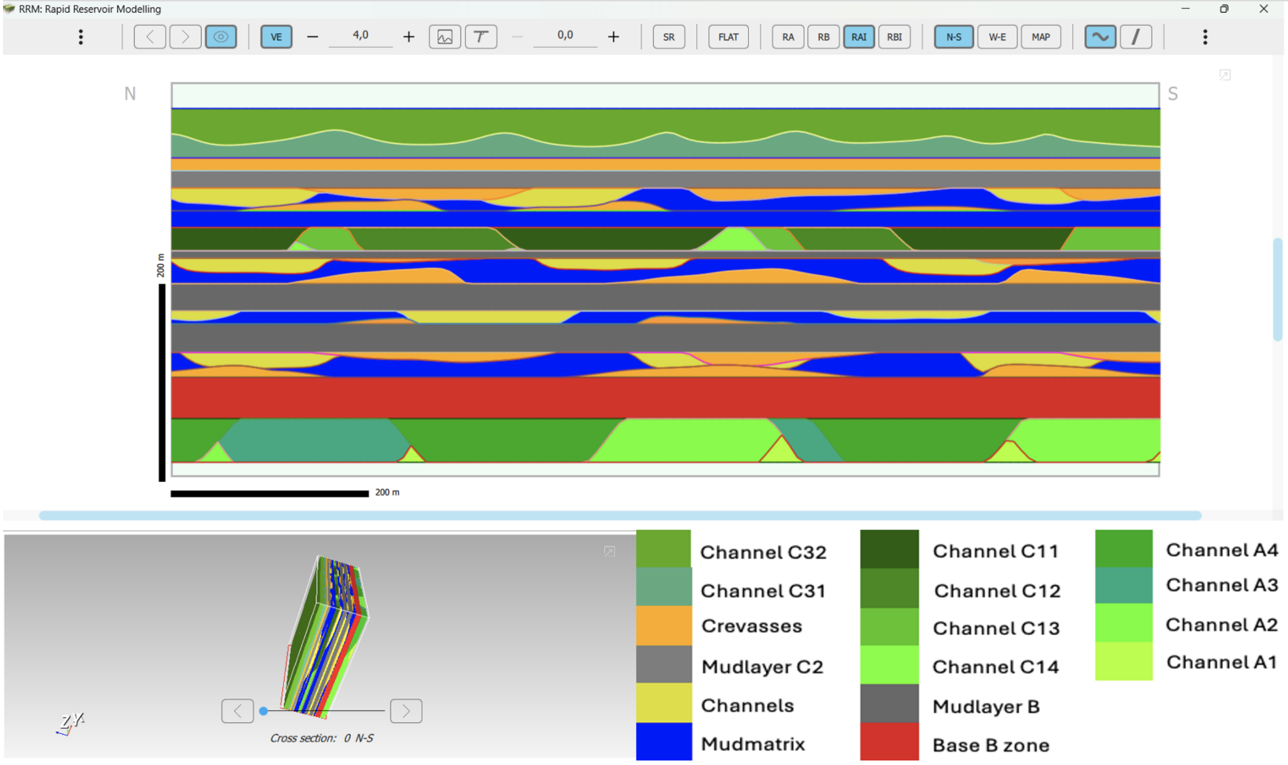

Cross section: 0 N-S

Figure 32: Scenario 1 in cross-section NS0, with three vertical connectivity zones in the non-continuous layers

5.1.2 Scenario 2

In the second scenario, the noncontinuous layers (figure 20) are vertically connected by architectural elements at two points (e.g. channels and/or crevasses). The connected architectural elements create vertical connected pathways within the layer. Figures 33 to 35 show the second scenario. The scenario starts at the base with the A zone consisting of four types of channels with varying properties (green). The A zone is overlain by the B zone which starts with a mud layer, marked in red. This mud layer is followed up by a sequence of three layers consisting of mud-rich deposits (blue) with architectural sand-rich elements (yellow and orange) alternated by two mud-rich layers without architectural elements (grey). The architectural sand rich elements are vertically connected on two locations. On top of the B zone, the C1 zone is marked which mainly consist of four types of channels with varying properties. The mud-rich deposits (blue) with architectural elements (orange and yellow) and the mud-rich layer (grey) illustrate the C2 layer. The sequence ends with the C3 starting with crevasses (orange) and followed by two types of channels (green).

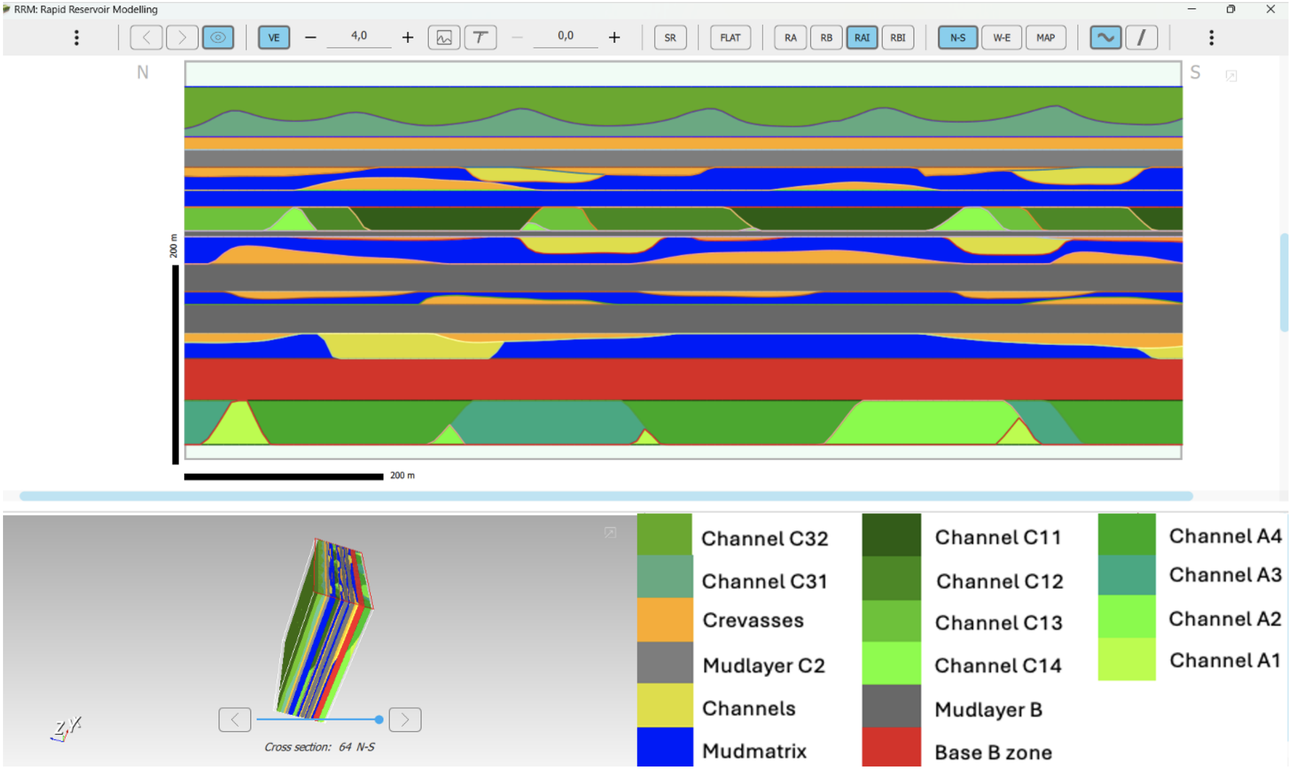

Figure 33: Scenario 2 in cross-section NS64, with two vertical connectivity zones in the non-continuous layers

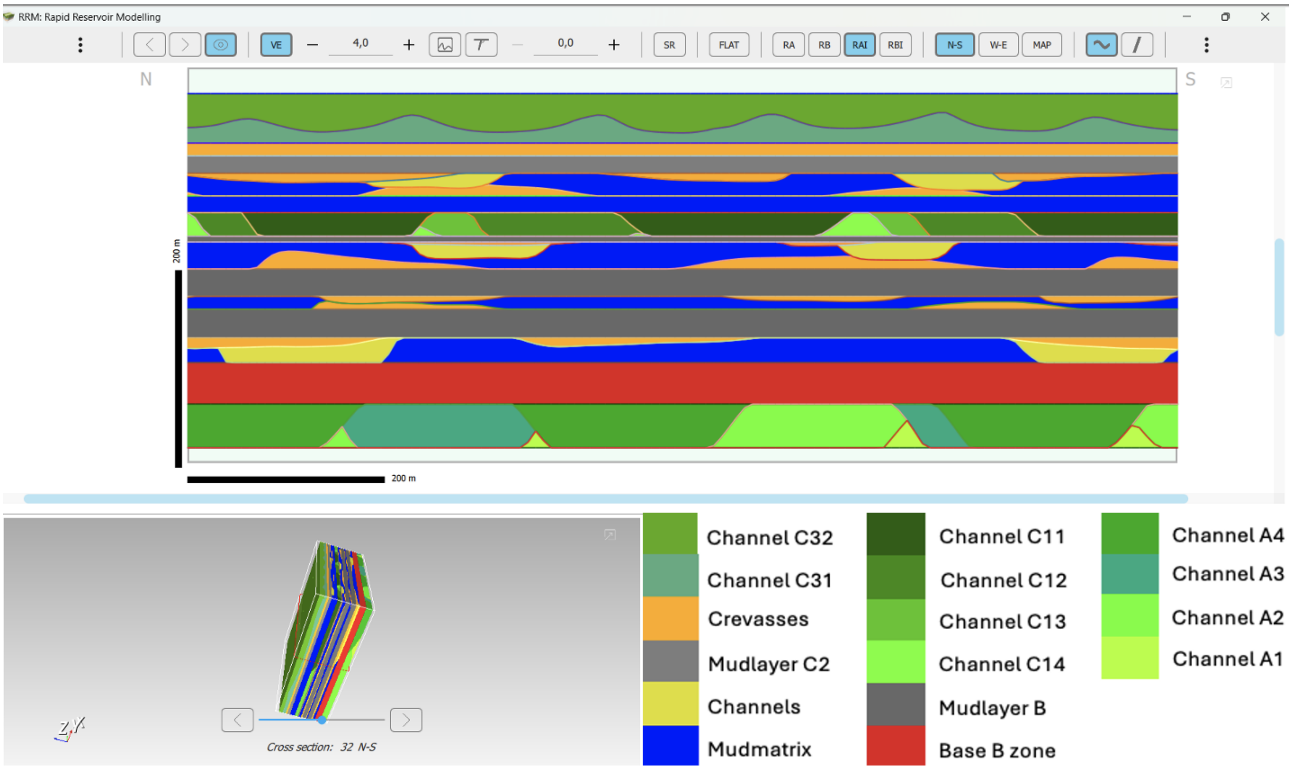

Figure 34: Scenario 2 in cross-section NS32, with two vertical connectivity zones in the non-continuous layers

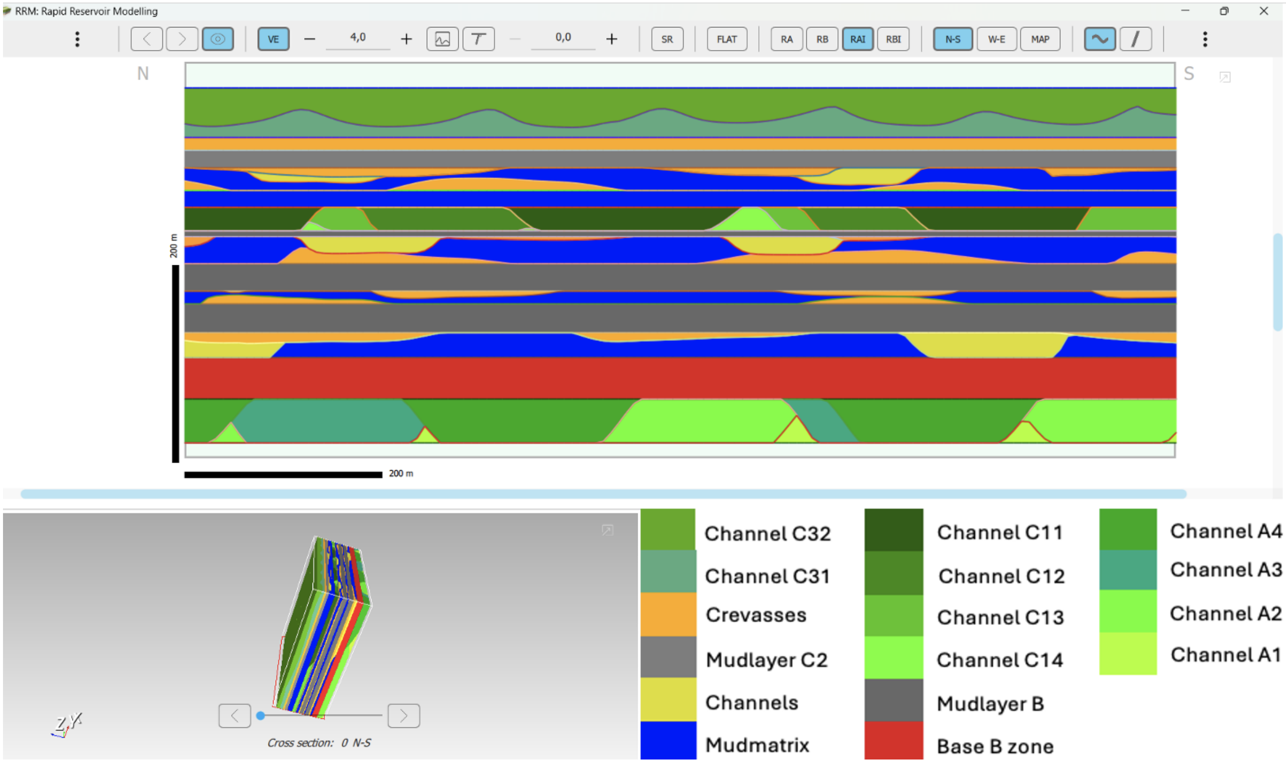

Figure 35: Scenario 2 in cross-section NS0, with two vertical connectivity zones in the non-continuous layers

5.1.3 Scenario 3

In the third scenario, the non continuous layers (figure 20) are vertically connected by architectural elements at one points (e.g. channels and/or crevasses). The connected architectural elements create vertical connected pathways within the layer. Figures 36 to 38 show the third scenario. The scenario starts at the base with the A zone consisting of four types of channels with varying properties (green). The A zone is overlain by the B zone which starts with a mud layer, marked in red. This mud layer is followed up by a sequence of three layers consisting of mud-rich deposits (blue) with architectural sand-rich elements (yellow and orange) alternated by two mud-rich layers without architectural elements (grey). The architectural sand-rich elements are vertically connected on one location. On top of the B zone, the C1 zone is marked which mainly consist of four types of channels with varying properties. The mud-rich deposits (blue) with architectural elements (orange and yellow) and the mud-rich layer (grey) illustrate the C2 layer. The sequence ends with the C3 starting with crevasses (orange) and followed by two types of channels (green).

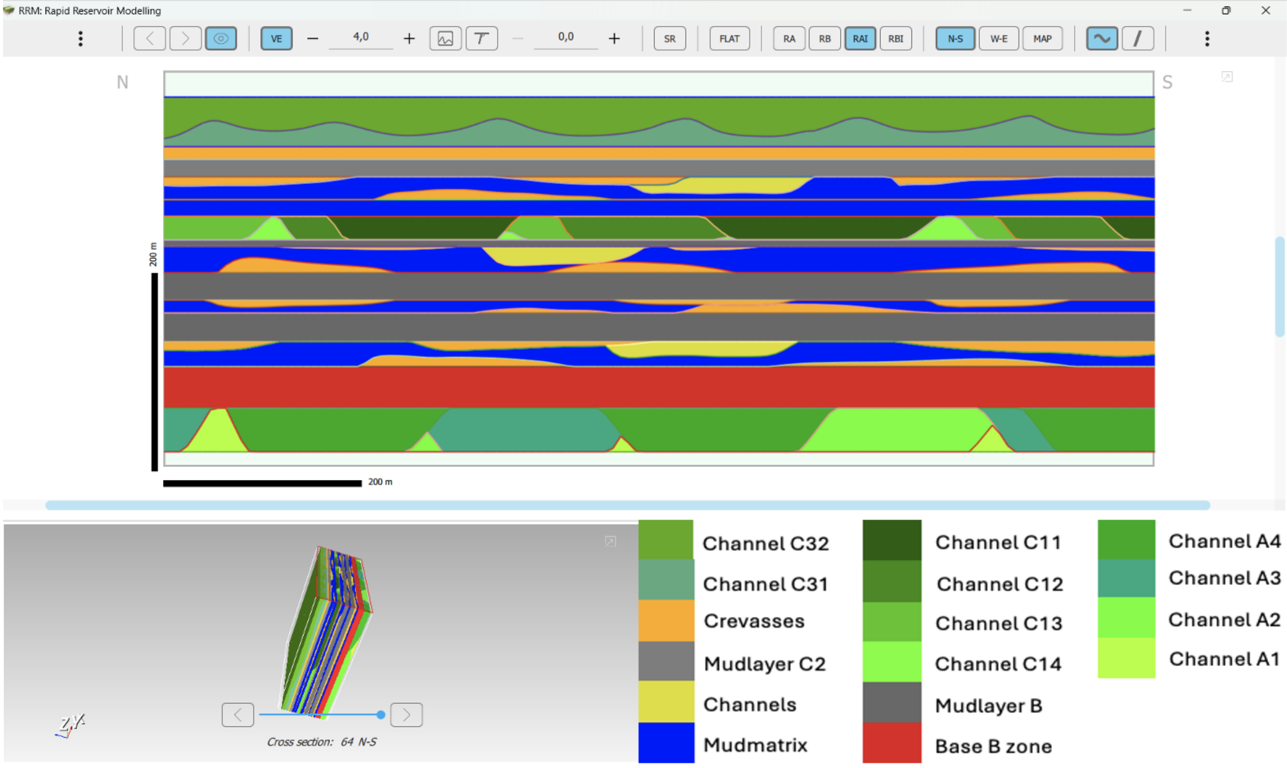

Figure 36: Scenario 3 in cross-section NS64, with one vertical connectivity zone in the non-continuous layers

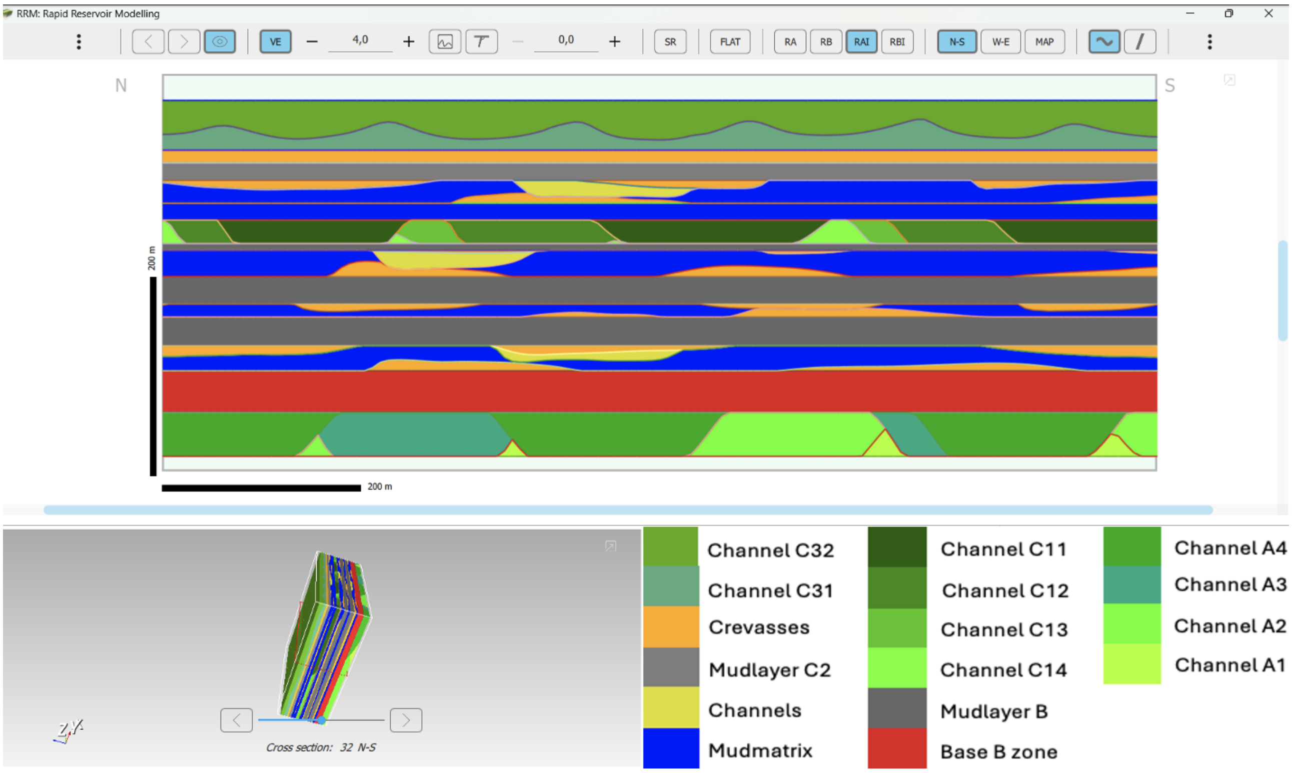

Figure 37: Scenario 3 in cross-section NS32, with one vertical connectivity zone in the non-continuous layers

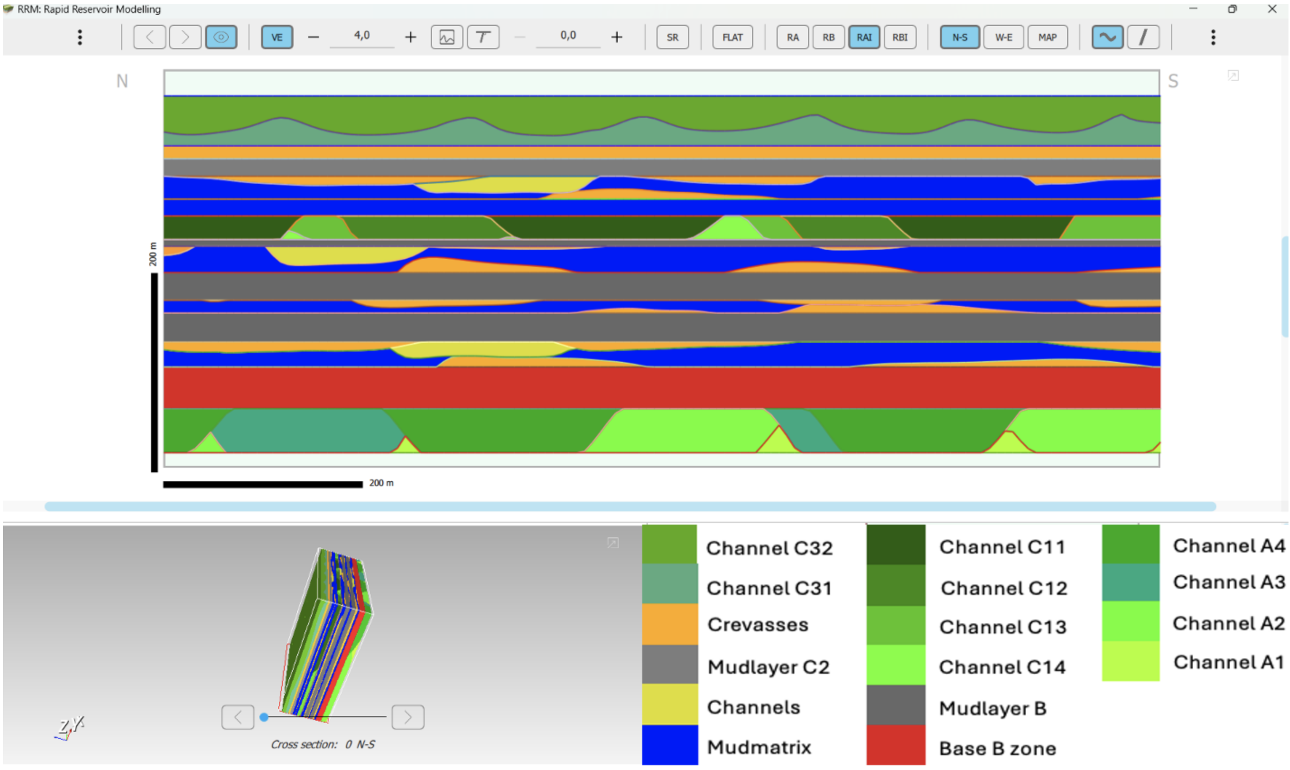

Figure 38: Scenario 3 in cross-section NS0, with one vertical connectivity zone in the non-continuous layers

5.1.4 Scenario 4

In the fourth scenario, the non continuous layers (figure 20) are not vertically connected by architectural elements (e.g. channels and/or crevasses). The connected architectural elements create vertical connected pathways within the layer. Figures 39 to 41 show the fourth scenario. The scenario starts at the base with the A zone consisting of four types of channels with varying properties (green). The A zone is overlain by the B zone which starts with a mud layer, marked in red. This mud layer is followed by a sequence of three layers consisting of mud-rich deposits (blue) with architectural sand-rich elements (yellow and orange) alternated by two mud-rich layers without architectural elements (grey). The architectural sand-rich elements are not vertically connected. On top of the B zone, the C1 zone is marked, which mainly consists of four types of channels with varying properties. The mud-rich deposits (blue) with architectural elements (orange and yellow) and the mud-rich layer (grey) illustrate the C2 layer. The sequence ends with the C3 starting with crevasses (orange) and followed by two types of channels (green).

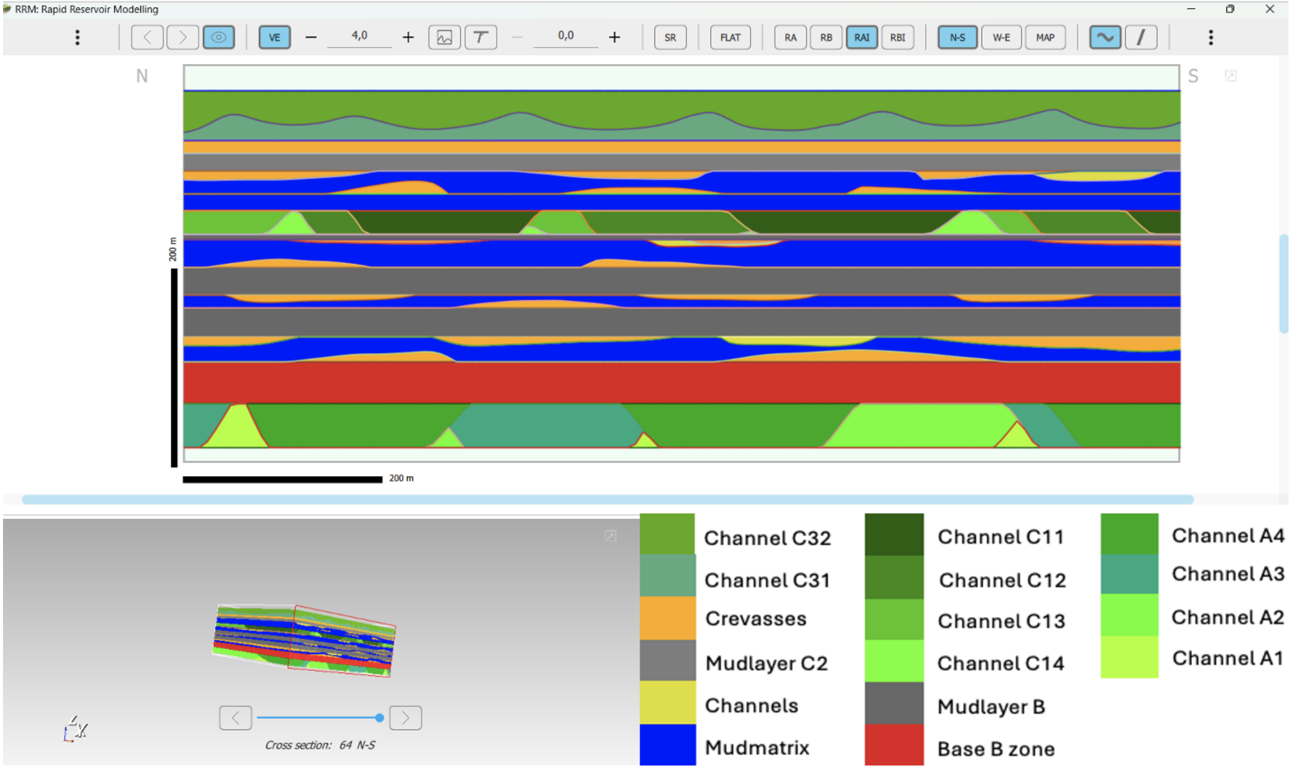

Figure 39: Scenario 4 in cross-section NS64, with no vertical connectivity in the non-continuous layers

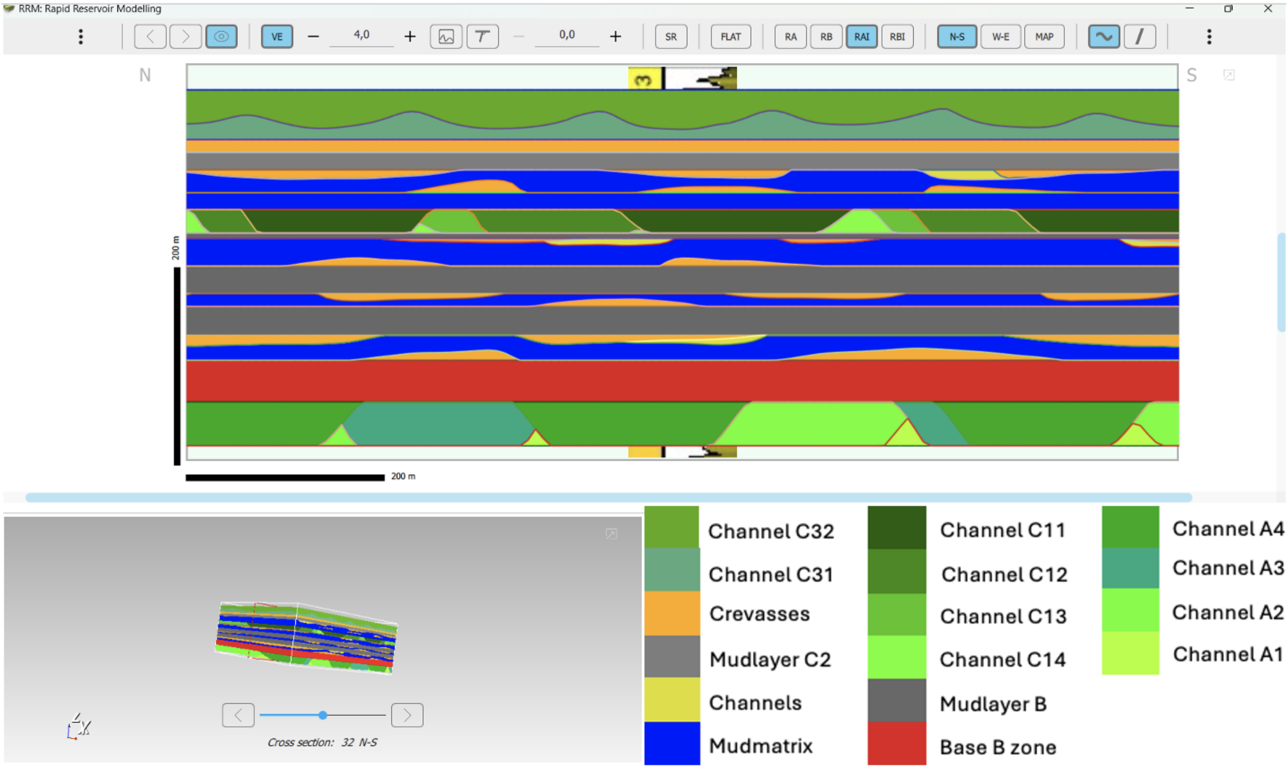

Figure 40: Scenario 4 in cross-section NS32, with no vertical connectivity in the non-continuous layers

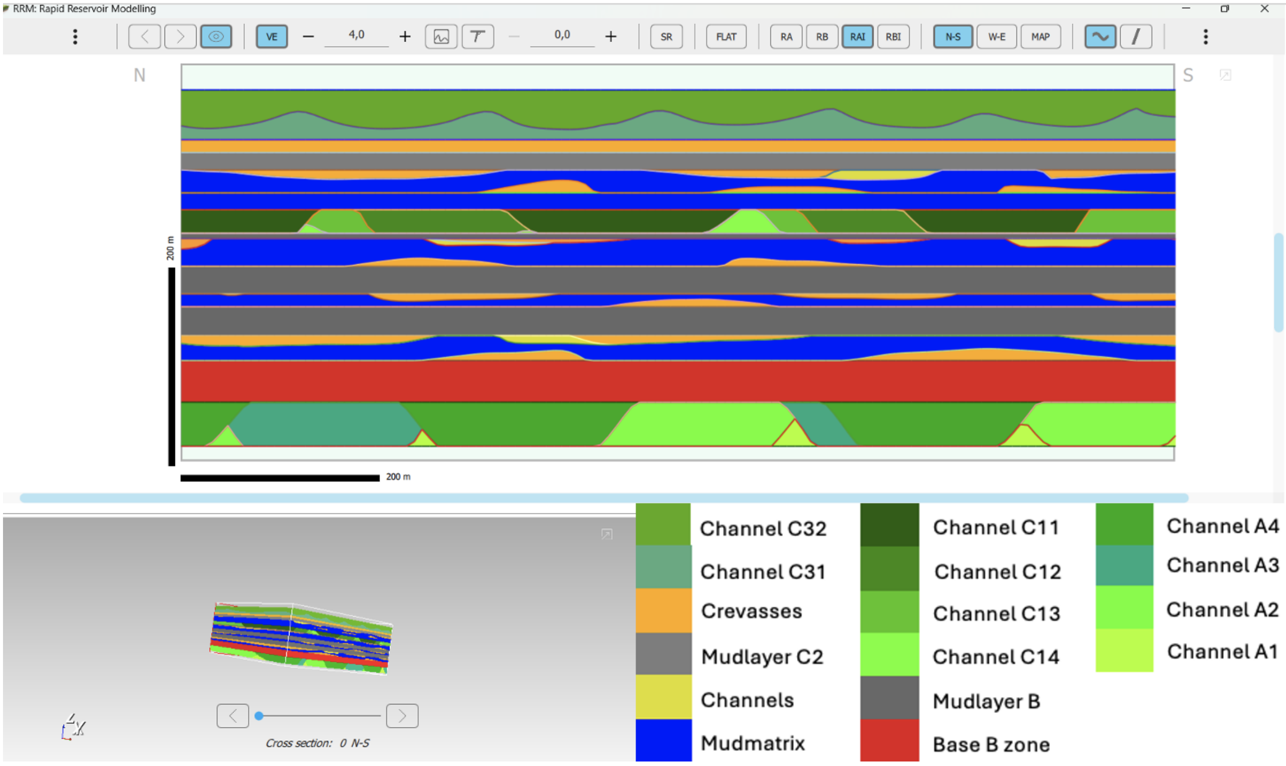

Figure 41: Scenario 4 in cross-section NS0, with no vertical connectivity in the non-continuous layers

5.2 Computer Modeling Group: Basecase

The results are obtained with CMG-IMEX simulations and are visualized in CMG Results. The simulations provide visualizations and graphs and the most important ones will be given in this section. In this chapter, some timeseries of Gas Volume, Free Gas Volume Cumulative Flux-Sector and Average Pressure will be provided for the different sectors. Flux refers to the amount of gas that has moved passed the boundaries of two adjacent sectors. The results can be found for scenario 1 in figures 43 to 45, scenario 2 in figures 46 to 48, scenario 3 in figures 49 to 51 and for scenario 4 in figures 52 to 54. For a more detailed overview of the water saturation and pressure distribution, screenshots of the simulations of these distributions over time are given in the Appendix (10) to keep the Results section clear and structured. In this chapter, the following graphs will be given: Total Cumulative Gas Volume (In)Flux-Sector of C-sector, B1 to A sectors, Average Pressure of the entire field and Gas volumes of sector C and A. The graphs containing the timeseries of Gas Volume, Free Gas Volume Cumulative Flux-Sector and Average Pressure will provide a quantitative overview of flow behavior, communication between the zones and the possibility of recharge of the C1 zone by the A zone. Figure 42 shows a compact summary table in which all key outcomes are summarized.

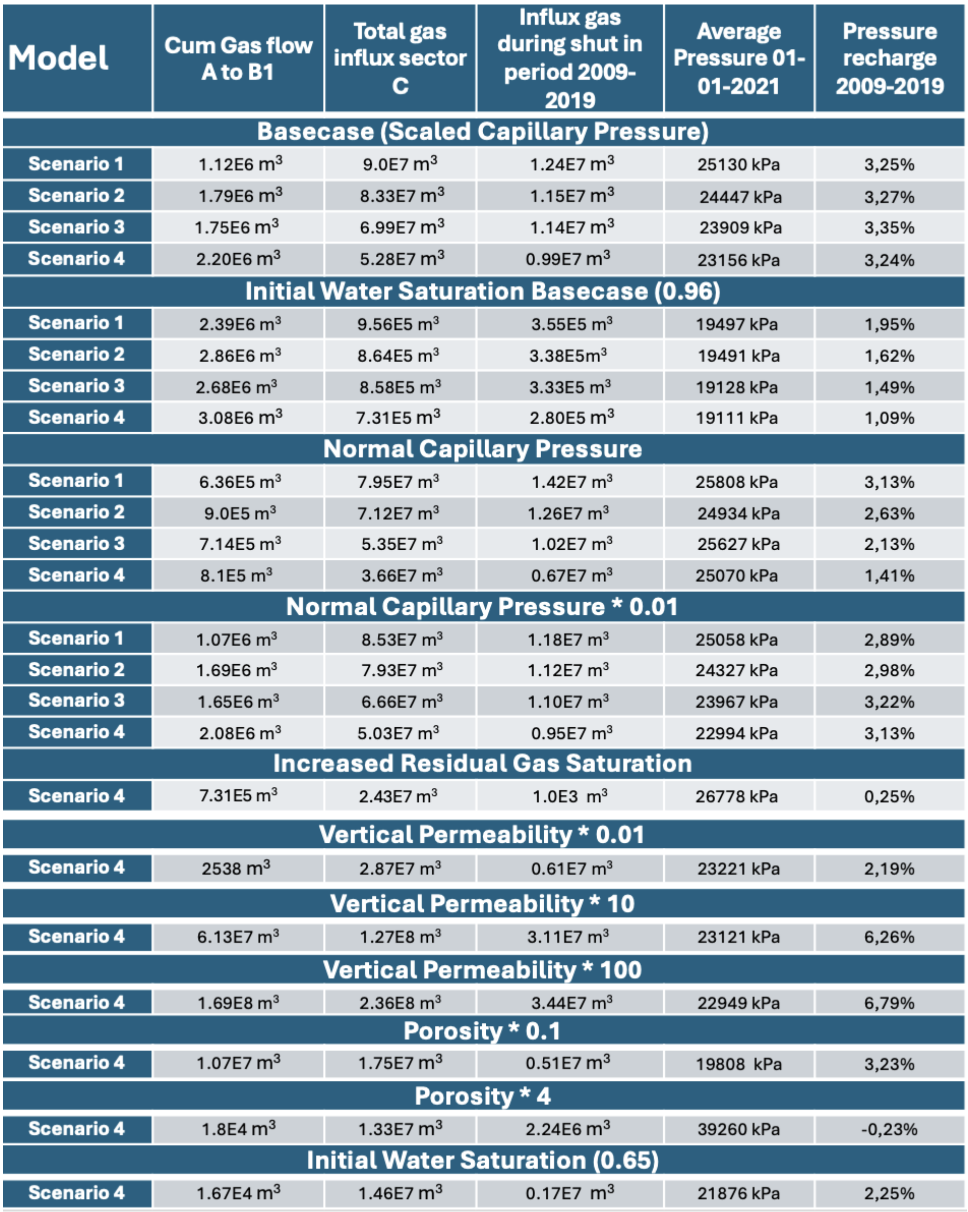

Model	Cum Gas flow A to B1	Total gas influx sector C	Influx gas during shut in period 2009-2019	Average Pressure 01-01-2021	Pressure recharge 2009-2019
Basecase (Scaled Capillary Pressure)					
Scenario 1	1.12E6 m^3	9.0E7 m^3	1.24E7 m^3	25130 kPa	3,25%
Scenario 2	1.79E6 m^3	8.33E7 m^3	1.15E7 m^3	24447 kPa	3,27%
Scenario 3	1.75E6 m^3	6.99E7 m^3	1.14E7 m^3	23909 kPa	3,35%
Scenario 4	2.20E6 m^3	5.28E7 m^3	0.99E7 m^3	23156 kPa	3,24%
Initial Water Saturation Basecase (0.96)					
Scenario 1	2.39E6 m^3	9.56E5 m^3	3.55E5 m^3	19497 kPa	1,95%
Scenario 2	2.86E6 m^3	8.64E5 m^3	3.38E5m^3	19491 kPa	1,62%
Scenario 3	2.68E6 m^3	8.58E5 m^3	3.33E5 m^3	19128 kPa	1,49%
Scenario 4	3.08E6 m^3	7.31E5 m^3	2.80E5 m^3	19111 kPa	1,09%
Normal Capillary Pressure					
Scenario 1	6.36E5 m^3	7.95E7 m^3	1.42E7 m^3	25808 kPa	3,13%
Scenario 2	9.0E5 m^3	7.12E7 m^3	1.26E7 m^3	24934 kPa	2,63%
Scenario 3	7.14E5 m^3	5.35E7 m^3	1.02E7 m^3	25627 kPa	2,13%
Scenario 4	8.1E5 m^3	3.66E7 m^3	0.67E7 m^3	25070 kPa	1,41%
Normal Capillary Pressure * 0.01					
Scenario 1	1.07E6 m^3	8.53E7 m^3	1.18E7 m^3	25058 kPa	2,89%
Scenario 2	1.69E6 m^3	7.93E7 m^3	1.12E7 m^3	24327 kPa	2,98%
Scenario 3	1.65E6 m^3	6.66E7 m^3	1.10E7 m^3	23967 kPa	3,22%
Scenario 4	2.08E6 m^3	5.03E7 m^3	0.95E7 m^3	22994 kPa	3,13%
Increased Residual Gas Saturation					
Scenario 4	7.31E5 m^3	2.43E7 m^3	1.0E3 m^3	26778 kPa	0,25%
Vertical Permeability * 0.01					
Scenario 4	2538 m^3	2.87E7 m^3	0.61E7 m^3	23221 kPa	2,19%
Vertical Permeability * 10					
Scenario 4	6.13E7 m^3	1.27E8 m^3	3.11E7 m^3	23121 kPa	6,26%
Vertical Permeability * 100					
Scenario 4	1.69E8 m^3	2.36E8 m^3	3.44E7 m^3	22949 kPa	6,79%
Porosity * 0.1					
Scenario 4	1.07E7 m^3	1.75E7 m^3	0.51E7 m^3	19808 kPa	3,23%
Porosity * 4					
Scenario 4	1.8E4 m^3	1.33E7 m^3	2.24E6 m^3	39260 kPa	-0,23%
Initial Water Saturation (0.65)					
Scenario 4	1.67E4 m^3	1.46E7 m^3	0.17E7 m^3	21876 kPa	2,25%

Figure 42: Table showing a compact summary of the key outcomes and results obtained with CMG IMEX simulations and the Manual Sensitivity Analysis

5.2.1 Scenario 1 Basecase

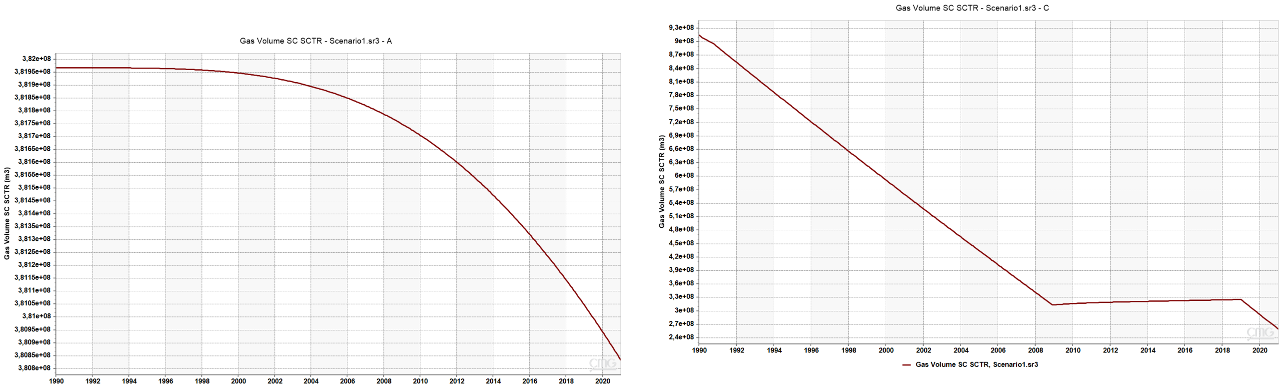

(a) Graph showing the gas volume of the A-sector (A-zone) in Scenario 1

(b) Graph showing the gas volume of the C-sector in Scenario 1. As seen, the gas volume decreases due to production and increases during shut-in period.

Figure 43: Graphs of the gas volumes of sectors A (a) and C (b) in scenario 1

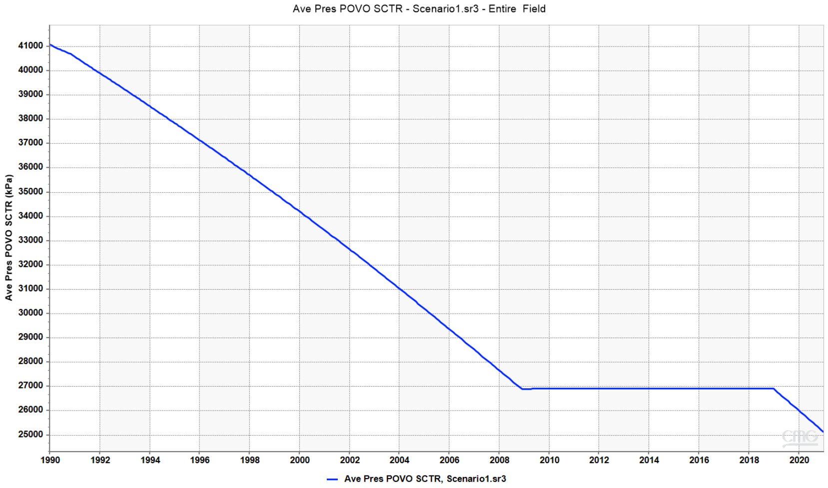

Figure 44: Graph showing the average pressure decline across the entire model for the first Scenario.

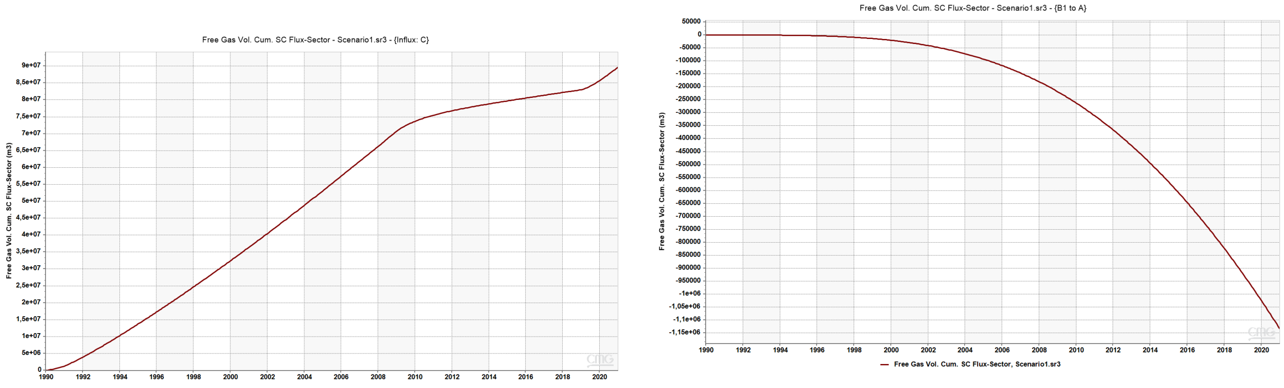

(a) Graph illustrating the cumulative gas volume that has entered the C-sector over time

(b) Graph illustrating the cumulative gas volume flux from the B1-sector into the A-sector. The negative numbers mean a flux from A to B1

Figure 45: Graphs of the total cumulative gas volume over time entering the C-sector and moving from the B1-sector into the A-sector in scenario 1.

5.2.2 Scenario 2 Basecase

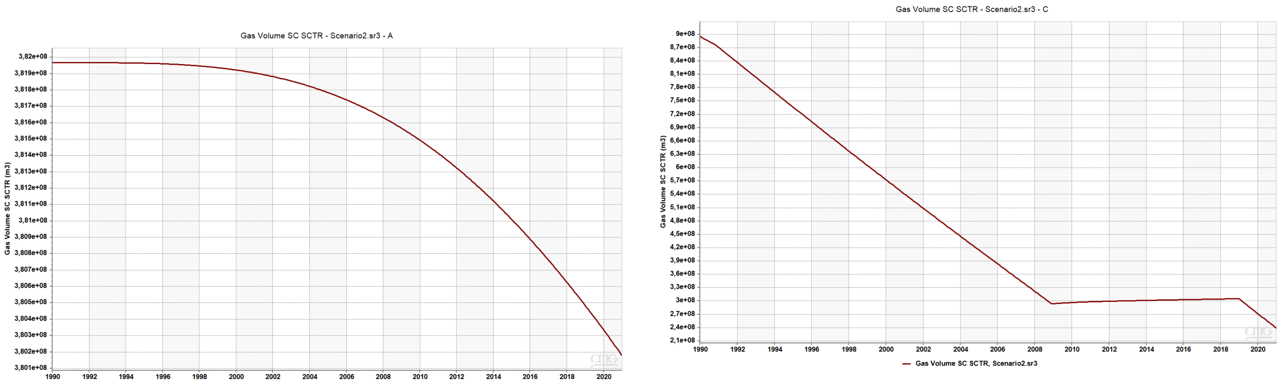

(a) Graph showing the gas volume of the A-sector (A-zone) in Scenario 2

(b) Graph showing the gas volume of the C-sector in Scenario 2. As seen, the gas volume decreases due to production and increases during shut-in period.

Figure 46: Graphs of the gas volumes of sectors A (a) and C (b) in scenario 2

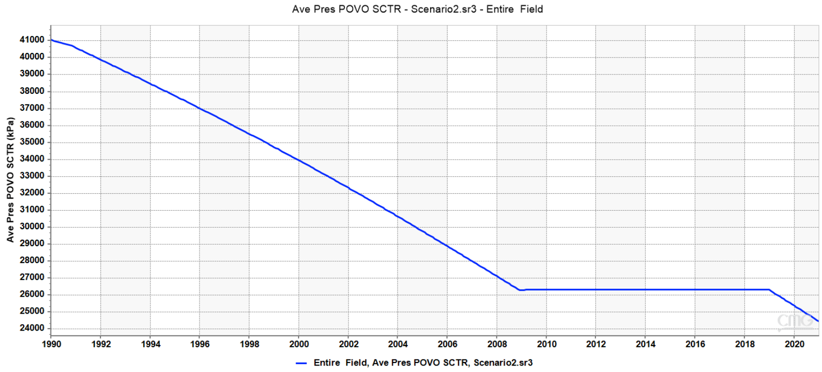

Figure 47: Graph showing the average pressure decline across the entire model for the second scenario

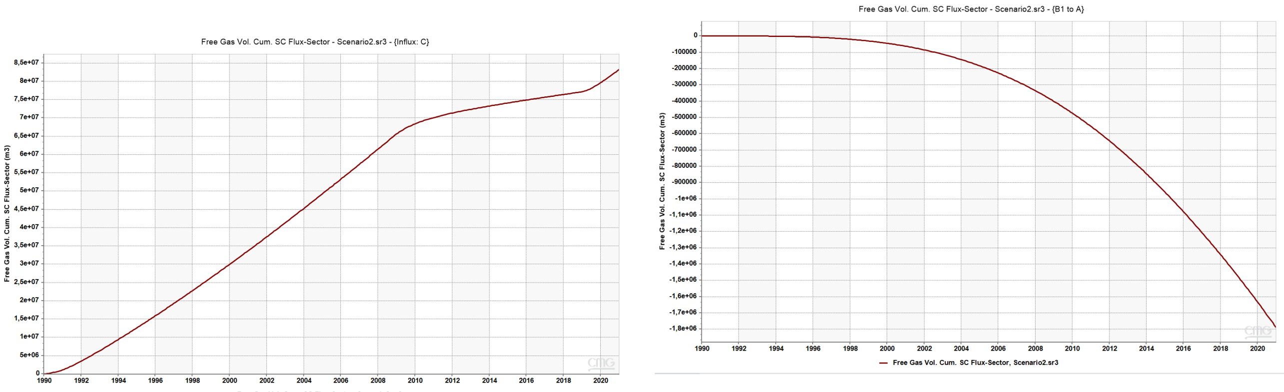

(a) Graph illustrating the cumulative gas volume that has entered the C-sector over time

(b) Graph illustrating the cumulative gas volume flux from the B1-sector into the A-sector. The negative numbers mean a flux from A to B1

Figure 48: Graphs of the total cumulative gas volume over time entering the C-sector (a) and moving from the B1-sector into the A-sector (b) in scenario 2

5.2.3 Scenario 3 Basecase

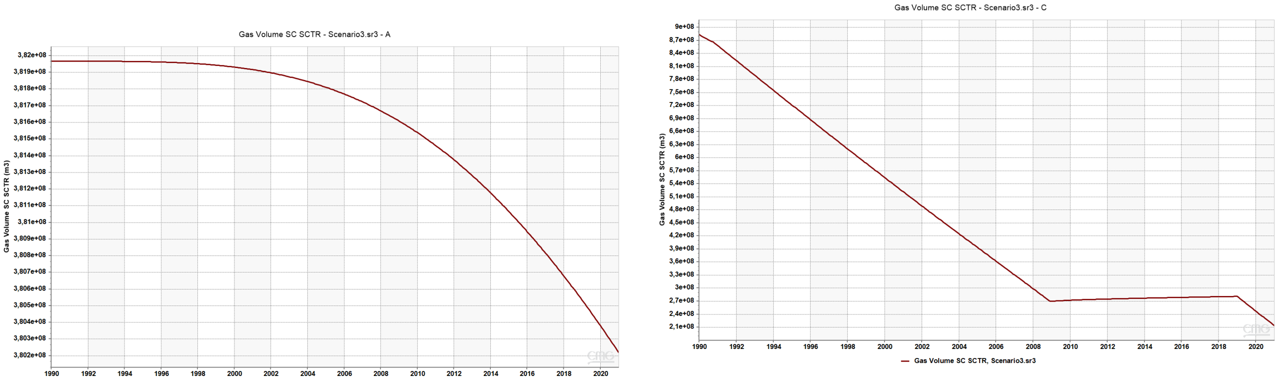

(a) Graph showing the gas volume of the A-sector (A-zone) in Scenario 3

(b) Graph showing the gas volume of the C-sector in Scenario 3. As seen, the gas volume decreases due to production and increases during shut-in period.

Figure 49: Graphs of the gas volumes of sectors A (a) and C (b) in scenario 3

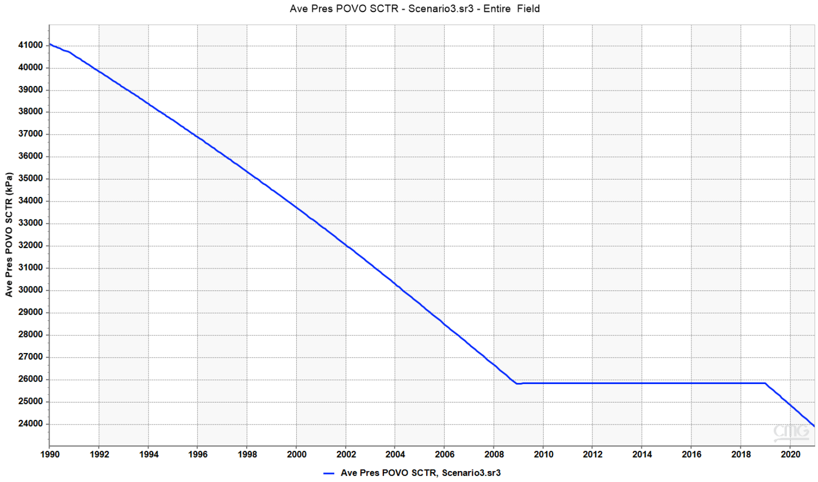

Figure 50: Graph showing the average pressure decline across the entire model for the third Scenario.

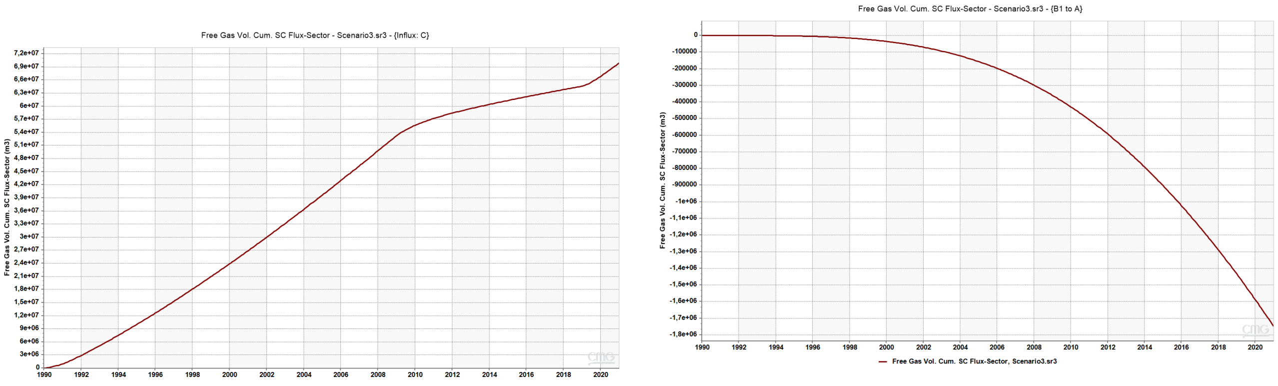

(a) Graph illustrating the cumulative gas volume that has entered the C-sector over time

(b) Graph illustrating the cumulative gas volume flux from the B1-sector into the A-sector. The negative numbers mean a flux from A to B1

Figure 51: Graphs of the total cumulative gas volume over time entering the C-sector (a) and moving from the B1-sector into the A-sector (b) in scenario 3

5.2.4 Scenario 4 Basecase

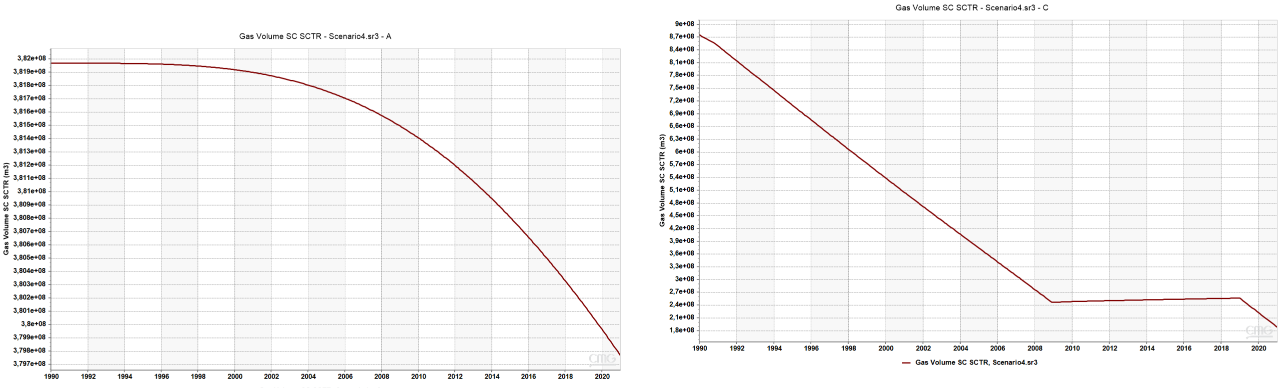

(a) Graph showing the gas volume of the A-sector (A-zone) in Scenario 4

(b) Graph showing the gas volume of the C-sector in Scenario 4. As seen, the gas volume decreases due to production and increases during shut-in period.

Figure 52: Graphs of the gas volumes of sectors A (a) and C (b) in scenario 4

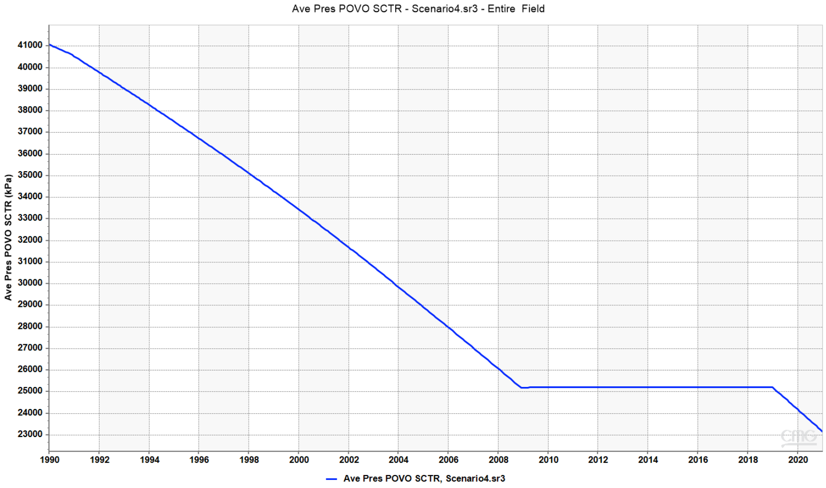

Figure 53: Graph showing the average pressure decline across the entire model for the fourth Scenario.

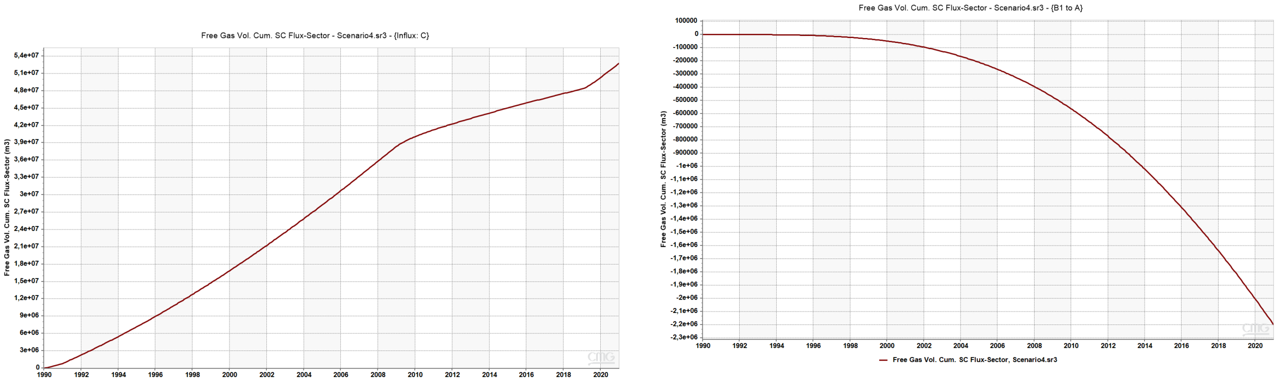

(a) Graph illustrating the cumulative gas volume that has entered the C-sector over time

(b) Graph illustrating the cumulative gas volume flux from the B1-sector into the A-sector. The negative numbers mean a flux from A to B1

Figure 54: Graphs of the total cumulative gas volume over time entering the C-sector (a) and moving from the B1-sector into the A-sector (b) in scenario 4

5.2.5 Sensitivity Analysis Manual Simulations

The results of the manual simulations for basecase Scenarios 1, 2, and 3 include graphs of total cumulative gas volume over time from sectors A to B1 and from B3 to C with water saturation = 0.96. The results can be found for scenario 1 in figure 55, scenario 2 in figure 56, and scenario 3 in figure 57. The sensitivity analysis of scenario 4 is given in chapter 5.2.6

Scenario 1

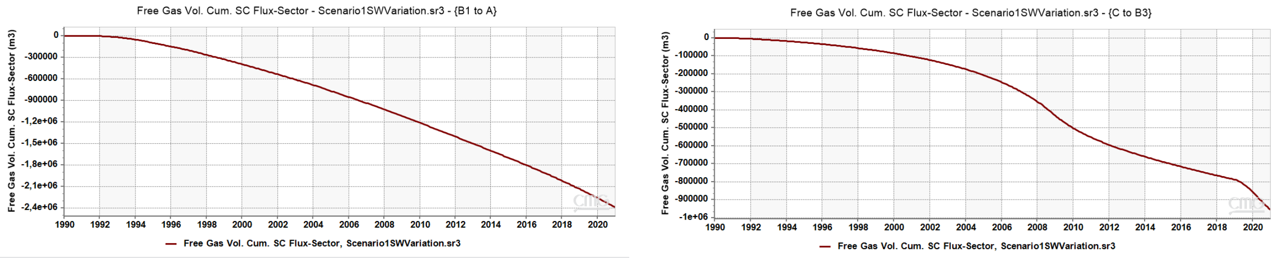

(a) Graph showing the gas cumulative flux of sector-A into sector-B1 in scenario 1 with SW=0.96 for the B zone

(b) Graph showing the gas cumulative flux of sector B3 into sector C in scenario 1 with SW=0.96 for the B zone

Figure 55: Graphs of the total cumulative gas volume over time in from sectors A into sector B1 (a) and from sector B3 into sector C (b) in basecase scenario 1

Scenario 2

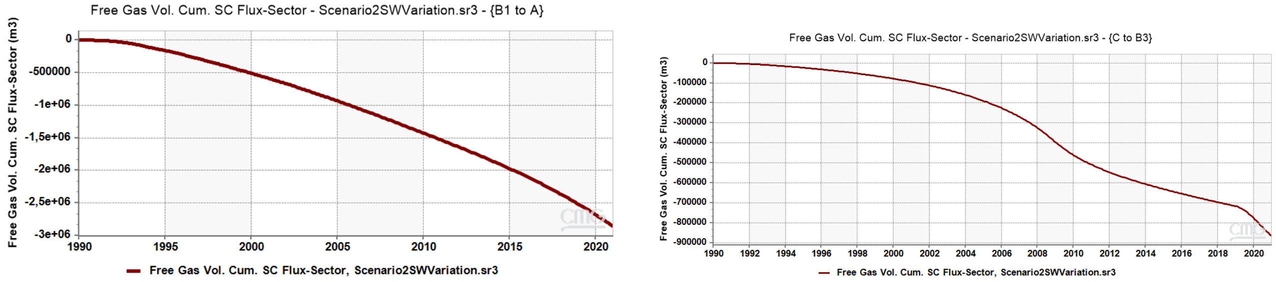

(a) Graph showing the gas cumulative flux of sector-A into sector-B1 in scenario 2 with SW=0.96 for the B zone

(b) Graph showing the gas cumulative flux of sector B3 into sector C in scenario 2 with SW=0.96 for the B-zone

Figure 56: Graphs of the total cumulative gas volume over time in from sectors A into sector B1 (a) and from sector B3 into sector C (b) in basecase scenario 2

Scenario 3

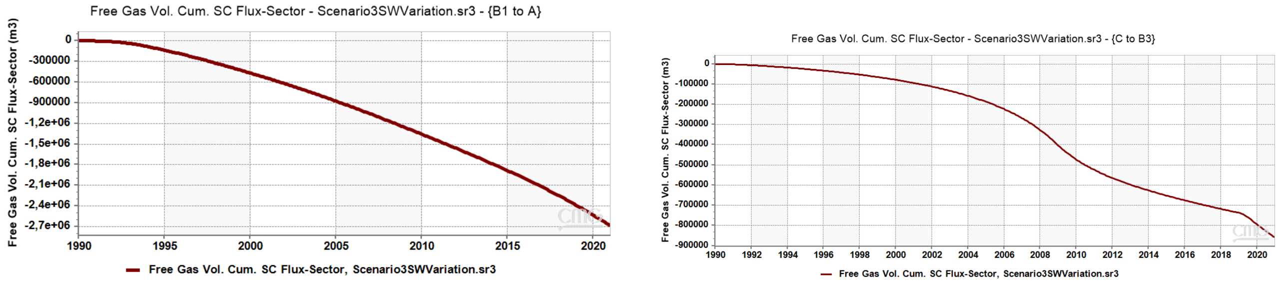

(a) Graph showing the gas cumulative gas volume from sector A into sector B1 in scenario 3 with SW=0.96 for the B- and C2-zones

(b) Graph showing the gas cumulative gas volume from sector B3 into sector C in scenario 3 with SW=0.96 for the B- and C2-zones

Figure 57: Graphs of the total cumulative gas volume over time in from sectors A into sector B1 (a) and from sector B3 into sector C (b) in basecase scenario 3

5.2.6 Extended Sensitivity Analysis Scenario 4

The results of the extended sensitivity analysis simulations for Scenario 4 include graphs of total cumulative gas volume over time from sectors A to B1 and from B3 to C for the porosity in the B-zone multiplied by 0.1 and 4, the vertical permeability in the B-zone multiplied by 0.1, 10 and 100 and the initial water saturation of 0.65 and 0.96. The results for vertical permeability analysis can be found in figures 60 to 62, for porosity analysis in figures 58 and 59, and for the initial water saturation analysis in figures 63 and 64. Additionally, to evaluate the importance of explicitly mapping reservoir architecture and geometries, the results of a simplified layer-cake model, where uniform permeability was assigned to the non-continuous layers of Scenario 4, are presented in figures 65 and 66.

Porosity

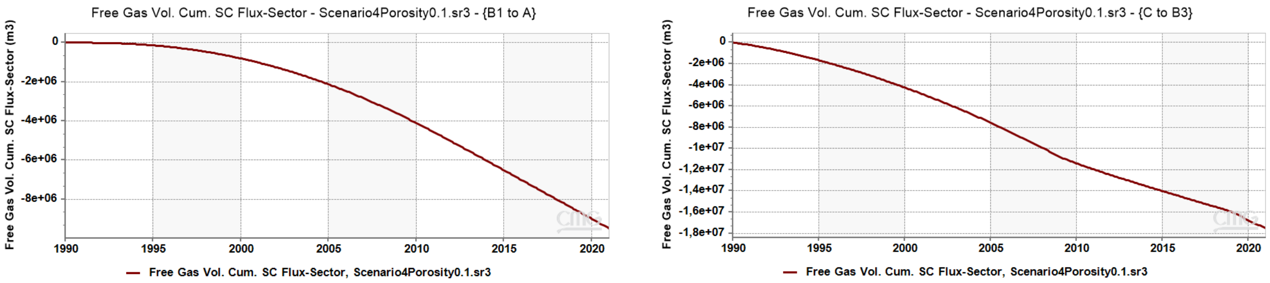

(a) Graph showing the gas cumulative gas volume from sector A into sector B1 in scenario 4 with porosity multiplied by 0.1 for the B- and C2- zones

(b) Graph showing the gas cumulative gas volume from sector B3 into sector C in scenario 4 with porosity multiplied by 0.1 for the B- and C2-zones

Figure 58: Graphs showing the gas cumulative gas volume from sector A into sector B1 (a) and from sector B3 into sector C (b) in scenario 4 with porosity multiplied by 0.1 for the B- and C2-zone

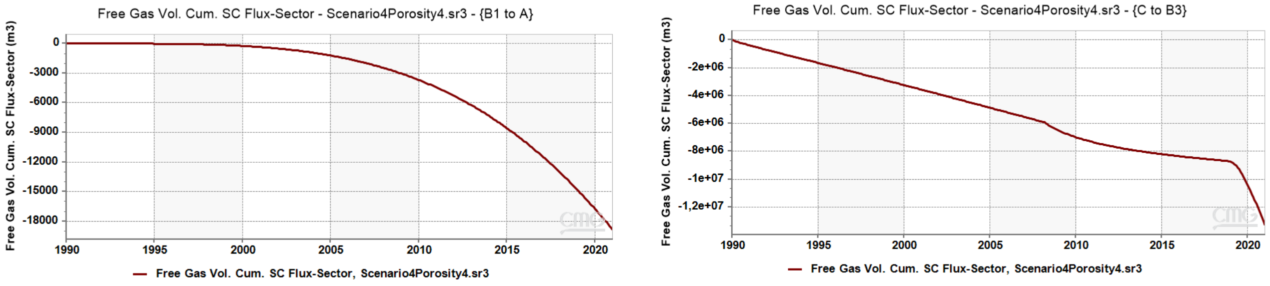

(a) Graph showing the gas cumulative gas volume from sector A into sector B1 in scenario 4 with porosity multiplied by 4 for the B- and C2- zones

(b) Graph showing the gas cumulative gas volume from sector B3 into sector C in scenario 4 with porosity multiplied by 0.1 for the B- and C2-zones

Figure 59: Graphs showing the gas cumulative gas volume from sector A into sector B1 (a) and from sector B3 into sector C (b) in scenario 4 with porosity multiplied by 4 for the B- and C2-zone

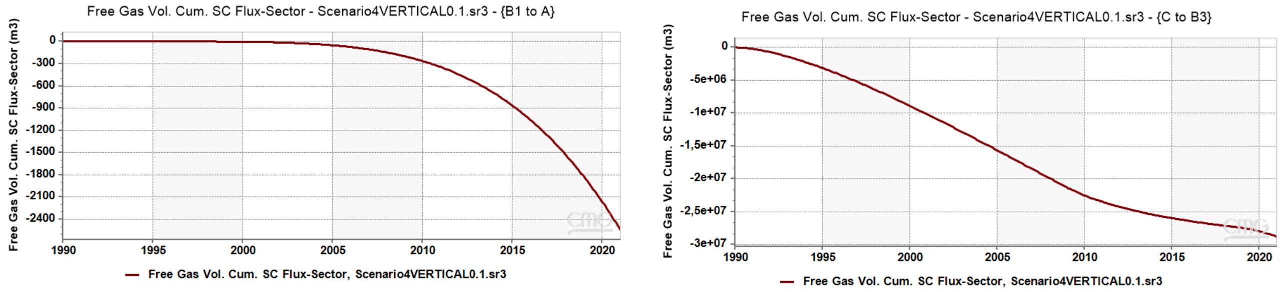

(a) Graph showing the gas cumulative gas volume from sector A into sector B1 in scenario 4 with vertical permeability multiplied by 0.1 for the B- and C2- zones

(b) Graph showing the gas cumulative gas volume from sector B3 into sector C in scenario 4 with vertical permeability multiplied by 0.1 for the B- and C2-zones

Figure 60: Graphs showing the gas cumulative gas volume from sector A into sector B1 (a) and from sector B3 into sector C (b) in scenario 4 with vertical permeability multiplied by 0.1 for the B- and C2-zone

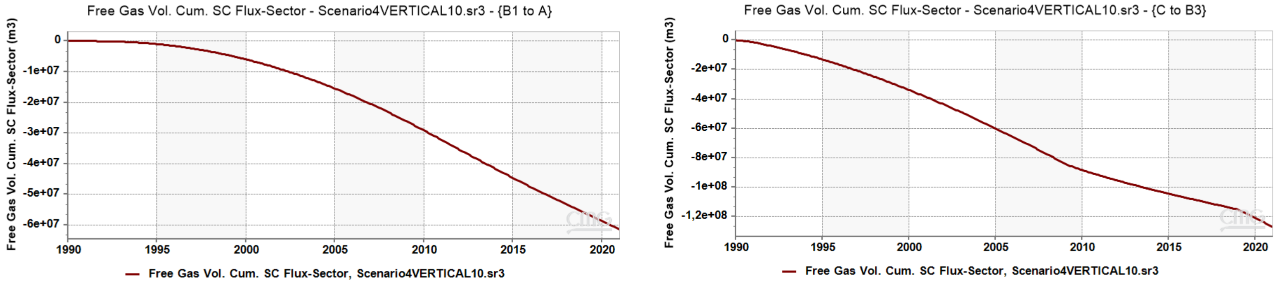

(a) Graph showing the gas cumulative gas volume from sector A into sector B1 in scenario 4 with vertical permeability multiplied by 10 for the B- and C2- zones

(b) Graph showing the gas cumulative gas volume from sector B3 into sector C in scenario 4 with vertical permeability multiplied by 10 for the B- and C2-zones

Figure 61: Graphs showing the gas cumulative gas volume from sector A into sector B1 (a) and from sector B3 into sector C (b) in scenario 4 with vertical permeability multiplied by 10 for the B- and C2-zone

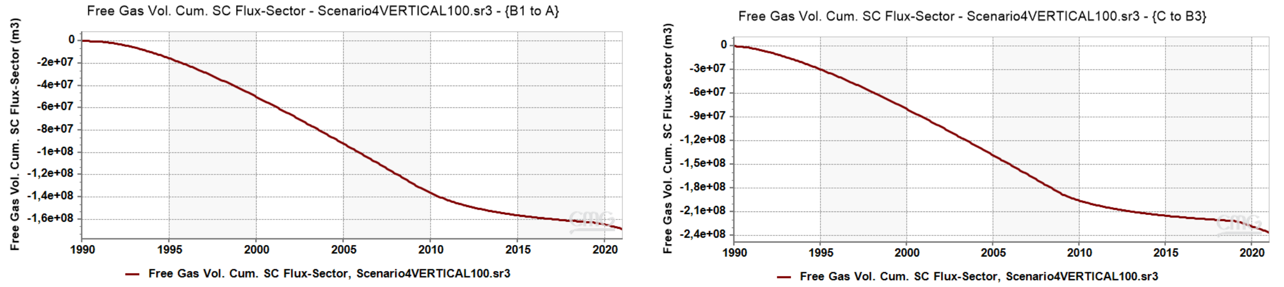

(a) Graph showing the gas cumulative gas volume from sector A into sector B1 in scenario 4 with vertical permeability multiplied by 100 for the B- and C2- zones

(b) Graph showing the gas cumulative gas volume from sector B3 into sector C in scenario 4 with vertical permeability multiplied by 100 for the B- and C2-zones

Figure 62: Graphs showing the gas cumulative gas volume from sector A into sector B1 (a) and from sector B3 into sector C (b) in scenario 4 with vertical permeability multiplied by 100 for the B- and C2-zone

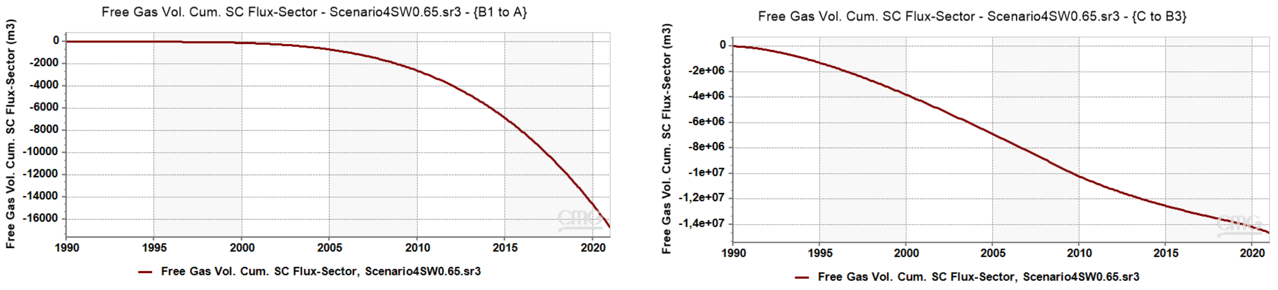

(a) Graph showing the gas cumulative gas volume from sector A into sector B1 in scenario 4 with initial water saturation set at SW=0.65 for the B- and C2- zones

(b) Graph showing the gas cumulative gas volume from sector B3 into sector C in scenario 4 with initial water saturation set at SW=0.65 for the B- and C2- zones

Figure 63: Graphs showing the gas cumulative gas volume from sector A into sector B1 (a) and from sector B3 into sector C (b) in scenario 4 with initial water saturation 0.65 for the B- and C2-zone

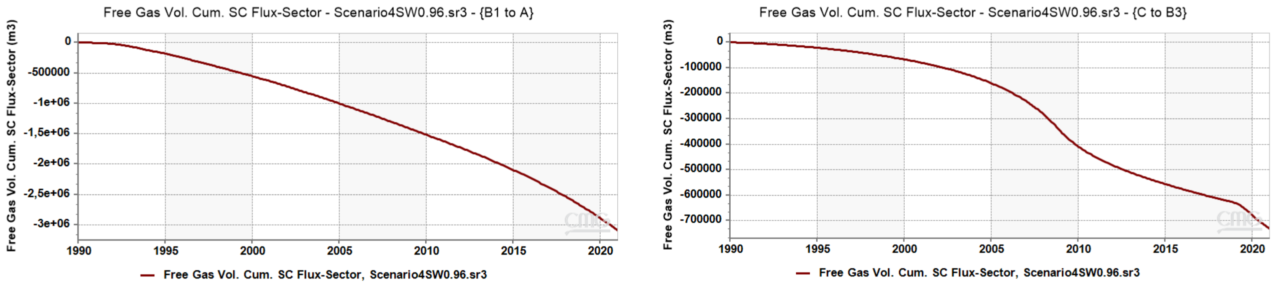

(a) Graph showing the gas cumulative gas volume from sector A into sector B1 in scenario 4 with initial water saturation set at SW=0.96 for the B- and C2- zones

(b) Graph showing the gas cumulative gas volume from sector B3 into sector C in scenario 4 with initial water saturation set at SW=0.96 for the B- and C2- zones

Figure 64: Graphs showing the gas cumulative gas volume from sector A into sector B1 (a) and from sector B3 into sector C (b) in scenario 4 with initial water saturation 0.96 for the B- and C2-zone

Average Permeability

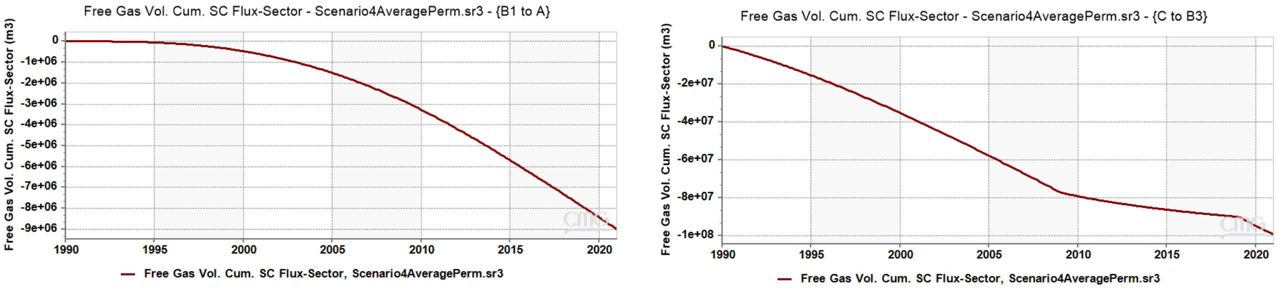

(a) Graph showing the gas cumulative gas volume from sector A into sector B1 in scenario 4 with uniform vertical and horizontal permeability for non-continuous layers

(b) Graph showing the gas cumulative gas volume from sector B3 into sector C in scenario 4 with uniform vertical and horizontal permeability for non-continuous layers

Figure 65: Graphs showing the gas cumulative gas volume from sector A into sector B1 (a) and from sector B3 into sector C (b) in scenario 4 with uniform vertical and horizontal permeability for non-continuous layers

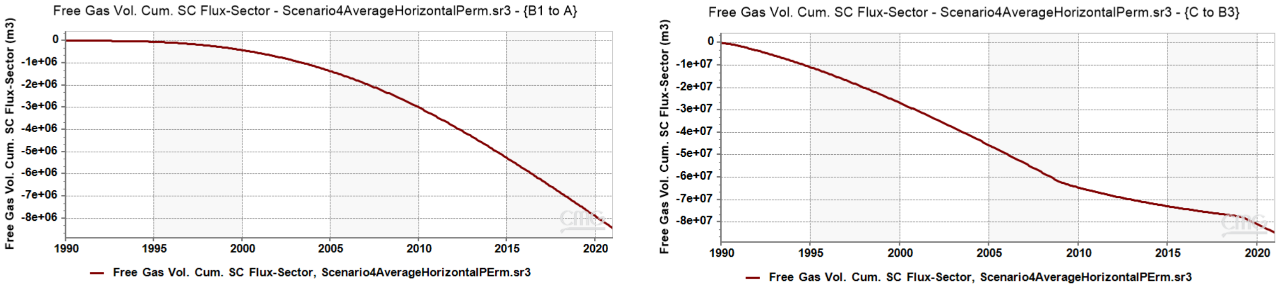

(a) Graph showing the gas cumulative gas volume from sector A into sector B1 in scenario 4 with uniform horizontal permeability for non-continuous layers

(b) Graph showing the gas cumulative gas volume from sector B3 into sector C in scenario 4 with uniform horizontal permeability for non-continuous layers

Figure 66: Graphs showing the gas cumulative gas volume from sector A into sector B1 (a) and from sector B3 into sector C (b) in scenario 4 with uniform horizontal permeability for non-continuous layers

5.2.7 Sensitivity Analysis Capillary Pressure and Residual Gas Saturation

In this section, the results of the simulations with keyword SWINIT-ADJMOB ON, which means that the calculated capillary pressures are used during the simulations, are given. Besides these results, the results of increased residual water saturation are also given for scenario 4. The results in both cases, for normal capillary pressures and residual gas saturation, include graphs of total cumulative gas volume over time from sectors A to B1 and from B3 to C. The results can be found for scenario 1 in figures 67 and 68, for scenario 2 in figures 69 and 70, for scenario 3 in figures 71 to 72 and for scenario 4 in figures 73 to 75

Scenario 1

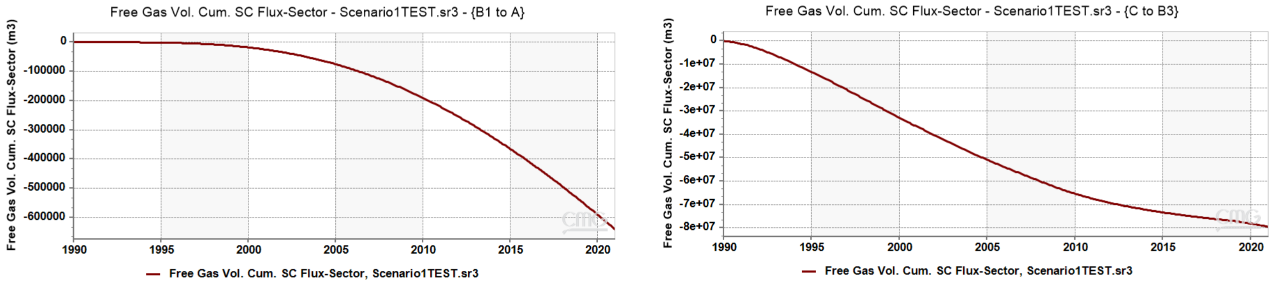

(a) Graph showing the gas cumulative gas volume from sector-A into sector-B1 in scenario 1 with normal capillary pressures

(b) Graph showing the gas cumulative gas volume from sector-B3 into sector-C in scenario 1 with normal capillary pressures

Figure 67: Graphs of the total cumulative gas volume over time in from sectors A into sector B1 (a) and from sector B3 into sector C (b) in scenario 1 with normal capillary pressure

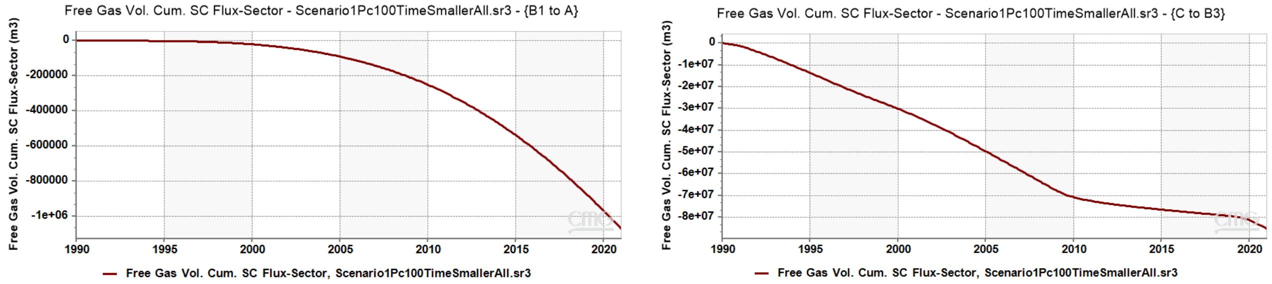

(a) Graph showing the gas cumulative gas volume from sector-A into sector-B1 in scenario 1 with capillary pressures multiplied by 0.01

(b) Graph showing the gas cumulative gas volume from sector-B3 into sector-C in scenario 1 with capillary pressures multiplied by 0.01

Figure 68: Graphs of the total cumulative gas volume over time in from sectors A into sector B1 (a) and from sector B3 into sector C (b) in scenario 1 with capillary pressure multiplied by 0.01

Scenario 2

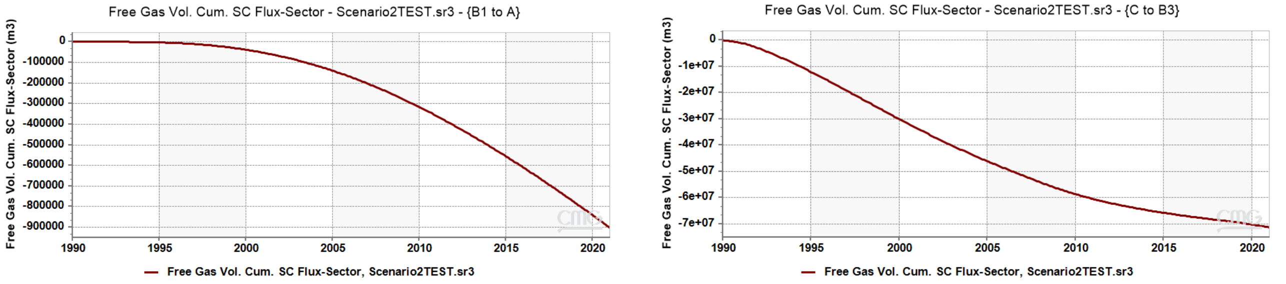

(a) Graph showing the gas cumulative gas volume from sector-A into sector-B1 in scenario 2 with normal capillary pressures

(b) Graph showing the gas cumulative gas volume from sector-B3 into sector-C in scenario 2 with normal capillary pressures

Figure 69: Graphs of the total cumulative gas volume over time in from sectors A into sector B1 (a) and from sector B3 into sector C (b) in scenario 2 with normal capillary pressure

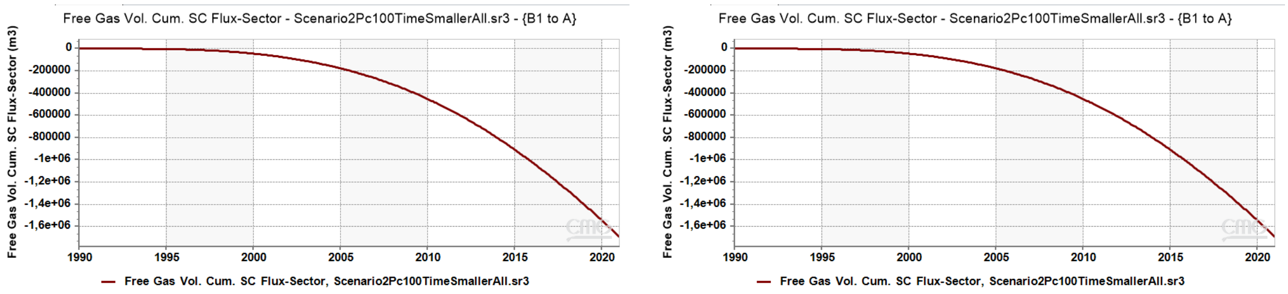

(a) Graph showing the gas cumulative gas volume from sector-A into sector-B1 in scenario 2 with capillary pressures multiplied by 0.01

(b) Graph showing the gas cumulative gas volume from sector-B3 into sector-C in scenario 2 with capillary pressures multiplied by 0.01

Figure 70: Graphs of the total cumulative gas volume over time in from sectors A into sector B1 (a) and from sector B3 into sector C (b) in scenario 2 with capillary pressure multiplied by 0.01

Scenario 3

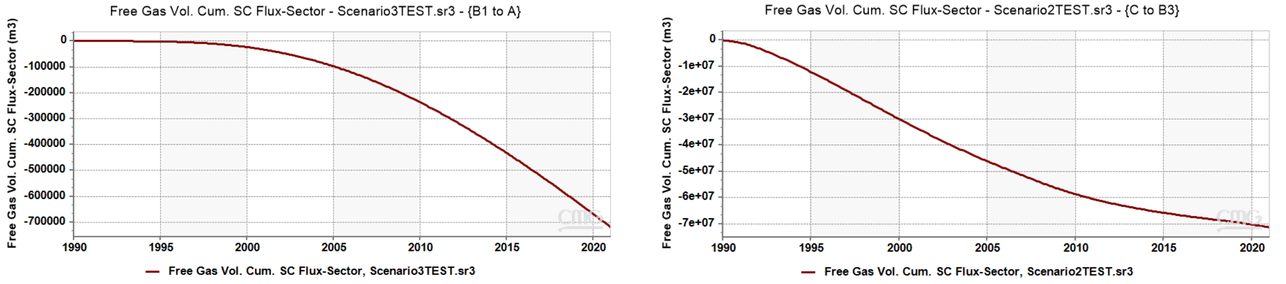

(a) Graph showing the gas cumulative gas volume from sector-A into sector-B1 in scenario 3 with normal capillary pressures

(b) Graph showing the gas cumulative gas volume from sector-B3 into sector-C in scenario 3 with normal capillary pressures

Figure 71: Graphs of the total cumulative gas volume over time in from sectors A into sector B1 (a) and from sector B3 into sector C (b) in scenario 3 with normal capillary pressure

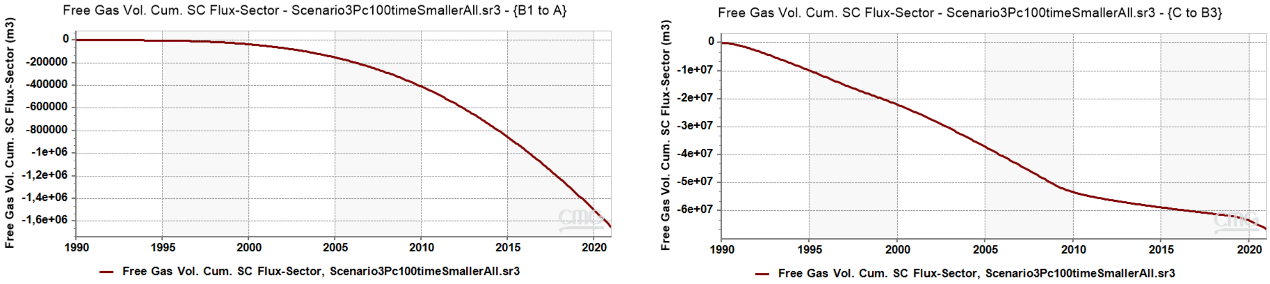

(a) Graph showing the gas cumulative gas volume from sector-A into sector-B1 in scenario 3 with capillary pressures multiplied by 0.01

(b) Graph showing the gas cumulative gas volume from sector-B3 into sector-C in scenario 3 with capillary pressures multiplied by 0.01

Figure 72: Graphs of the total cumulative gas volume over time in from sectors A into sector B1 (a) and from sector B3 into sector C (b) in scenario 3 with capillary pressure multiplied by 0.01

Scenario 4

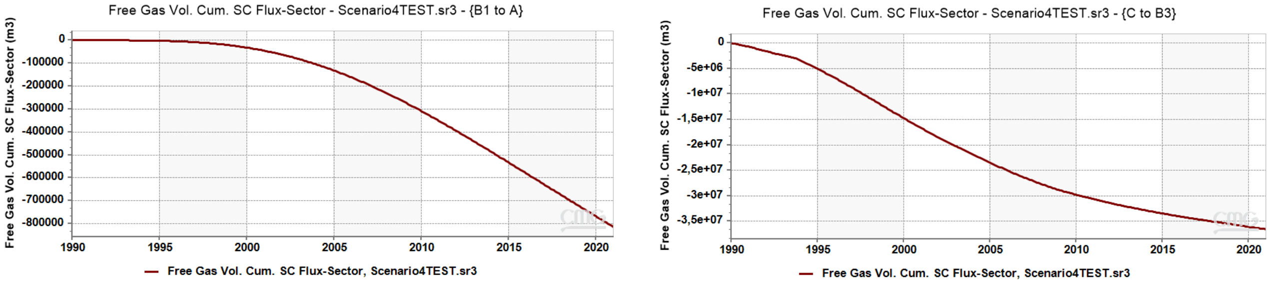

(a) Graph showing the gas cumulative gas volume from sector-A into sector-B1 in scenario 4 with normal capillary pressures

(b) Graph showing the gas cumulative gas volume from sector-B3 into sector-C in scenario 4 with normal capillary pressures

Figure 73: Graphs of the total cumulative gas volume over time in from sectors A into sector B1 (a) and from sector B3 into sector C (b) in scenario 4 with normal capillary pressure

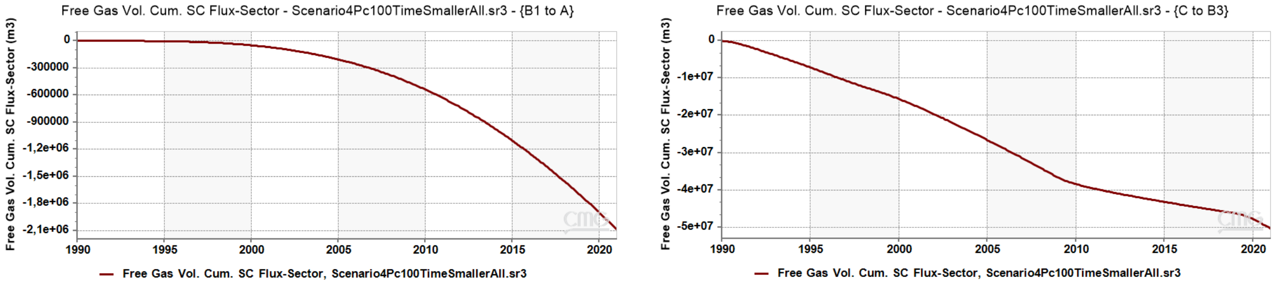

(a) Graph showing the gas cumulative gas volume from sector-A into sector-B1 in scenario 4 with capillary pressures multiplied by 0.01

(b) Graph showing the gas cumulative gas volume from sector-B3 into sector-C in scenario 4 with capillary pressures multiplied by 0.01

Figure 74: Graphs of the total cumulative gas volume over time in from sectors A into sector B1 (a) and from sector B3 into sector C (b) in scenario 4 with capillary pressure multiplied by 0.01

****

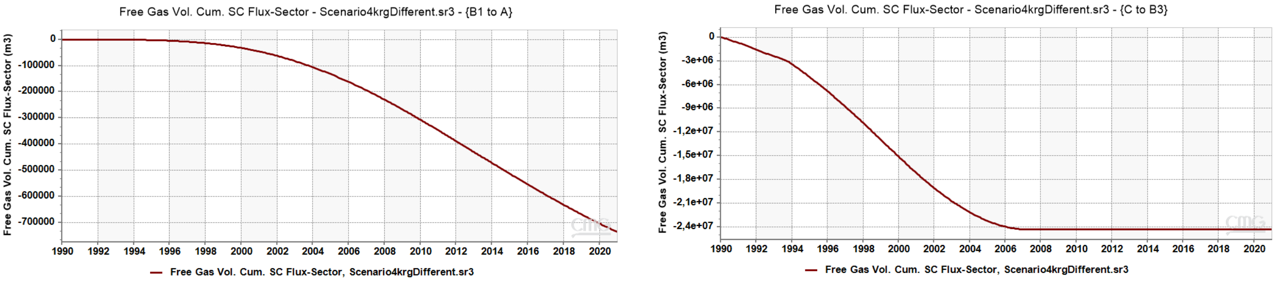

(a) Graph showing the gas cumulative gas volume from sector-A into sector-B1 in scenario 4 with increased Sgr

(b) Graph showing the gas cumulative gas volume from sector-B3 into sector-C in scenario 4 with increased Sgr

Figure 75: Graphs of the total cumulative gas volume over time in from sectors A into sector B1 (a) and from sector B3 into sector C (b) in scenario 4 with increased Sgr

6 Discussion

The objective of this study is to evaluate whether stratigraphic connectivity within the Upper Slochteren Member could explain recharge behavior of the C1 zone by the A zone through the B zone and what parameters enhance and influence vertical stratigraphical cross flow. To address this, four conceptual reservoir models were constructed in Rapid Reservoir Modelling (RRM), each representing a different degree of vertical connectivity within the B zone. These were subsequently simulated with CMG IMEX to analyze dynamic flow behavior under uniform production conditions. The results reveal complex and (non-)linear vertical flux patterns between the reservoir zones that appear to be strongly influenced by both stratigraphical setting and pressure redistribution. This discussion is structured in three parts. The first section evaluates the simulation results from the four architectural scenarios and interpret the resulting pressure redistribution during the simulation period and flow behavior between the A, B, and C zones. Particular attention is paid to how vertical connectivity influences recharge into the C zone, and the unexpected trend in gas flux from A to B. It also reflects on model assumptions and simplifications to assess the robustness of the findings. The second section focuses on the sensitivity analysis, in which key reservoir parameters such as vertical permeability , porosity, capillary pressure, and initial water saturation are varied to determine their individual influence on stratigraphic cross flow. The third and final section integrates insights from both the scenario analysis and sensitivity study to synthesize broader conclusions.

6.1 Pressure Distribution Basecase Simulations

The results from the four architectural scenarios demonstrate that the degree of vertical connectivity within the B zone significantly influences pressure distribution and gas migration in the near-wellbore area. Each scenario was constructed in RRM and all scenarios were based on the same conceptual base model, but differ in the amount of vertical connectivity points(by crevasse splays and channels) and amount of architectural elements present in the discontinuous layers of the B zone. Scenario 1 includes three such vertical connectivity points, scenario 2 has two, scenario 3 only one, and scenario 4 has no vertical connectivity at all. These architectural variations are confined to parts of the B and C2 zones; all other zones, particularly the A, C1, C3 zones and parts of the B and C2 zones, remained constant in geometry and reservoir properties across all simulations (figure 20). The differences in flow behavior and pressure redistribution that occur with this setup can therefore be fully attributed to architectural differences within the B zone. Despite the shared initial conditions across the four scenarios, the final average pressure distribution diverged significantly. Although initial average pressure was equal in all cases, the pressure at the end of the simulation period was highest in scenario 1 and lowest in scenario 4, following a clear trend: scenario $1 > 2 > 3 > 4$ (figures 42, 44, 47, 50 and 53in Results 5.2). This means that scenario 4 experienced the largest pressure drop across the model, while scenario 1 saw the least.

Although at first sight this observation may seem counterintuitive, given that the producing zones (C1 and C3) have the same properties in each model, closer analysis reveals a physically consistent explanation. The pressure differences for the scenarios can be explained by the degree of pressure support coming from below. In the more connected scenarios, vertical flow from deeper zones (the B zone) toward the producing intervals (C-sector) is facilitated by higher permeability pathways through the connected architectural elements ([Zhao et al., 2025, Fuquan et al., 2019]). This allows easier redistribution of pressure from underlying units to the C-sector. In contrast, in the less connected scenarios (lower permeability), gas migration from deeper zones is constrained due to lack of permeable vertical pathways. This restricted mobility leads to sharper pressure declines over time and distance ([Zhao et al., 2025]). This behavior is consistent with observations from low-permeability reservoirs, where gas moves more slowly, and pressure tends to drop more significantly with distance from the wellbore ([Zhao et al., 2025, Fuquan et al., 2019]). Thus, the permeability is inversely to the average pressure drop across the model; the higher the (average) permeability (scenario $1>2>3>4$) the lower the pressure drop (Scenario $4>3>2>1$). Higher pressure differences between parts of the reservoir allow capillary pressures to be more readily overcome, enabling gas to displace water and flow through the pore network. Once the capillary pressure is overwon and flow is enabled, the pressure gradients is a key parameter determining gas velocity as per Darcy's Law ([Johns, 2004]). Throughout this thesis, when pressure difference is cited as a driver of gas flow, it is implicitly understood that the pressure difference has already exceeded the capillary entry pressure, enabling gas movement and determining flow rate according to Darcy's Law. Additionally, when rock are over gas-saturated, capillary pressure is not needed to be overcame since the pores are already filled with gas, enabling gas movement. Moreover, the same pressure difference subsequently governs the gas flow rate according to Darcy's Law, where higher pressure differences result in higher gas velocities and fluxes ([Johns, 2004]). Additionally, throughout this chapter, whenever gas fluxes or fluxes are mentioned between certain sectors (for example, gas flux from A to B3), this refers specifically to the volume of gas flowing from one sector to another.

6.2 Flux Analysis Basecase Simulations

These pressure differences together with permeability have a clear impact on gas fluxes between zones, which was examined in detail by monitoring gas volumes moving between sector boundaries. The gas volumes movements are monitored between each defined sectors: B3 to C, B2 to B3, B1 to B2 and A to B1. The gas influx from the B3 sector into the C zone shows a particularly clear trend based on the properties (permeability and porosity). The magnitude of the fluxes decreases systematically with reduced vertical connectivity; scenario 1 $>$ 2 $>$ 3 $>$ 4 (figure 76).

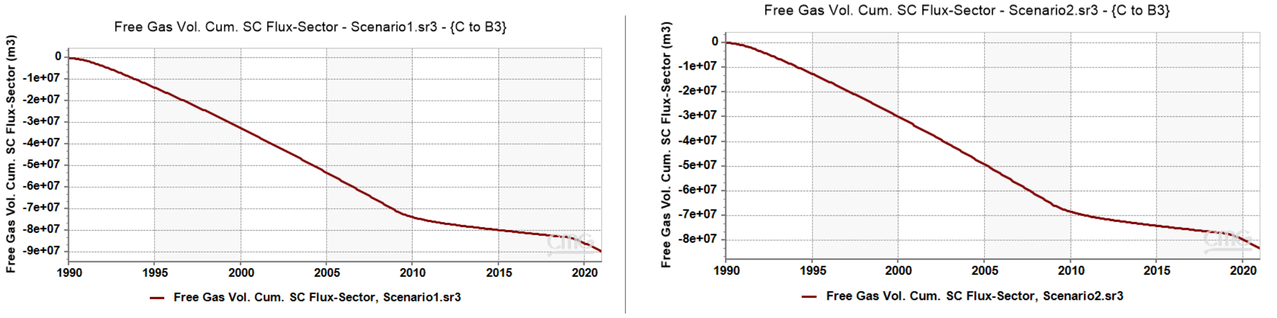

(a) Graph illustrating the cumulative gas volume moving from the B3-sector into the C-sector in scenario 1

(b) Graph illustrating the cumulative gas volume moving from the B3-sector into the C-sector in scenario 2

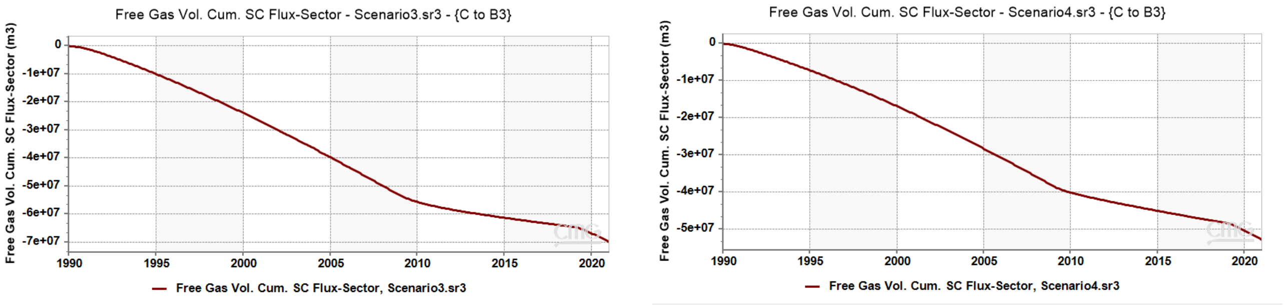

(c) Graph illustrating the cumulative gas volume moving from the B3-sector into the C-sector in scenario 3

(d) Graph illustrating the cumulative gas volume moving from the B3-sector into the C-sector in scenario 4

Figure 76: Graphs of the total cumulative gas volume over time from sector B3 into sector C in scenarios 1 (a), 2 (b), 3(c), and 4 (d)

Scenario 1, with the highest number of connected elements and highest effective permeability in the B3-sector, exhibits the greatest gas influx into the C-zone. Scenarios 2 and 3 follow this with decreasing gas influx respectively, and scenario 4 shows the lowest gas influx. This behavior is well explained by Darcy's Law, where the volumetric flow rate q is directly proportional to the permeability K, provided that viscosity μ remain constant, and pressure gradient ΔP: q=-KA/μ * ΔP/dx)[Johns, 2004]). The pressure decrease in the B3-sector follows the previously described trend of scenario 4 $>$ 3$>$ 2$>$ 1 (figure 77), but since B3 consist mainly of non-continuous layers, and permeability in this sector varies between scenarios depending on how many vertical connections were modeled and therefore average permeability of the layer, this result is expected based on the fact that pressure drop increases with decreasing permeability ([Fuquan et al., 2019, Zhao et al., 2025]). Although some variation in pressure gradient exists between the scenarios in the B3-sector, it is the difference in permeability, particularly vertical permeability across the B3-sector, that drives this trend. Channels and crevasses in the B3-sector provide high-permeability pathways that enable upward migration of gas into the C zone. In scenario 4, these features are absent, reducing the effective permeability and, consequently, the volumetric flux. The pressure differences are not large enough yet to heavily influence gas flow from sector B3 to C.

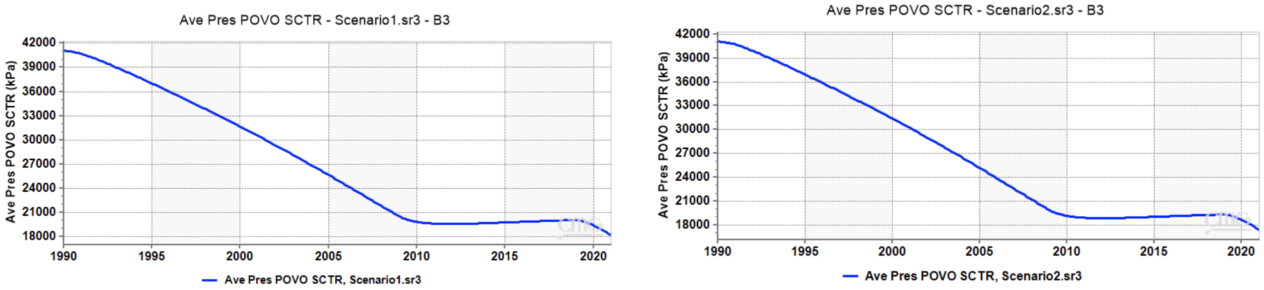

(a) Graph illustrating the average pressure over time of sector B3 in scenario 1

(b) Graph illustrating the average pressure over time of sector B3 in scenario 2

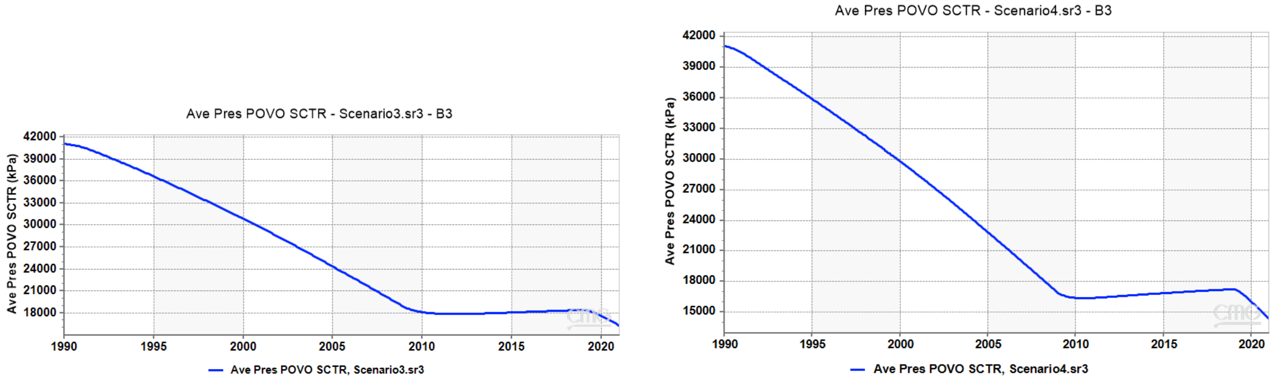

(c) Graph illustrating the average pressure over time of sector B3 in scenario 3

(d) Graph illustrating the average pressure over time of sector B3 in scenario 4

Figure 77: Graphs of the average pressure over time of sector B3 in scenarios 1 (a), 2 (b), 3(c), and 4 (d)

Fluxes from B2 to B3 reveal a more complex and less predictable trend. The observed net gas volume flux follows the order: scenario 4 > 3 > 1 > 2 (figures 80). Unlike B3, the B2-sector spans a wider portion of the B-zone and includes a greater proportion of continuous layers, interpreted as mud-rich units with low vertical permeability values of approximately 0.0001 mD. Therefore, the flow behavior cannot be explained purely based on permeability only, since B2 contains both discontinuous and a larger number of continuous layers. This drastically limits vertical flow, since the permeability in the continuous layers in the B-zone is low. Even in scenarios where overlying connectivity exists, the internal structure of the B2-sector poses a significant restriction on upward gas movement. The low permeability of these continuous units is a dominant control on flow from B2 to B3. In this case, Darcy's Law still applies, but the relative influence of pressure gradients becomes more apparent. The top layer of B2 consist of a continuous layer, governing the flow from the top of sector B2 into sector B3. Even though scenarios 1 and 2 benefit from high permeability in the non-continuous layers and higher average permeability in the B2-sector, the pressure gradient is not large enough to initiate faster flow in the continuous layers. In contrast, scenarios 3 and 4, although lower in permeability in the non-continuous layers, have higher pressure gradients between the top of sector B2 and bottom of sector B3, which enhances their respective gas flux in the continuous layers (figures 81). Notably, scenario 2, despite having moderately good permeability in non-continuous layers, exhibits the lowest flux between these sectors. Since the top of the B2-sector consist of a continuous layer and thus even permeability in all scenarios, the flow is mostly governed by the pressure gradient. Since the average pressure in these sectors follows the trend scenario 4 > 3 > 2 > 1, the gas flux follows almost the same trend per Darcy Law [Johns, 2004]. However, the flux trend does not follow the exact trend of the average pressure. This can be explained by the fact that in some places at the boundary between the B2- and B3-sectors, the pressure gradient of scenario 1 is higher than in scenario 2 resulting in higher fluxes in scenario 1 (78. In these figures there can be observed that the pressure difference in scenario 1 is 853 kPa between the top and bottom of the B3- and B2-sectors, and 837 kPa in scenario 2.

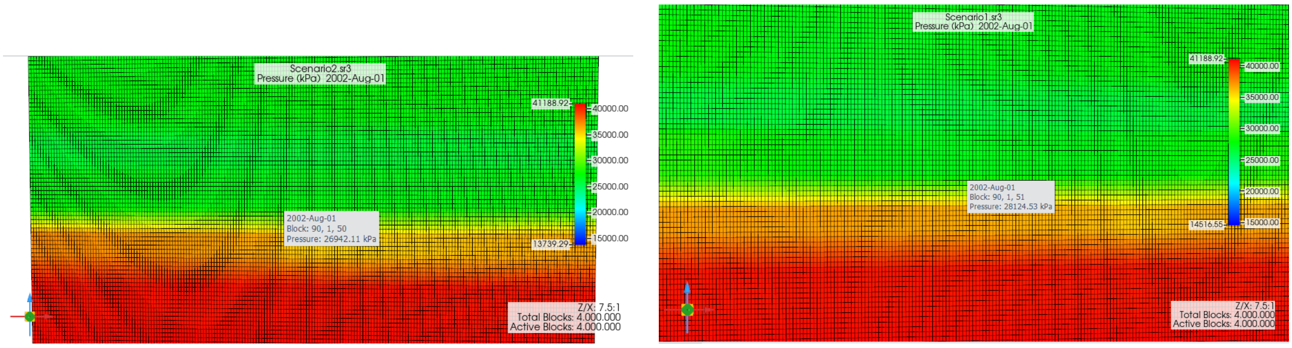

(a) Screenshot showing the pressure at block 90, 1, 50 in scenario 1

(b) Screenshot showing the pressure at block 90, 1, 51 in scenario 1

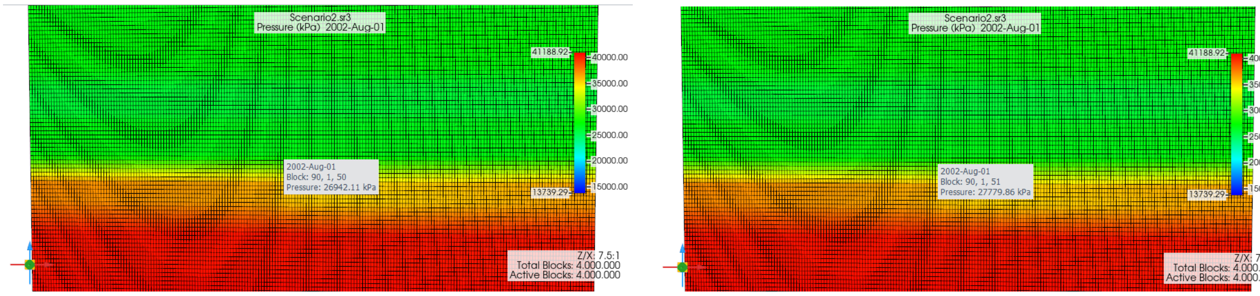

(c) Screenshot showing the pressure at block 90, 1, 50 in scenario 2

(d) Screenshot showing the pressure at block 90, 1, 51 in scenario 2

Figure 78: Screenshots showing the local pressure differences between the B2 (block 90, 1, 51) and B3 sector (block 90, 1, 50) in scenario 1 (a and b) and scenario 2 (c and d)

In another location, the pressure gradient in scenario 2 is higher than in scenario 1 (79. Where the differences for scenario 1 and 2 are 770 kPa and 807 kPa respectively. This phenomenon is explained by the distribution of architectural elements. In some areas, a higher amount of architectural elements is present in scenario 1 or 2 over horizontal/vertical distance, leading to less sharp pressure declines over distance. In the case where less architectural elements are present, a sharper pressure decline is observed, leading to higher local pressure gradients. In case of scenario 1, the architectural elements are less distributed over the non-continuous layer, having more areas with local lower permeability. These lower permeability zones experience sharper pressure drops over distance. Thus even though, the average permeability of the B2- and B3-sectors in scenario 1 is higher than the average permeability in scenario 2 and the average pressure in scenario 1 is higher than in scenario 2 (less sharp pressure decline due to higher permeability), still higher fluxes can be observed induced by local higher pressure gradients in scenario 1. Apparently, the architectural elements in scenario 1 are more located near each other in comparison with the architectural elements of scenario 2, leading to local higher pressure gradients in scenario 1, resulting in a higher total flux. The distribution of architectural elements in both scenarios in the B2- and B3-sectors can also be observed in figures 30 to 35, which reinforce the idea that the architectural elements are less distributed in scenario 1 than in scenario 2 in some locations, creating higher local pressure gradients.

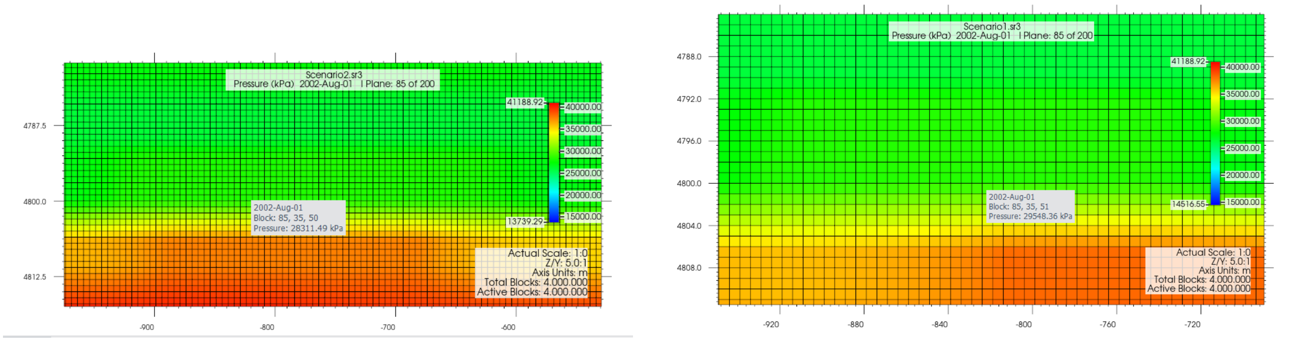

(a) Screenshot showing the pressure at block 85, 35, 50 in scenario 1

(b) Screenshot showing the pressure at block 85, 35, 51 in scenario 1

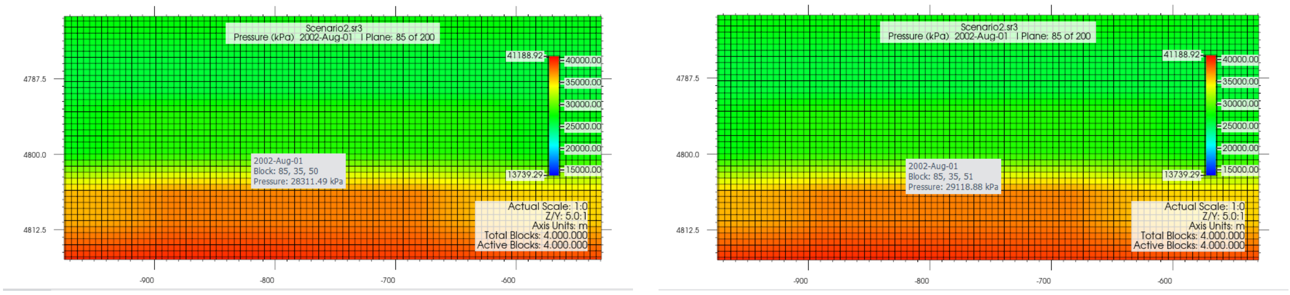

(c) Screenshot showing the pressure at block 85, 35, 50 in scenario 2

(d) Screenshot showing the pressure at block 85, 35, 51 in scenario 2

Figure 79: Screenshots showing the local pressure differences between the B2- (block 85, 35, 51) and B3-sectors (block 85, 35, 50) in scenario 1 (a and b) and scenario 2 (c and d)

This interplay suggests that the relative dominance of average permeability or pressure gradient can shift depending on which part, continuous or non-continuous layers, of the model is considered and depending on the connectivity of surrounding layers. It is likely that the B2-sector is a great example of the alternation of influences of both pressure gradients and permeability providing valuable information on both parameters.

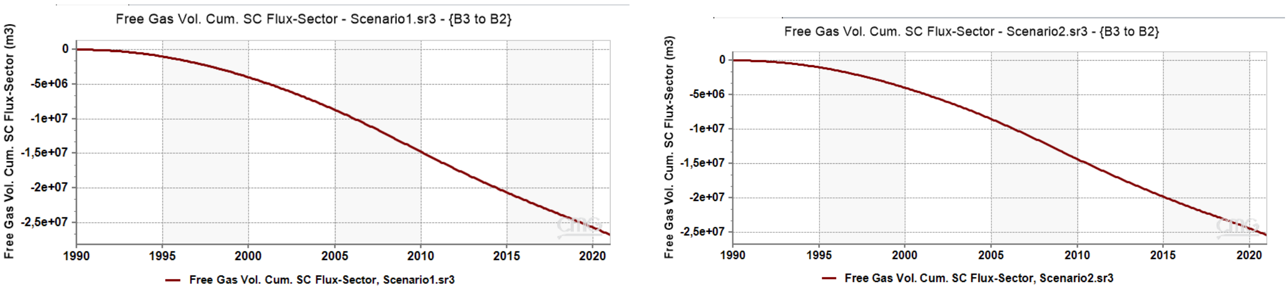

(a) Graph illustrating the cumulative gas volume moving from the B2-sector into the B3-sector in scenario 1

(b) Graph illustrating the cumulative gas volume moving from the B2-sector into the B3-sector in scenario 2

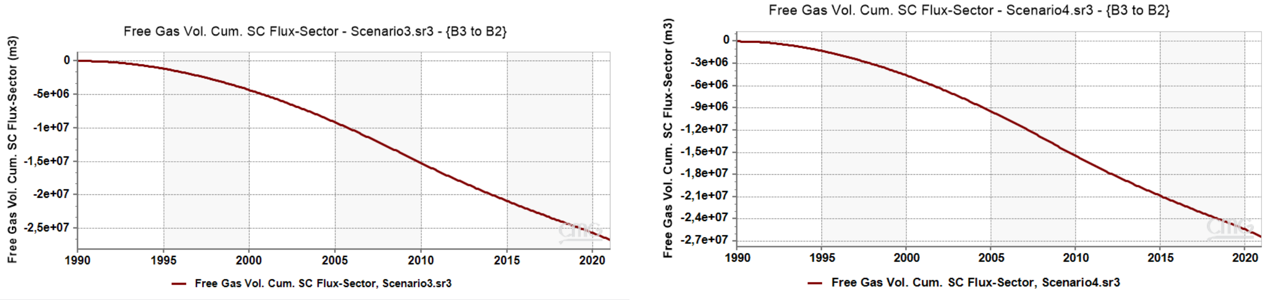

(c) Graph illustrating the cumulative gas volume moving from the B2-sector into the B3-sector in scenario 3

(d) Graph illustrating the cumulative gas volume moving from the B2-sector into the B3-sector in scenario 4

Figure 80: Graphs of the total cumulative gas volume over time from sector B2 into sector B3 in scenarios 1 (a), 2 (b), 3(c), and 4 (d)

The magnitude of the effect of pressure gradient and permeability on Darcy's Law is further supported by the large difference in net gas flux from the B3- to the C-sector and from the B2- to the B3-sector. While the B3 to C fluxes differ by over 3.7× 10^7 m^3 for scenario 1 and 4, the B2- to B3-sector flux difference is approximately 0.04× 10^7 m^3 for scenario 1 and 4. Scenario 2 seem to have the least gas flux because the combination of permeability and pressure difference has the lowest impact, resulting in slower gas movement and therefore lower fluxes. This reduction suggests that while permeability clearly dominates the B3- to C-sector interface, pressure gradient becomes increasingly important deeper in the model, particularly when the volume of continuous layers increase in a sector. This balance between permeability and pressure gradient as competing drivers of gas flow in stratified reservoirs echoes observations made in low-permeability field studies, where pressure-induced redistribution becomes a dominant recovery mechanism ([Zhao et al., 2025]).

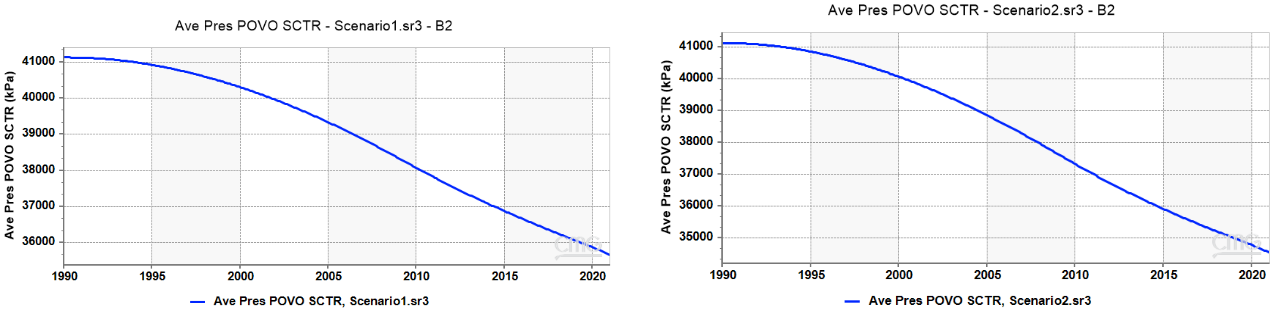

(a) Graph illustrating the average pressure over time of sector B2 in scenario 1

(b) Graph illustrating the average pressure over time of sector B2 in scenario 2

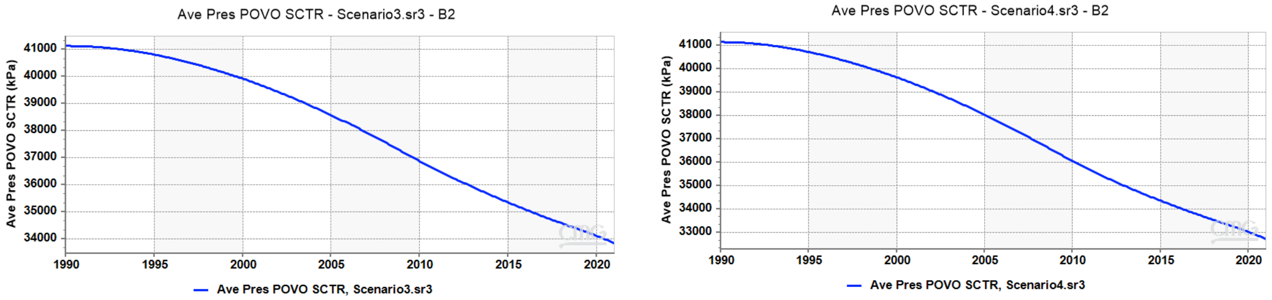

(c) Graph illustrating the average pressure over time of sector B2 in scenario 3

(d) Graph illustrating the average pressure over time of sector B2 in scenario 4

Figure 81: Graphs of the average pressure over time of sector B2 in scenarios 1 (a), 2 (b), 3(c), and 4 (d)

The fluxes from the B1 to B2 sectors follow yet another trend. In this case, scenario 4 exhibits the highest gas flux, followed by scenarios 2, 3, and 1 (figures 82). Unlike the B3 sector, where permeability varies per scenario, the B1 sector is composed entirely of continuous layers with uniform reservoir properties. This means the k/μ term in Darcy's Law is held constant across all scenarios, and any variation in flow must stem from the pressure gradient. Since the B2 sector experiences progressively sharper pressure drops in the lower-connectivity scenarios, it creates stronger pressure gradients across the B1–B2 interface.

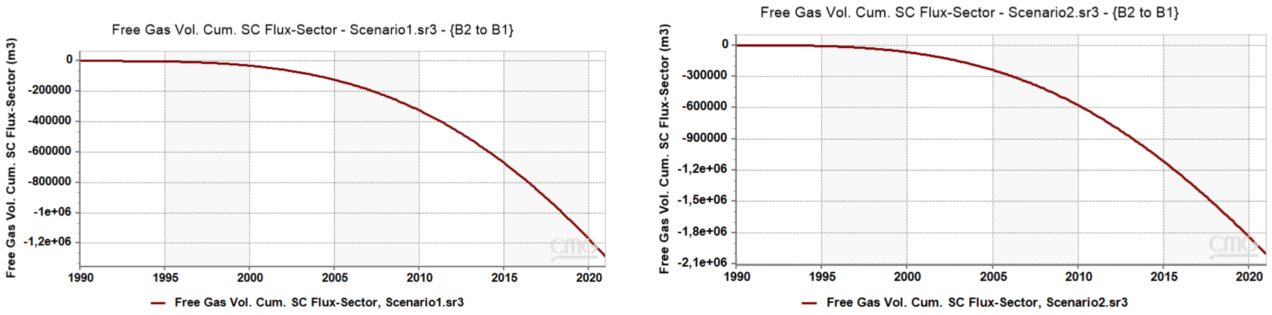

(a) Graph illustrating the cumulative gas volume moving from the B1-sector into the B2-sector in scenario 1

(b) Graph illustrating the cumulative gas volume moving from the B1-sector into the B2-sector in scenario 2

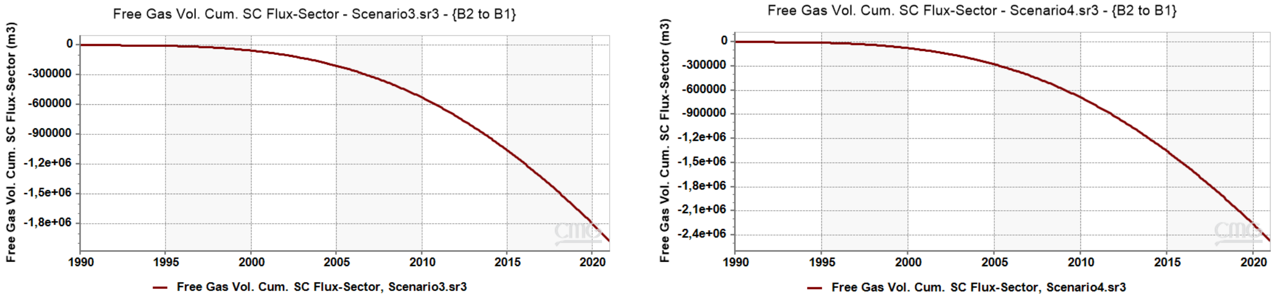

(c) Graph illustrating the cumulative gas volume moving from the B1-sector into the B2-sector in scenario 3

(d) Graph illustrating the cumulative gas volume moving from the B1-sector into the B2-sector in scenario 4

Figure 82: Graphs of total cumulative gas volume over time from sector B1 into sector B2 in scenarios 1 (a), 2 (b), 3(c), and 4 (d)

Scenario 2 exhibits higher gas flux into the B2-sector than scenario 3 which would not be expected based on average pressures in the B2-sector. The average pressure for scenario 2 is at the end of the simulation 34560 kPa in the B2-sector and 39000 kPa in the B1-sector, while scenario 3 shows average pressures of 33860 kPa in the B2-sector and 38950 kPa in B1-sector. The pressure difference of scenario 3 between the average pressures of the B1- and B2-sectors is therefore higher than the pressure difference of scenario 2 between the B1- and B2-sectors (figure 83.

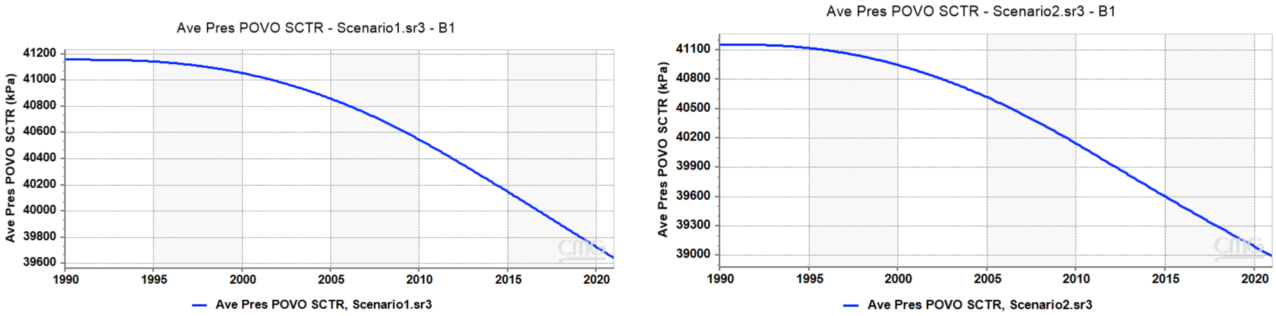

(a) Graph of the average pressure over time of sector B1 in scenario 1

(b) Graph of the average pressure over time of sector B1 in scenario 2

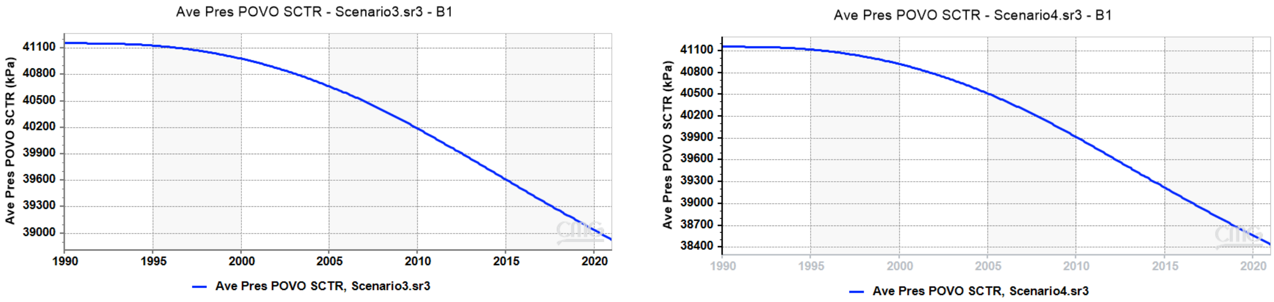

(c) Graph of the average pressure over time of sector B1 in scenario 3

(d) Graph of the average pressure over time of sector B1 in scenario 4

Figure 83: Graph of the average pressures over time of sector B1 in scenarios 1 (a), 2 (b), 3(c), and 4 (d)

However, the horizontal occupation of the architectural elements seem to play a role in the vertical pressure distribution. In the case of scenario 2, the architectural elements are less distributed over the non-continuous layers in comparison with the other scenarios (figures 33 to 35). The architectural elements, in scenario 2, are more located at the sides of the model, having almost no elements in the center. This absence of architectural elements creates higher pressure decrease locally in the non-continuous layers, resulting in higher gas fluxes due to increased pressure differences. Thus even though the average permeability of scenario 2 is higher than that of scenario 3, the pressure differences between the boundaries of sectors B2 and B1 at certain locations are greater in scenario 2 than in scenario 3. This can be explained by the distribution of architectural elements in both scenarios. In scenario 2, the channels and crevasse elements are distributed more toward the sides of the model, creating a central zone with almost no architectural elements. In contrast, the architectural elements in scenario 3 are more evenly distributed across the model (figures 36 to 38). As a result, scenario 2 exhibits locally lower average permeabilities than scenario 3, which leads to higher pressure increases with depth ([Fuquan et al., 2019]). Thus, even tough, scenario 2 is vertically more connected and has a higher average pressure than scenario 3, the pressure differences between sector B2 and B1 are greater in scenario 2: the pressure drop in scenario 2 is in a location in the center (with almost no architectural element input) 35933 kPa - 35673 kPa = 260 kPa while at this exact same location for scenario 3 36866 kPa - 36654 kPa = 212 kPa pressure difference between the boundaries of sectors B1 and B2 (figure 84).

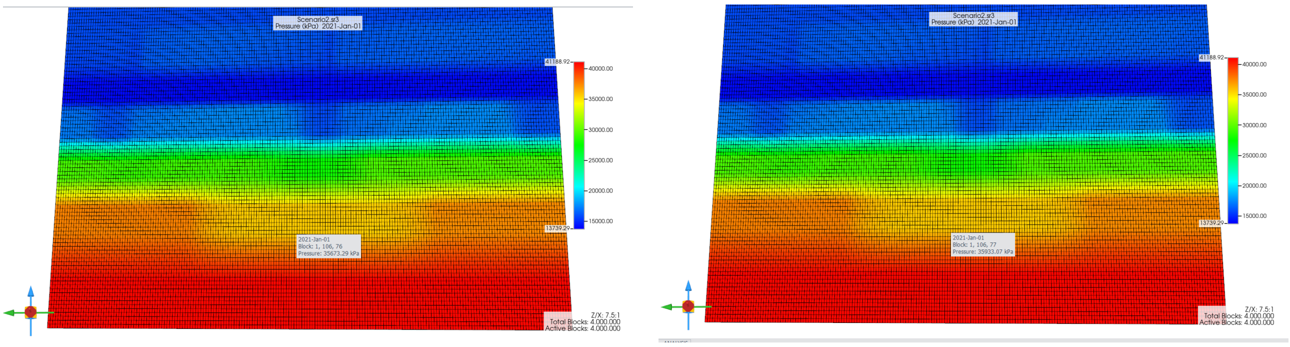

(a) Screenshot of pressure distribution of scenario 2 at the end of simulation in coordinates 1, 106, 76 (bottom boundary sector B2)

(b) Screenshot of pressure distribution of scenario 2 at the end of simulation in coordinates 1, 106, 77 (upper boundary sector B1)

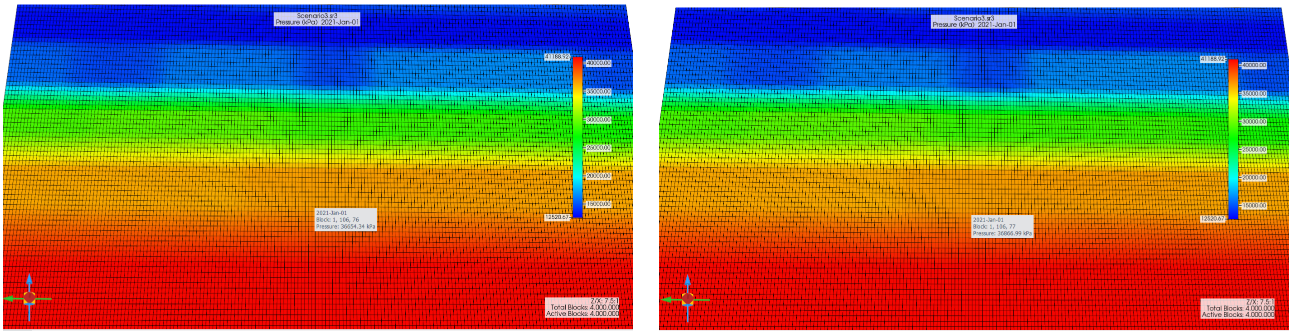

(c) Screenshot of pressure distribution of scenario 3 at the end of simulation in coordinates 1, 106, 76 (bottom boundary sector B2)

(d) Screenshot of pressure distribution of scenario 3 at the end of simulation in coordinates 1, 106, 77 (upper boundary sector B1

Figure 84: Screenshots of pressure distribution in scenarios 2 and 3 at the end of simulation in coordinates 1,106,76 and 1, 106, 77 (boundary between B2 and B1)

The gas flux from A to B1 follows the same trend as the flux from sector B1 to sector B2: scenario 4 exhibits the largest flux, followed by scenarios 2, 3 respectively and the lowest flux is observed in scenario 1 (figures 42, 45b, 48b, 51b and 54b). In this situation, the A and B1-sectors have identical permeability values across all scenarios since the boundary between both sectors contain continuous layers. The only variable, again, is the pressure gradient, resulting from permeability differences of overlying layers, determining the flow velocity (Darcy). In scenario 4, the severe pressure drop due to poor B-zone connectivity pulls more gas upward from the A zone. The greater the resistance to vertical migration within the B zone, the higher the pressure sink generated, and thus the stronger the vertical pressure gradient between the A- and B1-sectors (figure 85) ([Fuquan et al., 2019, Zhao et al., 2025]). Additionally, scenario 2 shows a slightly higher flux than scenario 3, which also matches the observations of the flux from B1 to B2. Since the B1- and A-sectors are continuous for all scenarios, the pressure drops at the same rate over distance in these sectors. Therefore, the local higher pressure drop in scenario 2, stays locally higher, inducing faster gas flow in that area. This results in a slightly higher flux in scenario 2 in comparison to scenario 3.

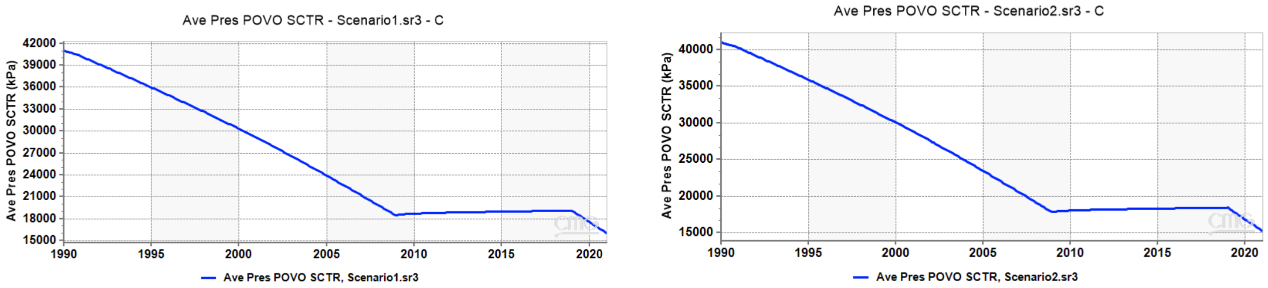

(a) Graph illustrating the average pressure over time of sector C in scenario 1

(b) Graph illustrating the average pressure over time of sector C in scenario 2

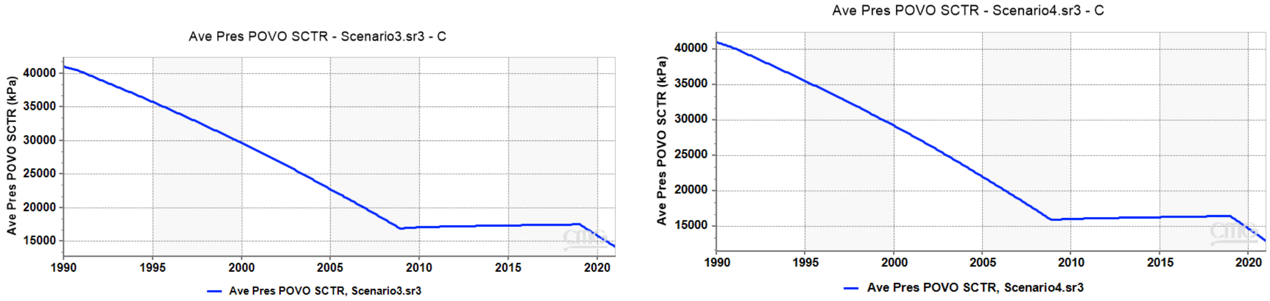

(c) Graph illustrating the average pressure over time of sector C in scenario 3

(d) Graph illustrating the average pressure over time of sector C in scenario 4

Figure 85: Graphs illustrating the average pressures over time of sector C in scenarios 1 (a), 2 (b), 3(c), and 4 (d)

Therefore, although scenario 1 has the most favorable reservoir properties overall, its pressure gradient is too small to induce large volumes of gas to move from sector A to sector B1. Scenario 2 shows a slight higher gas flux than scenario 3, following the same trend as observed for the gas flux from B1 to B2. However, the difference in flux decreased.

This reinforces the idea of a tipping point between permeability-controlled and pressure-controlled flow. Scenarios 2 and 3 occupy a transitional regime, where small differences in either factor can reverse their relative influence on gas flux. While scenario 1 is permeability-dominated and scenario 4 is pressure-gradient-dominated, scenarios 2 and 3 offer insight into the complex interplay between the two drivers in low-permeability systems.

These findings support the emerging hypothesis that permeability dominates flow behavior close to the producing zones (e.g., C1 and B3), while pressure gradient becomes increasingly more important in deeper parts of the reservoir with more continuous layers or in regions where vertical permeability is especially low. This influence of permeability and pressure gradients also explains why certain flux directions (such as from sectors B1 to B2 or sectors A to B1) show trends that differ from those involving better-connected units (like sectors B3 to C), despite all being governed by the same physical law (Darcy's Law). The mechanism of vertical permeability and pressure is commonly observed in low-permeability reservoir studies, where either permeability barriers or pressure depletion can dominate flow behavior depending on depth, distance from the well, and connectivity ([Zhao et al., 2025, Fuquan et al., 2019]). In addition to vertical permeability, horizontal occupation of higher-permeability input seems to determine pressure gradients across layers. In cases with lesser to no architectural elements horizontally, a higher pressure decline can be observed locally as a result of a lower average permeability over this interval. The average pressure of a sector could give a distorted picture of the actual existing local pressure differences, inducing gas movement between sectors.

These results show that there is communication between the A and C sectors across all scenarios. In every scenario, the gas is moving upward from the A-zone to the B-zone. Together, the scenario results demonstrate that stratigraphic cross flow in the Upper Slochteren Member is not purely a function of connectivity or pressure but rather a product of their interaction, which is strongly depth dependent. This nuanced control highlights the importance of modeling architectural heterogeneity at an appropriate scale to capture realistic recharge behavior.

6.3 Impact of Modeling Assumptions

During the modeling process, several assumptions were made to improve model feasibility and simplify the simulations. However, some of these assumptions may influence the model outcomes and affect the simulation results. Therefore, it is important to discuss the potential impacts of these assumptions and outline whether their influence could be positive or negative. In this chapter, the assumptions made in Chapter 4.3 and their effects are evaluated.

The assumptions can be grouped into two categories: geometrical and geological assumptions. Geometrical assumptions include those that affect the geometrical properties of the model, such as layer thickness, channel and crevasse dimensions, grid size, dip, and layer trajectories (Assumptions 1, 2, 4, and 13).
Geological assumptions encompass those influencing geological properties, such as depositional environment, horizontal and vertical permeability, porosity, and sand input (Assumptions 3, 5 to 12, and 14 to 19).

The geometrical assumptions simplify the geometry of the model, which may influence simulation responses. In reality, the layers of the Upper Slochteren Member exhibit a gentle dip, whereas they are assumed to be horizontal in the model (Assumption 1). Dipping formations could slightly alter local connectivity between zones and promote lateral gas migration, as horizontal permeability is typically higher than vertical permeability ([Bei et al., 2022, Philip et al., 2012]). Additionally, the zones of the Upper Slochteren do not have uniform thickness, which has been assumed in the models (Assumption 2). This can have both positive and negative effects on gas fluxes: thicker layers with higher sand content (and thus higher permeability and porosity) may increase connectivity but reduce pressure gradients. Conversely, thicker shale/mud layers (with lower permeability and porosity) would reduce connectivity but enhance pressure gradients ([Fuquan et al., 2019, Zhao et al., 2025, Bell et al., 2018, Liu et al., 2017, Hovadik and Larue, 2007]). In the model, architectural elements are assumed to follow uniform trajectories (Assumption 4). In reality, trajectories would vary (in)between architectural elements, potentially affecting connectivity ([Cao et al., 2017]). However, since connectivity is tested across various scenarios, differences in element trajectories are not expected to introduce significant bias into the results. Furthermore, the dimensions of architectural elements are exaggerated in the model (Assumption 13), creating a higher degree of connectivity and more flow pathways. In reality, these elements are smaller and thinner, which would reduce connectivity and lead to lower gas fluxes than those observed in the model. The exaggerated dimensions likely enhance gas distribution and may cause some overestimation of connectivity in the simulation results.

The geological assumptions simplify the geological aspects of the model and most assumptions are interconnected. In the model, single channels are represented (Assumption 3), while in reality, the Upper Slochteren consists of multiple stacked small channels. This assumption omits the influence of thin baffles between stacked (or amalgamated) channels. However, since average permeability and porosity values are applied to the channel units, the influence of such baffles is implicitly accounted for and is not expected to significantly impact the overall simulation outcomes. The A-, C1-, and C3-zones are modeled as consisting only of channels (A and C1) and a combination of channels and crevasses (C3) (Assumptions 5 and 6). Similar to Assumption 3, in reality, small baffles are present between these deposits. Again, using average permeability and porosity values limits the potential influence of these baffles on gas fluxes, which should not result in major deviations in the overall trends.
Assumption 7 is considered to have a more pronounced effect. In the model, three layers are assumed to contain architectural elements and crevasses. However, such extensive architectural elements are not observed in well logs or permeability and porosity data from ONE-Dyas. Nonetheless, data from adjacent wells indicate series of sand influxes within the B- and C2-zones. In the model, the volume and size of architectural elements are exaggerated to test the potential influence of vertical connectivity on flow and recharge behavior in the Upper Slochteren Member. In reality, architectural elements would occupy smaller volumes or be absent, which would reduce connectivity and recharge potential ([Liu et al., 2017, Hovadik and Larue, 2007, Xue et al., 2021, Porten et al., 2016]). This assumption strongly influences the simulation results by not only creating more connected pathways, but also increasing the average permeability and porosity within these layers. The resulting higher permeabilities and porosities further reduce capillary pressures (figure 16).
Average permeability and porosity values are used for architectural elements in the A, C1, and C3 zones, as well as for the less continuous B and C2 zones (Assumptions 8 to 12, 14, and 15), in order to simplify the model. In reality, permeability and porosity vary per 0.124 m interval, as shown in the ONE-Dyas data. These variations could locally enhance or restrict flow. However, applying average values ensures that the overall trends in flow behavior are captured, with local variations having only minor effects on the general results. The influence of varying horizontal and vertical permeability and porosity will be explicitly tested in the sensitivity analysis to

further assess their effect on gas fluxes in the model.

A uniform water saturation of 0.35 was assumed across the entire model. This choice was made due to the absence of water saturation data at the start of production from the B well. According to the literature, mud layers typically exhibit higher water saturation than sand layers ([Iqbal and Rezaee, 2020]). It is also well documented that water saturation strongly influences gas mobility in porous media ([Tan et al., 2021, Cao et al., 2017, Iqbal and Rezaee, 2020]). The impact of varying water saturation will be addressed in the sensitivity analysis to evaluate its effect on gas fluxes in the model. During the simulations, it was assumed that only the C1 and C3 zones were perforated and produced at a constant rate (Assumptions 17 and 18), whereas in reality, the A-zone is also perforated and the production rate varies over time. This modeling choice was made to drive flow from the A-zone toward the producing zones, enhancing the potential observation of vertical recharge effects. The constant production rate was selected due to the absence of detailed production data. In reality, this assumption could lead to differences in pressure behavior: production from the A-zone would reduce pressure in the A-zone, potentially reversing the pressure difference relative to the B-zone. In the model, the A-zone maintains a higher pressure than the B-zone, facilitating upward gas migration. Including realistic A-zone production would likely reduce this driving force and alter vertical flow dynamics. The reversed pressure differences between the B- and A-zones, could negatively influence the seen flux from the A- to the B1-sector, since smaller pressure differences would be present in reality.

By using the SWINIT keyword in the CMG basecase simulations, initial water saturation can be defined. In the model, an initial water saturation of 0.35 was chosen. In order to reach a hydrostatic-capillary equilibrium with this setting, CMG scales the capillary pressure curves that were added in the software (Assumption 20). With this setting enabled, CMG does not use the original capillary pressure curves, but instead applies a scaled version. This approach provides a useful way to test the influence of geological parameters under a simplified capillary pressure setting. However, in reality, capillary pressure behavior would be comparable to the values specified in the SWGT tables. Variations in capillary pressure at the layer interfaces influence the movement of water-saturated regions during gas migration ([Tsypkin and Shargatov, 2018]), and determine the saturation distribution throughout the reservoir during production, which in turn affects gas movement and recovery ([McPhee et al., 2015]). Higher capillary pressures also act to retain water in the pore space, making it more difficult for the gas to flow through the reservoir ([Cluff and Byrnes, 2010, Kadkhodaie and Kadkhodaie, 2022]). In the Discussion chapter 6.5, the SWINIT-ADJMOB keyword is activated to investigate the influence of the original capillary curves on both gas and pressure distribution. In addition to using the SWINIT keyword, gas flow was allowed at water saturations below 1.0. This was done to study the effect of gas movement in zones with high water saturation, and to encourage gas movement within the model. Since this study is not focused on matching realistic reservoir behavior, but rather on exploring under which circumstances communication between the A and C1 zones may occur, this assumption aligns with the overall objective of the study. However, this assumption does significantly influence the outcome of the results. Higher residual gas saturation (Sgr) would be present in lower mobile water saturation values in the reservoir, which would in turn lead to higher relative gas permeabilities and therefore greater gas flow volumes. Residual gas saturation is known to be one of the key parameters governing cumulative gas production in producing layers ([Rostami et al., 2020]). To evaluate the influence of this effect, a sensitivity analysis has been conducted (chapter 6.5), in which higher residual gas saturation values were applied across all rock types, consistent with values commonly reported in the literature.

The various assumptions made throughout the modeling process have differing degrees of influence on the simulation results, ranging from minor to more substantial effects. These potential impacts will be taken into account in the final discussion, where the research questions and underlying hypotheses will be critically evaluated in light of both the results and the assumptions presented here.

6.4 Sensitivity Analysis Basecase

In this chapter, the results of the sensitivity analysis will be discussed, with the aim of determining the influence of certain parameters on gas flow in the basecase models. Additionally, the parameter ranges that result in the largest fluxes into the C1-zone will be identified, as these parameters have the greatest impact on crossflow behavior.
As mentioned in the chapter 4.2, the extended sensitivity analysis was performed only for Scenario 4. This choice for this scenario only is because scenario 4 exhibits the smallest fluxes into the C-sector and represents the assumed most realistic scenario in terms of sand input in the B- and C2-zones. Thus, the effect of the varying parameters can be observed best.

An extended sensitivity analysis was not conducted for the other scenarios because the results of the scenario 4 analysis can also be used to interpret trends in the other scenarios. In the base case simulations, differences in fluxes per sector and per scenario have already been discussed. These differences primarily result from variations in connectivity and the corresponding average permeability and porosity between the scenarios. Thus, this information can be used to predict responses in other scenarios on the same parameter variations.
However, since this argument alone is not sufficient to fully justify omitting all variations in the other scenarios, it was decided to run manual simulations for scenarios 1, 2, and 3, varying water saturation to observe their influence. The main purpose of these manual simulations is to provide comparison material for the extreme values that are used in the sensitivity analysis of scenario 4. For example, in the B zone of scenarios 1, 2, and 3, the water saturation was set to 0.96 as an extreme test. Thus, while for scenario 4 a wider range of values (figure 29) is tested in the extended sensitivity analysis, for the other three scenarios only extreme values (such as 0.96 for water saturation) were simulated manually to observe their effect. This allows for a comparison of extreme-case results and supports the interpretation of how the trends identified in scenario 4 might apply across the other scenarios within the tested parameter ranges. It is not necessary to conduct a manual sensitivity analysis for permeability, as the influence of permeability on flow behavior has already been demonstrated through the differences observed between the basecase scenarios. The objective is therefore not to re-explore this relationship, but rather to assess how the system responds when permeability is increased beyond the ranges present in the initial scenarios.

The sensitivity analysis and manual simulations allow the observation of the impact of changing one parameter at a time. This approach aligns with the objective of this study: to identify which parameters most strongly influence and enhance vertical crossflow.

It is important to note that this sensitivity analysis is not intended to predict the exact flux values for each scenario, but rather to provide valuable insights into which parameters drive increased fluxes. The focus is on observing the trend, flow behavior and possibility of stratigraphical recharge, not on matching absolute values between scenarios.

6.4.1 Manual Analysis Basecase

The first set of manual simulations was performed with a modified water saturation of 0.96 in the B- and C2-zones. All other parameters remained unchanged. This water saturation value corresponds to the upper end of the range used in the extended sensitivity analysis of scenario 4.

The gas influx from sector B3 into sector C follows the same trend as observed in the base case scenarios. The total cumulative gas volume entering the C-sector is highest for scenario 1, followed by scenarios 2 and 3, respectively (figures 55b, 56b and 57b). However, major differences in the absolute cumulative gas flux volumes can be observed. In scenario 1, the base case total gas flux volume into the C-sector was approximately 8 × 10^7 m^3, whereas in the current simulation it is only about 1 × 10^6 m^3 (figures 45a and 55b). Similar decreases in total gas volume are observed in the other two scenarios. In addition, the relative differences between scenarios have shifted: whereas in the base case the fluxes of scenarios 1 and 2 were closer, they are now more similar between Scenarios 2 and 3.
The gas influx from the A sector into sector B1 also follows the same trend as in the base case: highest for scenario 2 and lowest for scenario 1. However, the total gas volumes have changed as well. In the base case, the cumulative gas volume from sector A to B1 for scenario 1 was around 1 × 10^6 m^3, whereas it is now nearly 2.4 × 10^6 m^3 (figures 55a, 56a and 57a). A higher water saturation in the B-zone thus appears to have a negative impact on the total gas volume entering the C sector from sector B3, and a positive impact on the total gas volume entering sector B1 from sector A.

Differences in average pressures can also be observed across all scenarios. The average pressure throughout the model decreases significantly (figures 44, 47, 50 and 86).

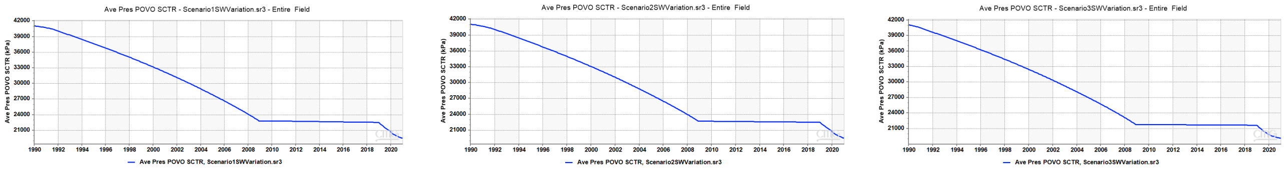

(a) Graph illustrating the average pressure over time for the entire field in scenario 1 with SW=0.96 for the B- and C2 zones

(b) Graph illustrating the average pressure over time for the entire field in scenario 2 with SW=0.96 for the B- and C2 zones

(c) Graph illustrating the average pressure over time for the entire field in scenario 3 with SW=0.96 for the B- and C2 zones

Figure 86: Screenshots of the average pressure over time of the entire field in scenarios 1 (a), 2 (b) and 3 (c) with SW=0.96 for the B- and C2-zones

The observed reduction in flux into the C sector, the increase in flux into the B1 sector, and the overall decrease in pressure across the sectors can be linked to changes in relative gas permeability (krg) caused by the higher water saturation. At higher water saturations, a greater fraction of the pore space is occupied by water, which restricts gas flow and leads to lower krg values ([Poilkar et al., 1990, Cui et al., 2024]). Lower krg effectively reduces the permeability to gas, resulting in sharper pressure declines both over time and across distance ([Zhao et al., 2025, Fuquan et al., 2019]). These sharper pressure gradients cause larger pressure differences deeper in the model, as observed in the pressure distribution maps of the three scenarios than in the basecase simulations (figures 87, 99, 102 and 104). As effective permeability decreases due to lower krg values, the gas flux into the C sector decreases. However, the resulting stronger pressure gradients further away from the well (deeper) creates higher pressure differences over distance, thereby promoting gas movement into zones such as B1. Additionally, the increase of gas flux from A into B1 can be explained by the capillary difference between the A- and B1-sectors which arise due to different water saturation. The capillary pressure difference can drive gas into B1, even if gas doesn't flow far or fast inside B, which explains the less flux from B3 into C as well.

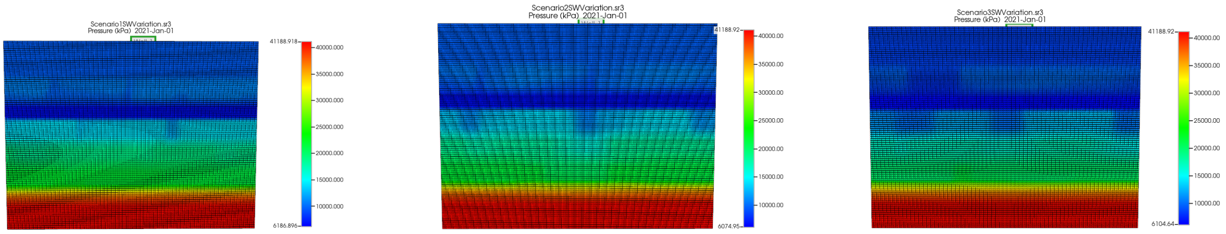

(a) Screenshot of the pressure distribution at the final timestep in scenario 1 with SW=0.96 for the B- and C2-zones

(b) Screenshot of the pressure distribution at the final timestep in scenario 2 with SW=0.96 for the B- and C2-zones

(c) Screenshot of the pressure distribution at the final timestep in scenario 3 with SW=0.96 for the B- and C2-zones

Figure 87: Screenshots of the pressure distribution at the final timestep in scenarios 1 (a), 2 (b) and 3 (c) with SW=0.96 for the B- and C2-zones

6.4.2 Extended Sensitivity Analysis Scenario 4

The extended sensitivity analysis was performed solely on scenario 4. In this analysis, the vertical permeability was multiplied by 0.1, 10, and 100, the porosity was scaled by factors of 0.1 and 4 and two initial water saturation values of 0.65 and 0.96 were tested. These variations were introduced to assess how the magnitude of vertical permeability, net-to-gross, and initial water saturation influence gas movement within the reservoir.

The first set of simulations focused on varying the vertical permeability. When vertical permeability was decreased by a factor of 0.1, the gas flux from sector B3 into the C sector showed a significant reduction compared to the base case (figures 42 and 60b). In contrast, increasing vertical permeability by factors of 10 and 100 led to major increases in gas flux (figure 42). When vertical permeability was multiplied by 10, the total gas flux increased substantially. A further increase to a multiplier of 100 led to an additional rise in flux, although the increase in flux from multiplier 10 to 100 was relatively smaller than the increase of multiplier 10 in comparison to the basecase. A similar trend was observed for the gas flux from sector A to B1 (figures 60a, 61a and 62a). A large decrease in flux occurred with a vertical permeability multiplier of 0.1 in comparison with basecase simulation (figure 42). When multiplied by 10, the gas flux rose dramatically, increasing by a factor of 27 relative to the base case. A further increase to a multiplier of 100 led to a more modest flux increase, roughly by a factor of 2.7 compared to the multiplier of 10 (figure 42). This diminishing return illustrates that while flux increases with vertical permeability, the flux does not increase linearly with increasing permeability as a result of pressure difference feedback.

This behavior is consistent with Darcy's Law, where flow rate increases with higher effective permeability (K/μ). Thus, an increase in vertical permeability should lead to higher flow rates and greater gas movement across the B-zone. However, the results demonstrate that this relationship is not linear, as would not be expected if only permeability were changing. In case of an increase of permeability by factor 10, the Darcy velocity would be increasing by a factor 10 as well in case the pressure difference over distance stays equal. However, the pressure difference over distance changes with changing permeability. Therefore, the explanation of this observation lies in the pressure gradient response. In lower-permeability rocks, pressure gradients are steeper over short distances due to poor connectivity and limited pressure communication ([Fuquan et al., 2019, Zhao et al., 2025]). Increasing vertical permeability improves communication between layers, which causes the pressure gradient to flatten ([Blunt, 2017]). As vertical permeability increases, the pressure difference between adjacent layers becomes smaller, reducing the other driving force for vertical flow (). Consequently, the resulting gas flux no longer scales directly with permeability increase, and the flow response becomes nonlinear ([Dake, 1983]). Additionally, the overall pressure decline in the reservoir accelerates with higher permeability, because enhanced vertical connectivity facilitates more rapid pressure redistribution ([Blunt, 2017, Dake, 1983]). Although the pressure drop across the entire reservoir becomes larger (i.e., from initial to final pressure), the local pressure differences between sectors such as A and B1 or B3 and C become smaller. This limits the ability of the A zone to sustain high-pressure support in models with very high vertical permeability. This effect is clearly reflected in the average pressure curves of the A-sector across simulations with Kv multipliers of 0.1, 10, and 100 (figure 88).

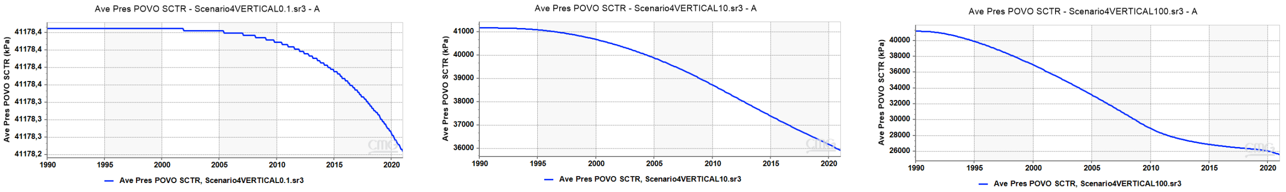

(a) Graph illustrating the average pressure decline over time for the A-sector in scenario 4 with vertical permeability multiplied by 0.1

(b) Graph illustrating the average pressure decline over time for the A-sector in scenario 4 with vertical permeability multiplied by 10

(c) Graph illustrating the average pressure decline over time for the A-sector in scenario 4 with vertical permeability scaled multiplied by 100

Figure 88: Graphs illustrating the average pressure decline over time for the A-sector in scenario 4 with vertical permeability scaled multiplied by 0.1 (a), 10 (b) and 100 (c)

In summary, increased vertical permeability promotes higher gas fluxes between sectors due to higher K/μ values and only moderately decreasing pressure gradients. Since the relative increase in gas flux becomes smaller with further increasing permeability (from 10 to 100), it can be concluded that the pressure differences ( ) between layers are decreasing more rapidly with further increasing permeability, resulting is smaller increase of gas velocity with further increasing vertical permeability. Conversely, lower vertical permeability reduces gas flow, as both K/μ and pressure communication deteriorate. The response of gas flux to vertical permeability variation is thus governed by the combined effects of effective permeability and pressure distribution, with a distinctly nonlinear character caused by the pressure difference response to changing permeability.

The second set of simulations focused on the influence of porosity on gas fluxes between the sectors. The porosity was scaled by 0.1 and 4 to test flow behaviour with decreased and increased porosity. The gas flux from sector B3 to C decreased for both porosity scaled by 4 and scaled by 0.1 in comparison to the basecase simulation (figures 42, 58b and 59b). The flux from sector A into B1, however, increased for the porosity scaled by 0.1 and decreased for the porosity scaled by 4 compared to the basecase simulation (figures 42, 58a and 59a). The increase and decrease in fluxes between sectors across the reservoir for the scaled porosities is driven by the differences in storage capacity. When porosity is increased, more gas can be stored in that layer since there is a higher percentage of pore space ([Ashouri et al., 2024]). Higher storage capacity means that the total volume of gas increased.

Although the flux from B3 to C decreases with increasing porosity, the B-zone retains a larger gas volume, allowing it to sustain gas availability for longer. However, this larger storage created by increased porosity buffers pressure changes more effectively, resulting in lower pressure gradients and thus lower flow rates (figure 89b). This results in lower pressure gradients and lower pressure differences in the reservoir ([Bakhshian et al., 2019, Ashouri et al., 2024]).

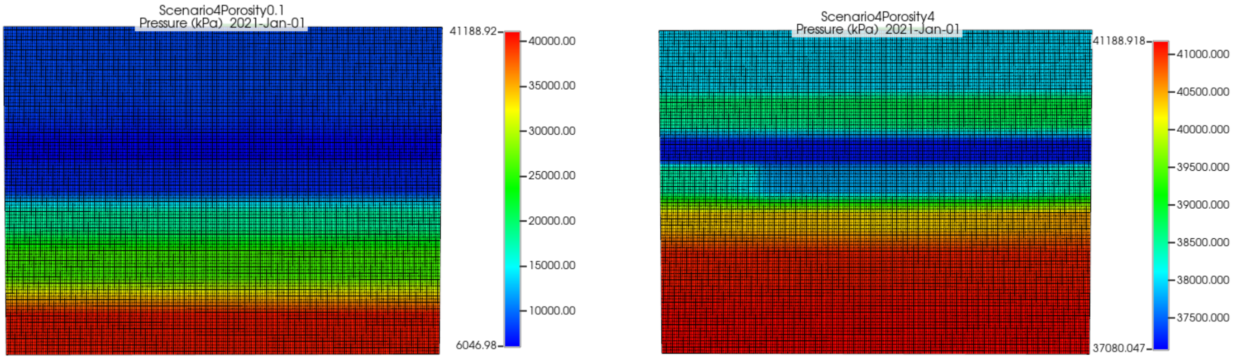

(a) Visualization of the pressure distribution with porosity scaled by 0.1 in scenario 4

(b) Visualization of the pressure distribution with porosity scaled by 4 in scenario 4

Figure 89: Visualization of the pressure distribution with scaled porosity by 0.1 (a) and 4 (b) in scenario 4

These smaller pressure differences in the model impede faster flow velocities from sector B3 to A and sector A into sector B1, explaining the lower gas flux for higher porosity ([Yan et al., 2022])
In the case with decreased porosity, the opposite is happening. Because the porosity is smaller and the storage capacity is lower, a smaller volume of gas is present in the B-zone. This causes the pressure in the B-zone to drop more quickly when gas enters C, which increases the pressure gradient across the model ([Bakhshian et al., 2019, Ashouri et al., 2024]) (figure 89a). Although lower porosity leads to faster pressure drop and steeper pressure gradients, it simultaneously reduces the available pore volume to accommodate flow from sector B3 into sector A ([Yan et al., 2022]). In contrast, the increased pressure gradient leads to higher pressure differences deeper in the model between the boundaries of the B1 and A sectors. This increased pressure difference results in higher gas inflow from A into B1, as per Darcy's Law ([Holtz, 2002]).

In summary, higher porosities lead to increased storage capacity, which can sustain gas flow from the B3-sector into the C-sector. This sustained gas flow results in reduced pressure gradients across the reservoir, decreasing pressure differences between deeper located layers ([Ashouri et al., 2024]). This reduces flow velocity deeper in the reservoir, impeding upward gas movement. In contrast, lower porosities result in higher pressure gradients since less gas is present in the B-zone, creating stronger pressure differences. The increases the flow velocity and promotes upward gas movement in deeper sections. In contrast, with reduced porosity flow can not be accommodated in the near-wellbore area, impeding flow from B3 into A. Conversely, moderate porosity (basecase) allows sufficient pressure gradient and flow capacity, resulting in higher flux. This highlights the non-linear, competing roles of porosity in controlling pressure redistribution and gas mobility in multiphase flow systems.

The last set of simulations focused on the influence of increasing water saturation. This was done by running two additional simulations with different initial water saturations in the B-zone: 0.65 and 0.96.

The gas flux from B3 into C decreased with increasing water saturation in the B-zone. The base case (SW = 0.35) showed the highest flux, while the model with SW = 0.96 showed the lowest (figures 42, 63b and 64b). However, for the gas flux from A into B1, a different trend was observed. In this case, the highest flux occurred at SW = 0.96 and the lowest at SW = 0.65 (figures 42, 63a and 64a). The decrease in flux from B3 into C can be directly explained by the krg values that apply at different water saturations. Higher water saturations result in lower gas relative permeability, reducing the effective permeability and thereby limiting gas mobility and flow velocity. As a result, less gas is able to migrate into the C-zone ([Poilkar et al., 1990, Cui et al., 2024]). The trend observed for the gas flux from A into B1 flux cannot be explained by krg values alone. If only relative permeability effects were considered, the trend SW = 0.35 > 0.65 > 0.96 would be expected, since lower mobility should reduce gas flow in high SW conditions. However, in the SW = 0.96 case, B1 is strongly out of capillary equilibrium with A. The resulting increase in capillary pressure difference between A and B enhances gas migration into B. Additionally, large pressure differences between A and B1 contribute to higher gas velocities (figure 90). While gas cannot continue flowing deeper into B due to the very low krg values at high water saturation, this initial draw into B1 explains the elevated flux observed at the A and B1 interface. The reason the flux from A into B1 is higher in the basecase than in the SW = 0.65 case is that, at SW = 0.65, the capillary suction is not strong enough to compensate for the already sharply reduced gas mobility ([Li and Horne, 2006]). Furthermore, pressure differences between A and B1 are relatively low in this scenario, further decreasing gas velocity according to Darcy's law ([Li and Horne, 2006, Johns, 2004]). In contrast, at SW = 0.96, the capillary suction is significantly stronger, offsetting the low krg and resulting in higher pressure gradients and gas velocities across the A–B1 boundary ([Li and Horne, 2006]).

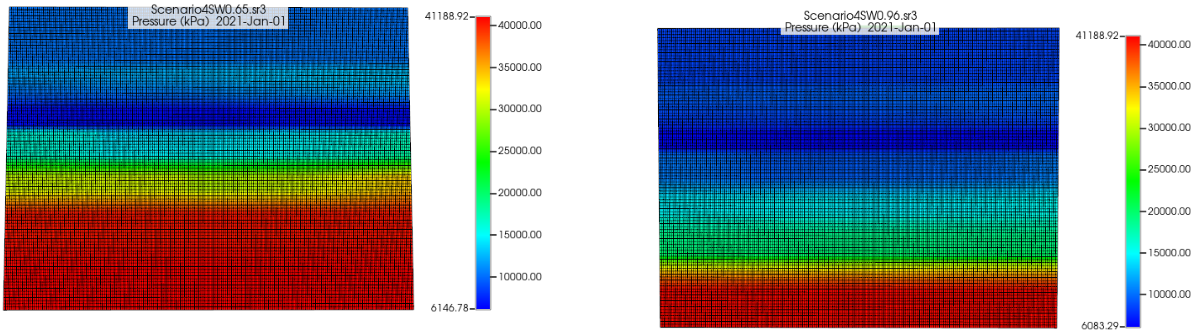

(a) Visualization of the pressure distribution with SW=0.65 in scenario 4

(b) Visualization of the pressure distribution with SW=0.96 in scenario 4

Figure 90: Visualization of the pressure distribution with SW=0.65 (a) and SW=0.96 (b) in scenario 4

Based on both analysis, it can be concluded that if a parameter is changed in one of the four scenarios, the resulting trend in gas flux caused by this parameter change will be consistent across all scenarios. For example, if adjusting a parameter in scenario 1 results in an increase (or decrease) of gas flux from B3 to C, then applying the same parameter change in the other scenarios will lead to a similar increase (or decrease) in flux, following the previously observed trend in magnitude: scenario 1 > 2 > 3 > 4.

6.4.3 Architecture and Geometry

To evaluate the significance of geological architecture and heterogeneity in reservoir modeling, two additional simulations were performed. In the first, both horizontal and vertical permeabilities in the non-continuous layers were averaged and applied uniformly across the model (referred to as AveK). In the second, only the horizontal permeability was averaged (AveKh), while the vertical permeability remained distributed according to the original architectural configuration. The latter was used to isolate the impact of vertical barriers on flow behavior. This setup allowed for an isolated assessment of vertical barriers and geometrical control on flow.

The results indicate that gas fluxes across all sector boundaries increased in both AveK and AveKh compared to the base case model of scenario 4. The highest fluxes from sector A into B1 and from B3 into C were observed in the AveK simulation, followed by the AveKh case (Figures 65 and 66). This trend follows the order: AveK > AveKh » Base case. The increase in fluxes observed in the AveK simulation can be explained by the greater number of effective vertical and horizontal flow pathways and the removal of low-permeability baffles. By averaging both horizontal and vertical permeability, the contrast between the high-permeability architectural elements and the low-permeability matrix (e.g., mud or clay) is eliminated. As a result, the matrix, which acts as a barrier to flow in the basecase scenario, now contributes to gas migration, creating vertically continuous high-relativity permeable pathways throughout the layers. This significantly enhances both lateral and vertical gas movement compared to the basecase, where permeability heterogeneity and internal baffles restrict connectivity. In AveKh, only the horizontal permeability was averaged, improving lateral connectivity. As a result, gas can more easily reach localized high-permeability zones, enhancing flow compared to the base case, but still constrained by the original vertical permeability distribution. In contrast, in the basecase model, gas must migrate through low-permeability matrix material to reach the high-permeability architectural elements, which are only locally developed. While gas flow may increase locally within these elements, the limited access reduces the total flux across the system. It is also important to consider the influence of grid resolution. In models with sharp contrasts in permeability, residual gas saturation (Sgr), or capillary pressure (Pc), grid refinement can significantly affect flow behavior and pressure redistribution. Without sufficient resolution, pressure gradients and fluid exchange between zones, particularly across discontinuous layers, may be underrepresented. This is a well-documented issue in fractured or heterogeneous systems, where accurate simulation of flow between high-permeability features and low-permeability matrix often results in incorrect results.
These results demonstrate that even when average permeability values are preserved, the spatial distribution of permeability, particularly the location and continuity of high-permeability zones, strongly controls gas movement and fluxes. The AveK model consistently shows higher fluxes than the AveKh model, emphasizing the importance of vertical permeability distribution.

Additionally, differences in pressure response were observed between the models. As previously discussed, lower permeability leads to sharper pressure gradients over distance ([Fuquan et al., 2019, Zhao et al., 2025, Blunt, 2017]). In the AveK simulation, the pressure drop is more evenly distributed due to the uniform permeability field, while in the basecase and AveKh models, steeper pressure gradients occur around low-permeability regions. These gradients impact gas flow efficiency and contribute to differences in observed fluxes as well.

Overall, these findings highlight the importance of capturing geological architecture and heterogeneity in reservoir models. Accurately representing the distribution of high-permeability features such as sand bodies or architectural elements is essential for correctly predicting gas flow behavior. The results emphasize that permeability should not be homogenized across layers, as this can significantly distort flow pathways and pressure responses, resulting in unrealistically high fluxes.

6.5 Sensitivity Analysis Capillary Pressure

As discussed in the Impact of Modeling Assumptions section, the capillary pressures added to the SWGT tables were not used in the Basecase simulations. Instead, scaled capillary pressures were applied by CMG. This scaling produces distorted results for total gas flux, as well as for water and pressure distribution over time. Capillary pressure is one of the key factors controlling gas and water distribution in a reservoir during production ([McPhee et al., 2015, Cluff and Byrnes, 2010]). To account for the actual capillary pressures derived from the reservoir properties of the Upper Slochteren Member, the SWINIT-ADJMOB keyword was activated, enabling the model to apply the original capillary pressure curves from the SWGT tables. The effects of this change on gas fluxes were analyzed across all four scenarios.

The gas influx from the B3 sector into the C sector appears to follow the same relative trend in terms of flux magnitude. Scenario 1 shows the largest volume of gas flowing into the C sector, followed by scenarios 2, 3, and 4, respectively (figures 42, 67b, 69b, 71b and 73b). However, significant differences can be observed in the total gas volumes entering the C sector, which are consistently lower than in the Basecase simulations for all scenarios. These lower gas fluxes indicate that the capillary pressures used here are higher than those in the scaled Basecase simulations.

The gas influx from the A sector into the B1 sector follows a pattern not previously observed. While in the Basecase simulation this flux followed the trend $4 > 2 > 3 > 1$, the flux from sector A into sector B1 in the capillary pressure simulations is highest for scenario 2, followed by scenarios 4, 3, and 1, respectively (figures 42, 67a, 69a, 71a and 73a. Additionally, a decrease in total gas volume that moved from the A into the B1 sector decreases as well. Here, the interplay between capillary pressure and flow shows a strong influence. Based purely on the average pressure differences between the B1- and A- sectors, this behavior is not expected, as scenario 4 has the lowest pressure difference at the end of the simulation. However, this can be explained by examining the average pressure evolution of the B1-sector and the gas flow rate between the sectors since the gas flow rate curve follows the same path as the average pressure curve of sector B1 (figure 91).

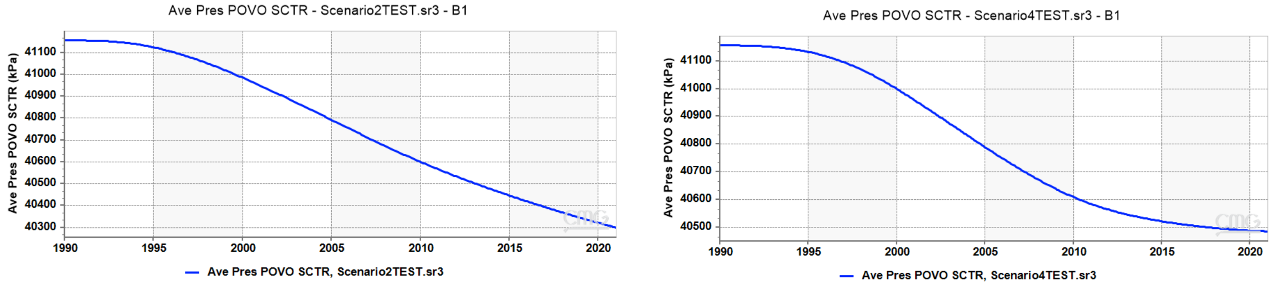

(a) Graph illustrating the average pressure over time of sector B1 in scenario 2

(b) Graph illustrating the average pressure over time of sector B1 in scenario 4

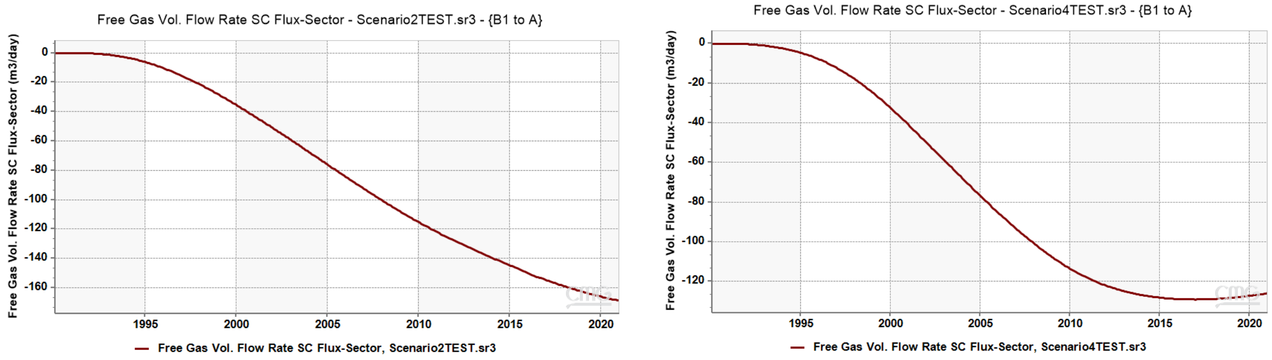

(c) Graph illustrating the gas flow rate between sectors A and B1 in scenario 2

(d) Graph illustrating the gas flow rate between sectors A and B1 in scenario 4

Figure 91: Graphs illustrating the average pressures over time of sector B1 in scenarios 2 (a) and 4 (b) and the gas flow rate between sectors A and B1 in scenarios 2 (c), and 4 (d)

The pressure decline in the B1 sector is steeper between 1995 and 2010 in scenario 4 than in scenarios 1 and 3, leading to higher flow velocities across the A–B1 boundary during this period and resulting in a higher cumulative gas volume in scenario 4. After 2010, flow velocity stabilizes at around 120 m^3/day in scenario 4, while other scenarios show increasing rates over time. Scenario 2 exhibits the highest flux into B1 because the overall average pressure difference between the A and B1 sectors remains the largest, resulting in higher gas flow velocities according to Darcy's Law ([Johns, 2004]). The reason for this higher flux in scenario 2 is consistent with the explanation provided in the Flux Analysis of the Basecase simulations: the presence of architectural elements located to the side induces sharper local pressure gradients due to lower permeability, resulting in stronger local pressure drops over distance and earlier initiation of gas flow.

For both fluxes, a decrease of total gas volume has been observed. Although gas saturations remain similar in the deeper zones in both the basecase and the adjusted capillary pressure simulations, the presence of higher capillary pressures flattens the gas pressure profile. This occurs because higher capillary entry pressures and stronger capillary forces in the overlying layers restrict vertical gas flow and hinder the transmission of pressure drops from the producing zones. As a result, gas pressure in the deeper parts of the model remains higher for longer, creating a flatter vertical Pg profile and delaying pressure equilibration with depth ([Blunt, 2017]). Additionally, with higher capillary pressures, larger local pressure gradients are required to initiate and sustain vertical gas flow, reducing gas flow.

In addition to differences in gas distribution, notable differences in water and pressure distribution are also observed. A substantial increase in water saturation is evident in certain layers across all scenarios (Figure 92b). In the C2-zone, a strong increase in water saturation occurs over time, reaching values of 0.956 after 30 years of simulation. This behavior can largely be attributed to the fact that residual gas saturation (Sgr) in this layer was set to zero, allowing water to fully displace gas without leaving behind a significant residual gas phase. Water is able to imbibe deeply into the initially gas-saturated C2-zone because capillary forces dominate, and no residual gas remains to impede water invasion ([Kantzas et al., 2001]). In the C2-zone, this unrestricted displacement results in near-complete water saturation over time.
This imbibition of water also alters the pressure distribution within the C sector. It can be observed that the pressure in the C2-zone across all scenarios remains higher and does not equilibrate with the surrounding zones (figure 92a). The pressure differences arise because water is nearly incompressible, and no high-mobility pathways are available for pressure dissipation, resulting in poor pressure communication between layers ([Li et al., 2024, Kantzas et al., 2001, Blunt, 2017]). Capillary forces in the overlying layers of the A-zone and parts of the B-zone further impede pressure communication, leading to a reduced pressure drop away from the producing zones. These reduced pressure drops again result in lower gas flow velocities ([Blunt, 2017, Johns, 2004]). The pressure drops between the B1- and A-sectors are also smaller than in the Basecase simulations. This can be attributed to the higher water saturation in the upper parts of the B-zone, which result in lower relative gas permeabilities. As a consequence, pressure transmission through the B-zone is further reduced.

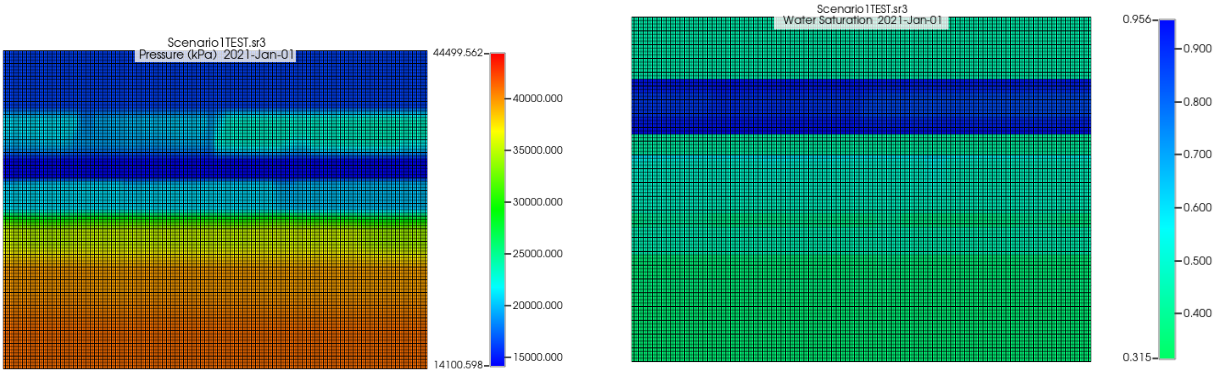

(a) Screenshot of the pressure distribution at the last timestep in scenario 1, as seen in the figure, the pressure in this zone is higher than in the basecase simulations

(b) Screenshot of the water saturation distribution at the last timestep in scenario 1, as seen in the figure, the water saturation is higher than in the basecase simulations

Figure 92: Screenshots of the pressure distribution (a) and water saturation distribution (b) at the last timestep in scenario 1

These results show that scaled capillary pressures by CMG result in overall different outcomes, not only in trend, but also in magnitude of cumulative gas volumes. To further investigate the effect of capillary pressure on flow within the Upper Slochteren member, a manual sensitivity analysis is conducted by multiplying the capillary pressures by 0.01.

The gas influx from sector B3 to sector C follows the same trend as observed in all earlier cases, with the largest flux seen in scenario 1, followed by scenarios 2, 3, and 4, respectively (figures 42, 68b, 70b, 72b and 74b). The total cumulative gas volume flowing into the C-sector also increases compared to previous simulations. In addition to differences in magnitude, the shape of the cumulative gas volume curve over time differs from the simulation with the normal capillary pressures. With reduced capillary pressures, the cumulative gas volume increases almost linearly over time until the shut-in, and shows a less steep increase during the shut-in period. After production is resumed, the cumulative gas volume once again follows a near-linear trend similar to that

observed prior to shut-in.
The gas influx from sector A into B1 follows the same trend as in the Basecase simulations (figures 42, 68a, 70a, 72a and 74b). The flux from A to B1 is again highest in scenario 4, followed by scenarios 2, 3, and 1, respectively. As with the fluxes from B3 to C, the total gas volume transferred from A to B1 has increased compared to the simulation with original capillary pressures. This increase is relatively larger than the increase observed in the B3- to C-sector fluxes.

The observed increase in gas movement can be explained by the fact that pressure differences induced by gas production can now redistribute more easily throughout the model since the capillary forces are not impeding pressure communication anymore, leading to a sharper pressure drop away from the producing zones ([Blunt, 2017, Zhao et al., 2025, Fuquan et al., 2019, Zhang et al., 2017]). These larger pressure differences accelerate gas flow across sector boundaries. The trends and total cumulative gas fluxes observed in this low-capillary pressure simulation are comparable to those found in the basecase simulations. The same physical mechanisms previously used to explain these trends remain valid here as well. The trend observed in the total cumulative gas volume from sector B3 to C is predominantly driven by differences in permeability. Sector B3 consists mainly of continuous layers, where permeability follows the trend: scenario $1 > 2 > 3 > 4$. According to Darcy's Law, flow is governed by permeability and pressure gradients [Johns, 2004]. In this sector, the influence of permeability dominates over pressure gradient effects, resulting in the observed trend.
For the trend of total cumulative gas volume from sector A to B1, it is important to note that pressure declines more sharply over distance in low-permeability layers ([Zhao et al., 2025, Fuquan et al., 2019]. This causes larger pressure differences to develop at the bottom of the reservoir in scenarios with lower permeability, resulting in higher flow velocities and increased gas movement across the A–B1 boundary in comparison with the normal capillary pressure.

The pressure and water saturation distributions appear to follow the same general patterns observed in the Basecase simulations, though slight differences in magnitude are present. This analysis shows that gas fluxes of the reduced capillary pressures simulations are quite similar to the basecase simulations . This suggests that lower capillary pressures promote gas flux throughout the model.

6.5.1 Residual Gas Saturation

The residual gas saturation (Sgr) was assumed to be 0 in the four Basecase simulations as well as in the sensitivity analysis of capillary pressure. However, setting a residual gas saturation of 0 is highly unrealistic and has not been done often in reservoir modeling. It is well established that (Sgr) increases with decreasing porosity ([Suzanne et al., 2001, Suzanne et al., 2003]). Sgr is an important parameter that determines when gas becomes immobile and the volume of gas trapped in the portions of the reservoir that have experienced water imbibition ([Holtz, 2002]). Therefore, since changing water saturations are observed in the models with normal capillary pressures, it is important to test the influence of Sgr on flow behavior, as well as on water and pressure distribution.
To investigate this, the SWGT tables of scenario 4 were modified with higher Sgr values for the different rock types. A Sgr of 0.20 was chosen for RPT 1 and RPT 2, corresponding to the sandstones of the A-, C1-, and C3-zones. For RPT 3 and 4, which correspond to the B and C2 zones, an Sgr of 0.40 was applied. The higher Sgr value for RPT 3 and 4 is based on the fact that these zones consist mainly of low-porosity, low-permeability mudstones, clays, and shales, for which higher Sgr values are commonly reported in the literature ([Rostami et al., 2020]).

The gas flux from sector B3 into sector C decreases compared to the simulation with Sgr $= 0$ (figure 75b). Based on previous observations, a similar reduction in total flux is expected for the other scenarios as well. This decrease in gas flux can be explained by the definition and effect of Sgr: it represents the portion of gas that remains trapped in the pore space and cannot flow ([Holtz, 2002, Cluff and Byrnes, 2010, Kantzas et al., 2001]). When water imbibes into the rock and gas saturation approaches residual gas saturation, capillary forces and relative gas permeability (krg) decline sharply, stopping further gas flow and trapping gas behind the imbibing water front ([Holtz, 2002, Cluff and Byrnes, 2010]). In figure 93, an increase in water saturation is observed at some locations along the boundary between the B3- and C-sectors. This indicates that more gas is being trapped in these zones and is no longer available to flow. With increased Sgr, more gas is immobilized at these locations, leading to a further reduction in gas flow into the C-sector ([Holtz, 2002, Saeedi and Rezaee, 2012]).

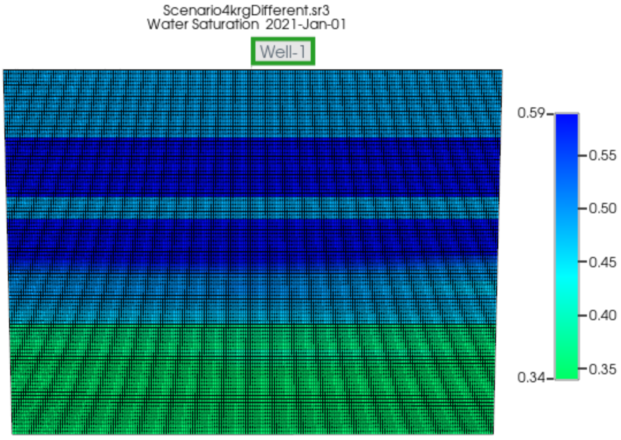

Figure 93: Screenshot of the water saturation distribution with increased Sgr in scenario 4

The gas flux from sector A into B1 also decreases, although the change is minor compared to the normal capillary pressure simulation (figure 75a). A reduction of approximately 0.8 10^5 m^3 in cumulative gas volume is observed with increased Sgr. This difference can be explained by the effect of higher Sgr even though the water saturation in these sectors is almost equal: more gas remains trapped in the pore space and therefore does not migrate towards the B1-sector, reducing flow rates ([Holtz, 2002, Saeedi and Rezaee, 2012, Suzanne et al., 2001]). Additionally, with increasing Sgr, the effective permeability decreases as well, resulting in a lower gas flux. The decrease of effective permeability is the main cause of the decreasing fluxes since less pathways are available.
The water saturation distribution also changes, where water saturation rises to 0.97 in the Sgr = 0 simulation, it increases only to a maximum of 0.59 in the higher-Sgr simulation (figure 93). This is consistent with the expected behavior, as higher Sgr prevents full displacement of the gas phase, thereby limiting water imbibition in affected zones.
Overall, the influence of increased Sgr has a negative impact on total gas volumes moving within the Upper Slochteren Member. The amount of mobile gas available to flow between sectors decreases as a result of higher gas trapping, and water movement is also altered accordingly.

6.6 Recharge

To assess the potential for stratigraphic recharge, the relative pressure increase during the shut-in period (2009–2019) was calculated for all simulation scenarios and is presented in Figure 42. In the actual reservoir, the B well exhibited a pressure increase from 10,500 kPa at shut-in to 14,700 kPa when brought back into production in 2019. This corresponds to a relative pressure recharge of approximately 40%. As the aim of this study was a proof of concept rather than a full history match, absolute pressures between the simulations and field data are not expected to align. Instead, the analysis focuses on relative pressure increases, enabling a meaningful comparison of pressure recovery trends.

The simulation results in Figure 42 reveal that the relative pressure recharge across all tested scenarios ranges from –0.23% to 6.79%. These values fall significantly short of the 40% pressure recovery observed at the B well. Based on this outcome, it can be concluded that stratigraphic recharge alone cannot fully explain the pressure buildup observed during the shut-in period. Nevertheless, this conclusion should be interpreted in light of the modeling assumptions. Several simplifying choices and assumptions may have limited the model's ability to replicate the full range of recharge mechanisms active in the reservoir. Additionally, the model does not attempt to history match pressure trends or precisely replicate reservoir properties, meaning that certain processes contributing to recharge in reality may not be fully captured.

Further insight is provided in Figure 94, which presents the relative recharge percentages for each parameter tested in the sensitivity analysis. This diagram clearly shows that increased vertical permeability has the most pronounced positive effect on pressure recharge in the C sector. Conversely, an increase in porosity (scaled by a factor of four) leads to an overall reduction in pressure within the C zone, likely due to enhanced gas storage capacity and redistribution of pressure away from the well.

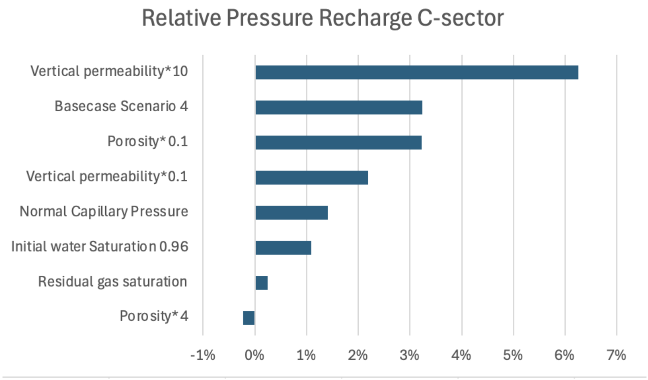

Figure 94: 2D bar showing the relative pressure recharge of the scenario 4 basecase and the sensitivity analysis parameters

These results reinforce that vertical permeability is a key control on recharge potential, but also emphasize that stratigraphic connectivity alone, under the current model configuration, cannot account for the full extent of pressure recovery observed in the field. However, since this study was intended to assess feasibility rather than reproduce historical behavior, the results still provide valuable insight into the relative influence of stratigraphic parameters on pressure redistribution.

6.7 General Discussion

This General Discussion integrates the results of the basecase simulations, sensitivity analyses, and the influence of modeling assumptions to provide a comprehensive answer to the research questions of this study. The goal is to evaluate how architectural connectivity and key reservoir parameters influence vertical cross flow within the Upper Slochteren Member in the near-wellbore area. First, the main outcomes of the basecase simulations are summarized, followed by the effects of varying parameters as observed in the sensitivity analyses. The influence of key modeling assumptions on the outcomes is then discussed, with a focus on identifying which parameters are realistic and relevant under field conditions. Based on this integrated understanding, the main research question and sub-questions are subsequently addressed.

The Upper Slochteren Member consist of a series of depositional cycles in a fluvial system differentiating through distal-proximal changes. The A-zone was deposited at the base in a fan to distal fan environment and is characterized by isolated, thin unconfined sands. The second cycle includes the B- and C1-zones. The B-zone was primarily deposited in a mudflat environment, where fan-front deposits resulted in local sand influx in the B-zone. The second cycle ends with the depositional of the C1-zone in a distal fan to fan environment, containing channel deposits. The last cycle consists of the C2- and C3-zones, with environment ranging from mudflat to fan-front in the C2-zone and distal fan in the C3-zone. The C2-zone consist mainly of mudstone, locally interrupted by sand deposits, while the C3-zone consist mainly of crevasse and channel deposits.

The basecase models showed the influence of different architectural configurations and reservoir properties on flow behavior within the Upper Slochteren Member. Vertical connectivity is highest in scenario 1 and decreases stepwise to zero in scenario 4. The results demonstrate that architecture strongly controls gas fluxes and pressure distribution across the reservoir. Higher connectivity leads to better average reservoir properties (permeability and porosity) and creates more effective pathways for gas flow. In layers closer to the well (e.g., from B3 to C), where architectural differences are most pronounced, gas fluxes are higher in the more connected scenarios due to the presence of vertical pathways. These pathways promote faster gas flow in the near-wellbore region. However, in deeper parts of the reservoir, the influence of pressure gradients increases in scenarios with fewer architectural elements, as pressure drops more sharply in low-permeability rocks ([Fuquan et al., 2019, Zhao et al., 2025]). This sharper pressure drop leads to higher gas fluxes in deeper layers where properties across all scenarios are equal (e.g., from A to B1). Not only the number of vertical pathways determines the gas flux but also the horizontal distribution of sand input also plays a significant role. In regions with little or no sand input, sharper local pressure gradients can develop, as seen in scenario 2. Overall, it can be concluded that architectural elements promote gas flow from nearby zones but can impede gas flow in deeper parts of the reservoir within non-continuous layers. The pressure gradients that arise in lower-permeability regions, due to reduced volumes of architectural elements, enhance gas flow in the deeper continuous layers. Scenario 2 in particular demonstrated this behavior, as the localized distribution of sand input in its lower zones created strong pressure gradients in areas with little architectural input, leading to enhanced gas flow from depth. These findings emphasize the importance of architectural heterogeneity in determining flow behavior throughout the Upper Slochteren Member.

Water saturation showed a strong influence on gas movement within the reservoir. Increasing water saturation to SW=0.96 in the B- and C2-zones led to a significant reduction in the volume of gas moving into the C-sector from the B3-sector. Higher water saturation have lower krg, which reduces the effective permeability of these zones. In addition, as more pore space is occupied by water, less mobile gas is available to flow, and overall vertical gas mobility is reduced across the entire B-zone. In the deeper parts of the reservoir, gas flow from the A- to the B1-sector was promoted because higher pressure differences developed throughout the reservoir as a result of the reduced effective permeability. Additionally, because B1 is strongly out of capillary pressure equilibrium, resulting in higher capillary pressure differences which enhances the gas flux from A into B as well. The sharper pressure gradients that formed in the deeper layers allowed more gas to move toward the upper zones. The analysis of SW=0.65 showed that the interplay between capillary pressure differences and krg determines the ability of gas to invade the B-zone from the A-zone. At moderate SW, the pressure differences are not high enough for gas to move upward. Overall, higher water saturations lead to decreased gas movement in layers close to the well, and to increased gas fluxes from the deeper parts of the reservoir when SW is close to 1-Sgr. When SW is close to 1-Sgr, higher pressure differences and capillary pressure differences are present resulting in higher fluxes from A into B. At moderate SW not close to 1-Sgr, the pressure differences are not large enough to initiate increased gas movement and even show less gas flux than at lower SW.

Finally, the trends observed in these sensitivity analyses showed that changes in parameters, such as water saturation, affect gas flux behavior consistently across all scenarios: the relative ranking of scenarios remains the same even when water saturation is varied.
The extended sensitivity analysis of scenario 4 showed that increasing vertical permeability had a positive effect on overall flow behavior. Gas fluxes between all sectors increased with higher vertical permeability. The highest gas fluxes were observed at the highest vertical permeability values, while the lowest fluxes occurred at the lowest vertical permeability. It can be concluded that the total volume of gas moving upward through the reservoir increases with increasing vertical permeability. In contrast, decreasing vertical permeability resulted in lower gas fluxes across all sectors. The increase in gas flux does not scale linearly with increasing vertical permeability. The increase in flow rate becomes smaller with further increases in vertical permeability. This is because higher vertical permeability flattens pressure gradients due to improved communication, reducing the pressure difference between zones ([Blunt, 2017, Dake, 1983]).
An increase in porosity led to lower gas fluxes in the near-wellbore region and to lower gas fluxes in the deeper sectors. Higher porosity increases storage capacity allowing a larger volume of gas to be present. Higher gas volumes flatten the pressure gradients, resulting in reduced gas fluxes in the reservoir ([Yan et al., 2022]). Lower porosities lead to lower gas fluxes in the near-wellbore area but increased fluxes in the deeper sectors. With lower porosity, less gas is present, increasing pressure gradients. Higher pressure gradients result in higher pressure differences between the sectors deeper in the reservoir, enhancing gas fluxes ([Bakhshian et al., 2019, Ashouri et al., 2024]. These results confirm that porosity controls both gas storage and pressure distribution, directly impacting gas flux trends across the model.
Based on these results and the trends observed between the scenarios, it can be concluded that increasing vertical permeability would consistently lead to increased gas fluxes across the reservoir. The same trends and flux patterns observed earlier are expected to apply across all scenarios when these parameters are increased or decreased.

The introduction of calculated instead of scaled capillary pressures showed the influence of higher capillary forces on gas movement. The normal capillary pressure was much higher than the scaled version, as was observed when the normal capillary pressure was multiplied by 0.01 in the manual sensitivity analysis. This showed that increasing capillary pressures resulted in lower gas influx into the C-sector, with less gas migrating from the B-zone into the C-zone. In addition, gas movement from the A-zone into the B-zone also decreased. Higher capillary forces restrict vertical gas flow and hinder the transmission of pressure drops from the producing zones ([Blunt, 2017]). This leads to a flattening of the gas pressure profile in deeper parts of the reservoir, which impedes the upward movement of gas from the A sector. Because pressure differences decrease with depth when high capillary pressures are present, gas velocities are reduced as well ([Johns, 2004]). Additionally, higher capillary pressures cause a redistribution of water within the reservoir, leading to increased water saturation. Higher water saturations again reduce pressure communication, as water is nearly incompressible and fewer high-mobility pathways are available for gas ([Li and Horne, 2006, Kantzas et al., 2001]). Overall, higher capillary pressures result in decreased gas fluxes across the reservoir in every location. When capillary pressures were reduced again by multiplying them by 0.01, the behavior of the system returned to a state comparable to the basecase simulations, demonstrating that capillary forces play a dominant role in controlling gas movement. In all cases, the relative ranking of scenarios remained consistent across these variations in capillary pressure.

Increased residual gas saturations have a negative influence on gas fluxes across the reservoir. Fluxes between all sectors decrease with increasing Sgr, as more gas becomes immobile ([Holtz, 2002]). With higher Sgr values, a larger portion of gas remains trapped in the pore space and does not move, decreasing overall gas flow ([Saeedi and Rezaee, 2012]). When water imbibes into gas-saturated pores and the gas saturation approaches Sgr, continuous gas pathways disappear, further impeding gas movement. In the simulated models, water saturation increased, which resulted in more residual gas being trapped in the B-zone, reducing total gas movement ([Kantzas et al., 2001, Cluff and Byrnes, 2010]). This effect was clearly observed in the flux from the B3 sector into the C sector, which decreased significantly compared to the Sgr = 0 case. The gas flux from the A- into B1-sector also decreased. The reduction in this flux can also be explained by higher Sgr: even with similar water saturations in these sectors, more gas remains trapped and thus does not migrate toward the B1-sector. Overall, increasing Sgr reduces the amount of mobile gas available to flow between sectors in the Upper Slochteren Member, impeding gas movement. This impediment results in lower gas fluxes with increased Sgr.

The tornado chart in Figure 95 summarizes the effect of varying key parameters on gas fluxes across sector boundaries. This visual representation allows a more direct comparison of the relative influence of each parameter on flow behavior. The chart shows that the gas flux from B3 to sector C is most sensitive to changes in initial water saturation and vertical permeability. Specifically, the highest increase in flux is observed with an increase in vertical permeability, while the most significant reduction occurs with a higher initial water saturation, relative to the base case. For the flux from sector A into B1, vertical permeability also exerts the strongest influence: increasing the vertical permeability leads to the highest positive effect on gas flux, whereas decreasing it results in the greatest reduction. These results confirm that vertical permeability is the most critical parameter governing communication in the reservoir.

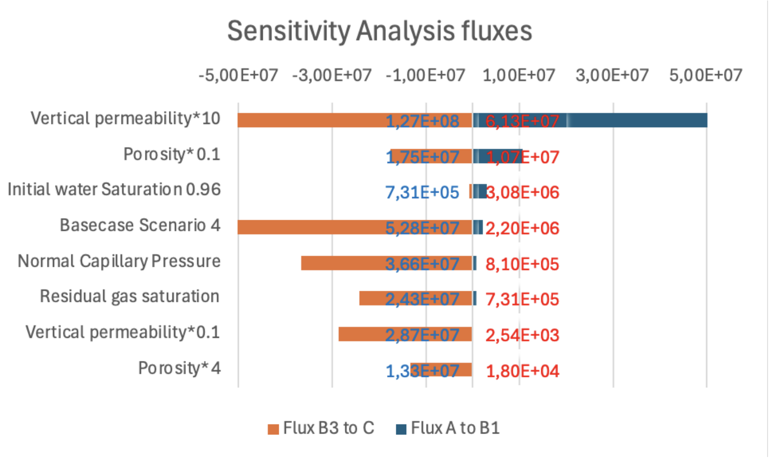

Figure 95: Tornado plot of the gas fluxes from the A into the B1 sector and from the B3 into the C sector of the scenario 4 basecase and sensitivity analysis parameters. This tornado plot illustrates which varying parameter induces the largest change in fluxes in comparison with the basecase

These results show that flow behavior in the reservoir is governed by the interplay between architecture, capillary pressures, water and gas saturations, and residual gas saturation (Sgr). These four parameters are interconnected but are ultimately controlled by the characteristics of the reservoir architecture. The depositional environment determines the volume and distribution of architectural elements, which in turn influence overall permeability and porosity. Permeability and porosity then determine capillary pressures and control pressure distribution within the reservoir. Increased vertical connectivity leads to improved gas movement near the well, whereas less gas moves upward from the lower zones. This trend was consistently observed in each simulation with varying parameters: gas fluxes are highest near the well in the scenario with the highest vertical connectivity, and lowest in the scenario with no vertical connectivity. In contrast, the opposite trend occurs deeper in the reservoir, where the highest gas fluxes are observed in the least connected scenario and the lowest in the most connected scenario. This illustrates the complex interplay between connectivity and pressure distribution, where higher connectivity results in improved pressure communication and lower connectivity leads to poorer pressure distribution.

The results and observations also show that, in these scenarios, there is communication between the C1-zone and the A-zone present. Gas is migrating upward from the A-zone through the B-zone, which was previously considered to act as a seal. However, it is important to note that the four basecase scenarios represent optimistic cases in which the highest gas fluxes are observed. Capillary pressures, water saturations, and Sgr values are expected to be higher than those used in the basecase scenarios. In addition, the high sand input modeled here is considered plausible, but also optimistic. Additionally, it cannot be stated with certainty that the gas moving upward from the A-zone is produced by the well in the C1-zone, since it is not clear which migrated gas is originally from. Moreover, in reality, the A-zone is perforated, leading to decreased pressure in the A-zone as well, limiting upward flow through pressure differences. The reservoir created in this study, has been defined by a size of 2km x 2km x 1km, while in reality the reservoir is way bigger. This influences the pressure distribution as well, since the pressure would redistribute horizontally first instead of redistributing vertically like seen in the simulations. Furthermore, in figure 42 the influx during the shut in period has been tracked, which shows that the recharge occurred can not match the real number observed by ONE-Dyas. This amplifies the observations made in this thesis; there is limited communication between the A-,B and C1-zones present but this communication is limited by the sealing behavior of the B-zone. Therefore, when considering the model assumptions and the results from the sensitivity analyses, it is likely that gas fluxes will be lower than those observed in the basecase scenarios. Based on this can the recharge of the C1 zone, which was observed by ONE-Dyas during the shut in period, not be fully assigned to stratigraphical vertical cross-flow between the A- and C1-zones.

7 Conclusion

The Upper Slochteren member consist of a series of three depositional cycles: the A-zone, the B- and C1 zones and the C2- and C3 zones which are deposited in a mudflat to (distal) fan (front) environments. The reservoir quality is determined by an interplay of several parameters, such as connectivity, the distribution of architectural elements and properties of the geological units (porosity and permeability). This study demonstrates that flow behavior in the Upper Slochteren Member is controlled by a complex interplay between architecture, permeability, porosity, capillary pressures, water saturation, and residual gas saturation (Sgr). These parameters are interconnected, with the depositional architecture ultimately determining the distribution of permeability and porosity, which in turn controls capillary effects and pressure (re)distribution. The simulations show that higher vertical connectivity promotes gas movement near the well but reduces gas flux from deeper zones, which is explained by sharper pressure drops in low-permeability rocks. In contrast, scenarios with lower vertical connectivity show the highest gas fluxes from the lower zones, as sharper pressure gradients develop due to restricted vertical low-permeability flow paths. This pattern was consistent across all sensitivity analyses. Increased vertical permeability and porosity improve gas mobility throughout the model, while higher capillary pressures, water saturations, and Sgr values significantly reduce vertical cross flow. The observed gas movement from the A-zone through the B-zone to the C1-zone confirms that stratigraphic cross flow is present under all conditions.

Since communication can exist through zones of the Upper Slochteren Member that were considered as seal previously, it is important to better map and characterize the properties of these layers, as they can influence recharge behavior under specific conditions. However, it must be emphasized that the basecase scenarios represent optimistic geological cases, with flow-enhancing properties. Therefore, while stratigraphic vertical cross flow may contribute to the recharge of the C1-zone, it is unlikely to fully explain the magnitude of recharge observed in the field. Additional mechanisms, such as structural features or fault-related flow, may also play a role, though these fall outside the scope of this study.

8 Recommendations

In this study, several assumptions were made to improve the feasibility of the basecase models. The sensitivity analysis helped isolate the influence of key parameters, showing that communication through layers previously considered as seals is possible. In reservoir modeling, such sealing layers are often overlooked, under the assumption that their contribution to flow behavior is negligible. However, the results of this study demonstrate that even minimal connectivity through a seal can significantly affect pressure behavior and gas migration. It is therefore recommended that seals be explicitly included in future models and that their petrophysical properties are better characterized.

To further investigate the role of these sealing intervals, future studies should try to construct more geologically realistic models. This requires improved data on capillary pressures, lateral variations in sand content, and permeability distributions. Additionally, the potential influence of microfaults and small-scale structural features has been excluded from this study. Since these features may promote vertical connectivity by creating flow pathways within seals, it is recommended to assess their presence and evaluate their impact on gas movement, particularly within the B-zone.

9 Bibliography

References

[Abdoulghafour et al., 2020] Abdoulghafour, H., Sarmadivaleh, M., Hauge, L. P., Fernø, M., and Iglauer, S. (2020). Capillary pressure characteristics of co2-brine-sandstone systems. *International Journal of Greenhouse Gas Control*, 94:102876.

[Ainsworth, 2003] Ainsworth, R. B. (2003). *Sequence stratigraphic-based analysis of depositional connectivity using 3-D reservoir modelling techniques.* PhD thesis, University of Liverpool.

[Ainsworth, 2005] Ainsworth, R. B. (2005). Sequence stratigraphic-based analysis of reservoir connectivity: influence of depositional architecture–a case study from a marginal marine depositional setting. *Petroleum Geoscience*, 11(3):257–276.

[Ainsworth, 2006] Ainsworth, R. B. (2006). Sequence stratigraphic-based analysis of reservoir connectivity: influence of sealing faults–a case study from a marginal marine depositional setting. *Petroleum Geoscience*, 12(2):127–141.

[Alipour K et al., 2022] Alipour K, M., Kasha, A., Sakhaee-Pour, A., Sadooni, F. N., and Al-Kuwari, H. A.-S. (2022). Empirical relation for capillary pressure in shale. *Petrophysics*, 63(05):591–603.

[Ashouri et al., 2024] Ashouri, H., Mohammadiun, H., Mohammadiun, M., Shafiee Sabet, G., Dibaee Bonab, M., and Sabbaghzadeh, F. (2024). Investigating pressure gradient dynamics in two-phase fluid flow through porous media: An experimental and numerical analysis. *Journal of Applied Fluid Mechanics*, 17(7):1499–1513.

[Bakhshian et al., 2019] Bakhshian, S., Hosseini, S. A., and Shokri, N. (2019). Pore-scale characteristics of multiphase flow in heterogeneous porous media using the lattice boltzmann method. *Scientific reports*, 9(1):3377.

[Bei et al., 2022] Bei, K., Tian, H., Xu, T., Li, Y., and Yin, Z. (2022). Effects of key geological factors in the long-term transport of ch4 and the ch4-hydrate formation behavior with formation dip. *Journal of Natural Gas Science and Engineering*, 103:104615.

[Bell et al., 2018] Bell, D., Kane, I. A., Pontén, A. S., Flint, S. S., Hodgson, D. M., and Barrett, B. J. (2018). Spatial variability in depositional reservoir quality of deep-water channel-fill and lobe deposits. *Marine and Petroleum Geology*, 98:97–115.

[Bello et al., 2021] Bello, A. M., Jones, S., Gluyas, J., Acikalin, S., and Cartigny, M. (2021). Role played by clay content in controlling reservoir quality of submarine fan system, forties sandstone member, central graben, north sea. *Marine and petroleum Geology*, 128:105058.

[Blunt, 2017] Blunt, M. J. (2017). *Multiphase flow in permeable media: A pore-scale perspective.* Cambridge university press.

[Borgh et al., 2018] Borgh, M., Jaarsma, B., and Rosendaal, E. (2018). Structural development of the northern dutch offshore: Paleozoic to present. *Geological Society, London, Special Publications*, 471:SP471.4.

[Busch et al., 2019a] Busch, B., Becker, I., Koehrer, B., Adelmann, D., and Hilgers, C. (2019a). Porosity evolution of two upper carboniferous tight-gas-fluvial sandstone reservoirs: Impact of fractures and total cement volumes on reservoir quality. *Marine and Petroleum Geology*, 100:376–390.

[Busch et al., 2019b] Busch, B., Hilgers, C., and Adelmann, D. (2019b). Reservoir quality controls on rotliegend fluvio-aeolian wells in germany and the netherlands, southern permian basin – impact of grain coatings and cements. *Marine and Petroleum Geology*, 112:104075.

[Cannon, 2024] Cannon, S. (2024). *Reservoir modelling: A practical guide.* John Wiley & Sons.

[Cao et al., 2017] Cao, R., Ye, L., Lei, Q., Chen, X., Ma, Y. Z., and Huang, X. (2017). Gas-water flow behavior in water-bearing tight gas reservoirs. *Geofluids*, 2017(1):9745795.

[Cluff and Byrnes, 2010] Cluff, R. M. and Byrnes, A. P. (2010). Relative permeability in tight gas sandstone reservoirs-the" permeability jail" model. In *SPWLA Annual Logging Symposium*, pages SPWLA–2010. SPWLA.

[Coward, 1993] Coward, M. (1993). The effect of late caledonian and variscan continental escape tectonics on basement structure, paleozoic basin kinematics and subsequent mesozoic basin development in nw europe. In *Geological Society, London, Petroleum Geology Conference Series*, volume 4, pages 1095–1108. The Geological Society of London.

[Cui et al., 2024] Cui, S., Wu, Q., and Wang, Z. (2024). Estimating the influencing factors of gas–water relative permeability in condensate gas reservoirs under high-temperature and high-pressure conditions. *Processes*, 12(4):728.

[Dake, 1983] Dake, L. P. (1983). *Fundamentals of reservoir engineering*, volume 8. Elsevier.

[De Jager, 2007] De Jager, J. (2007). Geological development. *Geology of the Netherlands*, 5:26.

[De Jong et al., 2020] De Jong, M., Donselaar, M., Boerboom, H., Van Toorenenburg, K., Weltje, G., and Van Borren, L. (2020). Long-range, high-resolution stratigraphic correlation of rotliegend fluvial-fan deposits in the central dutch offshore. *Marine and Petroleum Geology*, 119:104482.

[De Jong et al., 2019] De Jong, M. G., Seijmonsbergen, A. C., and De Graaff, L. W. (2019). In search of stratigraphic subdivision of the period 8–0 ka in greenland ice cores. *Polish Polar Research*, 40(2):55–77.

[Donselaar et al., 2011] Donselaar, M. E., Overeem, I., Reichwein, J. H., and Visser, C. A. (2011). Mapping of fluvial fairways in the ten boer member, southern permian basin. *SEPM Special Publication*, 98:105–118.

[Doornenbal et al., 2010] Doornenbal, H., Abbink, O., Duin, E., Dusar, M., Hoth, P., Jasionowski, M., Lott, G., Mathiesen, A., Papiernik, B., Peryt, T., and others, a. (2010). *Introduction, stratigraphic framework and mapping.* EAGE Publications B.V.

[Felder, 2010] Felder, M. (2010). Sedimentology, petrography and reservoir properties of upper slochteren sandstones from well l11b-a06 (renamed from l11-13). Technical Report G741, PanTerra Geoscience B.V., Leiderdorp, The Netherlands. Final internal report prepared for Cirrus Energy Nederland B.V.

[Felder, 2024] Felder, M. (2024). L11 study: Architecture and reservoir quality distribution in the upper slochteren. Internal report for ONE-Dyas, unpublished report by Molenaar Geoconsulting.

[Fisher et al., 2008] Fisher, J. A., Krapf, C. B., Lang, S. C., Nichols, G. J., and Payenberg, T. H. (2008). Sedimentology and architecture of the douglas creek terminal splay, lake eyre, central australia. *Sedimentology*, 55(6):1915–1930.

[Fraser and Gawthorpe, 1990] Fraser, A. J. and Gawthorpe, R. (1990). Tectono-stratigraphic development and hydrocarbon habitat of the carboniferous in northern england. *Geological Society, London, Special Publications*, 55(1):49–86.

[Fuquan et al., 2019] Fuquan, S., Xingxing, S., Yong, W., and Yeheng, S. (2019). Single-and two-phase flow model in low-permeability reservoir. *Petroleum*, 5(2):183–190.

[Gast et al., 2010] Gast, R., Dusar, M., Breitkreuz, C., Gaupp, R., Schneider, J., Stemmerik, L., Geluk, M., Geißler, M., Kiersnowski, H., Glennie, K., et al. (2010). Rotliegend. *Petroleum geological atlas of the Southern Permian Basin area*, pages 101–121.

[Gaupp and Okkerman, 2011] Gaupp, R. and Okkerman, J. (2011). *Diagenesis and reservoir quality of Rotliegend sandstones in the northern Netherlands—A Review*, volume 98, pages 193–226.

[Gee et al., 2008] Gee, D., Fossen, H., Henriksen, N., and Higgins, A. (2008). From the early paleozoic platforms of baltica and laurentia to the caledonide orogen of scandinavia and greenland. *Episodes*, 31:44–51.

[Geiger et al., 2009] Geiger, S., Matthäi, S., Niessner, J., and Helmig, R. (2009). Black-oil simulations for three-component, three-phase flow in fractured porous media. *SPE journal*, 14(02):338–354.

[Geluk, 2005] Geluk, M. (2005). *Stratigraphy and tectonics of Permo-Triassic basins in the Netherlands and surrounding areas.* Utrecht University.

[Geluk et al., 2007] Geluk, M., Dusar, M., and De Vos, W. (2007). *Pre-Silesian*, pages 23–38.

[Gibbons et al., 1993] Gibbons, K., Halvorsen, C., and Siring, E. (1993). Vertical and horizontal permeability variation within a sandstone reservoir based on minipermeameter measurements. *Marine and petroleum geology*, 10(4):325–334.

[Gluyas and Swarbrick, 2021] Gluyas, J. G. and Swarbrick, R. E. (2021). *Petroleum geoscience*. John Wiley & Sons.

[Goupil et al., 2022] Goupil, M., Heap, M. J., and Baud, P. (2022). Permeability anisotropy in sandstones from the soultz-sous-forêts geothermal reservoir (france): implications for large-scale fluid flow modelling. *Geothermal Energy*, 10(1):32.

[Graham et al., 2018] Graham, M., MacAllister, D., Vinogradov, J., Jackson, M., and Butler, A. (2018). Self-potential as a predictor of seawater intrusion in coastal groundwater boreholes. *Water Resources Research*, 54(9):6055–6071.

[Gras et al., 2016] Gras, R., Neale, R., Rossebø, O., and Verkuil, E. (2016). Fault seal in the upper slochteren (rotliegend), case study from the gillian gas field, block l11c, netherlands offshore. In *78th EAGE Conference and Exhibition 2016*, volume 2016, pages 1–5. European Association of Geoscientists & Engineers.

[Grötsch et al., 2011] Grötsch, J., SLUIJK, A., van Ojik, K., KEIJZER, M., GRAAF, J., and STEENBRINK, J. (2011). The groningen gas field: Fifty years of exploration and gas production from a permian dryland reservoir. *SEPM Special Publications*, 98:11–33.

[Haaland, 2018] Haaland, L. C. (2018). Geometry and kinematic evolution of ductile shear zones in the ersfjord granite (1.79 ga), west troms basement complex: A svecofennian accretionary thrust system. Master's thesis, UiT Norges arktiske universitet.

[Heybroek, 1975] Heybroek, P. (1975). On the structure of the dutch part of the central north sea graben. *Applied Science Publishers Ltd (London): 339*.

[Holtz, 2002] Holtz, M. H. (2002). Residual gas saturation to aquifer influx: A calculation method for 3-d computer reservoir model construction. In *SPE Unconventional Resources Conference/Gas Technology Symposium*, pages SPE–75502. SPE.

[Honarpour and Mahmood, 1988] Honarpour, M. and Mahmood, S. (1988). Relative-permeability measurements: An overview. *Journal of petroleum technology*, 40(08):963–966.

[Horn et al., 2021] Horn, S., Gunn, A. G., Petavratzi, E., Shaw, R. A., Eilu, P., Törmänen, T., Bjerkgård, T., Sandstad, J. S., Jonsson, E., Kountourelis, S., et al. (2021). Cobalt resources in europe and the potential for new discoveries. *Ore Geology Reviews*, 130:103915.

[Hovadik and Larue, 2007] Hovadik, J. M. and Larue, D. K. (2007). Static characterizations of reservoirs: refining the concepts of connectivity and continuity. *Petroleum Geoscience*, 13(3):195–211.

[Huysmans and Dassargues, 2011] Huysmans, M. and Dassargues, A. (2011). Direct multiple-point geostatistical simulation of edge properties for modeling thin irregularly shaped surfaces. *Mathematical Geosciences*, 43:521–536.

[Iqbal and Rezaee, 2020] Iqbal, M. A. and Rezaee, R. (2020). Porosity and water saturation estimation for shale reservoirs: An example from goldwyer formation shale, canning basin, western australia. *Energies*, 13(23):6294.

[Jacquemyn et al., 2021] Jacquemyn, C., Pataki, M. E., Hampson, G. J., Jackson, M. D., Petrovskyy, D., Geiger, S., Marques, C. C., Machado Silva, J. D., Judice, S., Rahman, F., et al. (2021). Sketch-based interface and modelling of stratigraphy and structure in three dimensions. *Journal of the Geological Society*, 178(4):jgs2020–187.

[Johns, 2004] Johns, R. T. (2004). Oil recovery. In *Encyclopedia of Energy*, pages 701–713. Elsevier, New York.

[Kadkhodaie and Kadkhodaie, 2022] Kadkhodaie, A. and Kadkhodaie, R. (2022). Chapter 4 - pore type and pore size distribution. In *Reservoir Characterization of Tight Gas Sandstones*, pages 77–100. Elsevier.

[Kantzas et al., 2001] Kantzas, A., Ding, M., and Lee, J. (2001). Residual gas saturation revisited. *SPE Reservoir Evaluation & Engineering*, 4(06):467–476.

[King, 1990] King, P. (1990). The connectivity and conductivity of overlapping sand bodies. In *North Sea Oil and Gas Reservoirs—II: Proceedings of the 2nd North Sea Oil and Gas Reservoirs Conference organized and hosted by the Norwegian Institute of Technology (NTH), Trondheim, Norway, May 8–11, 1989*, pages 353–362. Springer.

[Knox et al., 2010] Knox, R., Bosch, J., Rasmussen, E., Heilmann-Clausen, C., Hiss, M., De Lugt, I., Kasińksi, J., King, C., Köthe, A., Słodkowska, B., Standke, G., and Vandenberghe, N. (2010). *Cretaceous. In: Doornenbal, J.C. and Stevenson, A.G. (editors): Petroleum Geological Atlas of the Southern Permian Basin Area*, pages 211–223. EAGE Publications b.v. (Houten).

[Kombrink and Patruno, 2020] Kombrink, H. and Patruno, S. (2020). The integration of public domain lithostratigraphic data into a series of cross-border north sea well penetration maps. *Geological Society, London, Special Publications*, 494:SP494–2020.

[Lan et al., 2016] Lan, C., Yang, M., and Zhang, Y. (2016). Impact of sequence stratigraphy, depositional facies and diagenesis on reservoir quality: A case study on the pennsylvanian taiyuan sandstones, northeastern ordos basin, china. *Marine and Petroleum Geology*, 69:216–230.

[Lang et al., 2004] Lang, S., Payenberg, T., Reilly, M., Hicks, T., Benson, J., and Kassan, J. (2004). Modern analogues for dryland sandy fluvial-lacustrine deltas and terminal splay reservoirs. *The APPEA Journal*, 44(1):329–356.

[Larue and Hovadik, 2006] Larue, D. K. and Hovadik, J. (2006). Connectivity of channelized reservoirs: a modelling approach. *Petroleum Geoscience*, 12(4):291–308.

[Lauwerier, 2021] Lauwerier, W. (2021). Resource evaluation of the dutch offshore rotliegend play.

[Li et al., 2023] Li, J.-p., Qiu, Z.-y., and Li, H.-y. (2023). Lithology and lithofacies characteristics of deeply buried clastic reservoirs in alternating wet-arid climate and its hydrocarbon significance. In *Journal of Physics: Conference Series*, volume 2594, page 012039. IOP Publishing.

[Li and Horne, 2006] Li, K. and Horne, R. N. (2006). Comparison of methods to calculate relative permeability from capillary pressure in consolidated water-wet porous media. *Water resources research*, 42(6).

[Li et al., 2024] Li, Y., Fu, J., Yan, W., Chen, K., Ding, J., and Wu, J. (2024). Experimental study on the dynamic threshold pressure gradient of high water-bearing tight sandstone gas reservoir. *Frontiers in Earth Science*, 12:1487433.

[Liu et al., 2017] Liu, J., Xian, B., Wang, J., Ji, Y., Lu, Z., and Liu, S. (2017). Sedimentary architecture of a sub-lacustrine debris fan: Eocene dongying depression, bohai bay basin, east china. *Sedimentary Geology*, 362:66–82.

[Lott et al., 2010] Lott, G., Wong, T., Dusar, M., Andsbjerg, J., Mönnig, E., Feldman-Olszewska, A., and Verreussel, R. (2010). *Jurassic. In: Doornenbal, J.C. and Stevenson, A.G. (editors): Petroleum Geological Atlas of the Southern Permian Basin Area*, pages 175–193. EAGE Publications b.v. (Houten).

[Lyu et al., 2017] Lyu, W., Zeng, L., Zhang, B., Miao, F., Lyu, P., and Dong, S. (2017). Influence of natural fractures on gas accumulation in the upper triassic tight gas sandstones in the northwestern sichuan basin, china. *Marine and Petroleum Geology*, 83:60–72.

[McKerrow et al., 2000] McKerrow, W., Mac Niocaill, C., and Dewey, J. (2000). The caledonian orogeny redefined. *Journal of the Geological society*, 157(6):1149–1154.

[McPhee et al., 2015] McPhee, C., Reed, J., and Zubizarreta, I. (2015). Capillary pressure. In *Developments in Petroleum Science*, volume 64, pages 449–517. Elsevier.

[Mijnlieff, 2020] Mijnlieff, H. F. (2020). Introduction to the geothermal play and reservoir geology of the netherlands. *Netherlands Journal of Geosciences*, 99:e2.

[Monsees, 2021] Monsees, A. C. (2021). *Diagenetic controls on fluid flow and mechanical properties in Rotliegend reservoir sandstones.* KIT Scientific Publishing.

[Pereira, 2019] Pereira, G. (2019). Fluid flow, relative permeabilities and capillary pressure curves through heterogeneous porous media. *Applied Mathematical Modelling*, 75:481–493.

[Pharaoh et al., 2010] Pharaoh, T., Dusar, M., Geluk, M., Kockel, F., Krawczyk, C., Krzywiec, P., Scheck-Wenderoth, M., Thybo, H., Vejbaek, O., and Van Wees, J. (2010). *Tectonic Evolution. In: Doornenbal, J.C. and Stevenson, A.G. (editors): Petroleum Geological Atlas of the Southern Permian Basin Area*, pages 25–58. EAGE Publications b.v. (Houten).

[Philip et al., 2012] Philip, C. I., Tiab, D., and Alpheus, O. I. (2012). Vertical-horizontal permeability relationships for sandstone reservoirs. In *SPE Nigeria Annual International Conference and Exhibition*, pages SPE–163011. SPE.

[Poilkar et al., 1990] Poilkar, M., Farouq All, S., and Puttagunta, V. (1990). High-temperature relative permeabilities for athabasca oil sands. *SPE Reservoir Engineering*, 5(01):25–32.

[Porten et al., 2016] Porten, K. W., Kane, I. A., Warchoł, M. J., and Southern, S. J. (2016). A sedimentological process-based approach to depositional reservoir quality of deep-marine sandstones: an example from the springar formation, northwestern vøring basin, norwegian sea. *Journal of Sedimentary Research*, 86(11):1269–1286.

[Ren et al., 2022] Ren, X., Li, A., and Memon, A. (2022). Experimental study on gas–water relative permeability characteristics of tight sandstone reservoir in ordos basin. *Geofluids*, 2022(1):1521837.

[Rostami et al., 2020] Rostami, A., Raef, A., Kamari, A., Totten, M. W., Abdelwahhab, M., and Panacharoensawad, E. (2020). Rigorous framework determining residual gas saturations during spontaneous and forced imbibition using gene expression programming. *Journal of Natural Gas Science and Engineering*, 84:103644.

[Saeedi and Rezaee, 2012] Saeedi, A. and Rezaee, R. (2012). Effect of residual natural gas saturation on multiphase flow behaviour during co2 geo-sequestration in depleted natural gas reservoirs. *Journal of Petroleum Science and Engineering*, 82:17–26.

[Schroot, 1991] Schroot, B. (1991). Structural development of the dutch central graben. *Danmarks Geologiske Undersøgelse Serie B*, 16:32–35.

[Simon et al., 2019] Simon, H., Buske, S., Hedin, P., Juhlin, C., Krauß, F., and Giese, R. (2019). Anisotropic kirchhoff pre-stack depth migration at the cosc-1 borehole, central sweden. *Geophysical Journal International*, 219(1):66–79.

[Sun et al., 2008] Sun, A. Y., Ritzi, R. W., and Sims, D. W. (2008). Characterization and modeling of spatial variability in a complex alluvial aquifer: implications on solute transport. *Water Resources Research*, 44(4).

[Suzanne et al., 2001] Suzanne, K., Hamon, G., Billiotte, J., and Trocme, V. (2001). Distribution of trapped gas saturation in heterogeneous sandstone reservoirs. In *Proceedings of the Annual Symposium of the Society of Core Analysts*, pages 1–4.

[Suzanne et al., 2003] Suzanne, K., Hamon, G., Billiotte, J., and Trocme, V. (2003). Experimental relationships between residual gas saturation and initial gas saturation in heterogeneous sandstone reservoirs. In *SPE Annual Technical Conference and Exhibition?*, pages SPE–84038. SPE.

[Tan et al., 2021] Tan, Y., Zhang, S., Tang, S., Cui, G., Ma, Y., Sun, M., and Pan, Z. (2021). Impact of water saturation on gas permeability in shale: Experimental and modelling. *Journal of Natural Gas Science and Engineering*, 95:104062.

[Trevena, 1989] Trevena, A. (1989). Small faults as barriers to permeability in sandstone gas reservoirs, pattani basin, thailand. *AAPG (Am. Assoc. Pet. Geol.) Bull.;(United States)*, 73(CONF-8905132-).

[Tsypkin and Shargatov, 2018] Tsypkin, G. and Shargatov, V. (2018). Influence of capillary pressure gradient on connectivity of flow through a porous medium. *International Journal of Heat and Mass Transfer*, 127:1053–1063.

[van Oeveren et al., 2017] van Oeveren, H., Valvatne, P., Geurtsen, L., and van Elk, J. (2017). History match of the groningen field dynamic reservoir model to subsidence data and conventional subsurface data. *Netherlands Journal of Geosciences*, 96(5):s47–s54.

[van Uijen, 2013] van Uijen, W. M. (2013). Rotliegend geology in the southern permian basin: the development of synrift sediments and its relation to seismic imaging. Master's thesis.

[Wang et al., 2021] Wang, X., Wang, M., Li, Y., Zhang, J., Li, M., Li, Z., Guo, Z., and Li, J. (2021). Shale pore connectivity and influencing factors based on spontaneous imbibition combined with a nuclear magnetic resonance experiment. *Marine and Petroleum Geology*, 132:105239.

[Witmans et al., 2010] Witmans, N., van Gessel, S., and van Veen, J. H. (2010). Central offshore platform and vlieland basin mapping and modelling - area 2e. *TNO Report TNO*.

[Xue et al., 2021] Xue, X., Liu, Z., Jiang, Z., Zhang, J., and Yang, T. (2021). Static connectivity of fluvial reservoirs and their temporal evolution: An example from densely drilled subsurface data in the sanzhao sag, songliao basin. *Marine and Petroleum Geology*, 134:105327.

[Yan et al., 2022] Yan, G., Li, Z., Galindo Torres, S. A., Scheuermann, A., and Li, L. (2022). Transient two-phase flow in porous media: a literature review and engineering application in geotechnics. *Geotechnics*, 2(1):32–90.

[Zhang et al., 2017] Zhang, Y., Lashgari, H. R., Di, Y., and Sepehrnoori, K. (2017). Capillary pressure effect on phase behavior of co2/hydrocarbons in unconventional reservoirs. *Fuel*, 197:575–582.

[Zhao et al., 2025] Zhao, F., Qiu, X., Sun, A., Deng, T., and Zhang, M. (2025). Research and practice on reasonable displacement pressure limits for low-permeability reservoirs. In *International Field Exploration and Development Conference*, pages 187–195. Springer.

[Ziegler, 1982] Ziegler, P. (1982). Faulting and graben formation in western and central europe. *Philosophical Transactions of the Royal Society of London. Series A, Mathematical and Physical Sciences*, 305(1489):113–143.

[Ziegler, 1990] Ziegler, P. (1990). Collision related intra-plate compression deformations in western and central europe. *Journal of Geodynamics*, 11(4):357–388.

[Ziegler et al., 2004] Ziegler, P., Schumacher, M., Dèzes, P., and Van Wees, J. (2004). Post-variscan evolution of the lithosphere in the rhine graben area: Constraints from subsidence modelling. *Geological Society London Special Publications*, 223:289–317.

10 Appendix

10.1 Porosity and Permeability

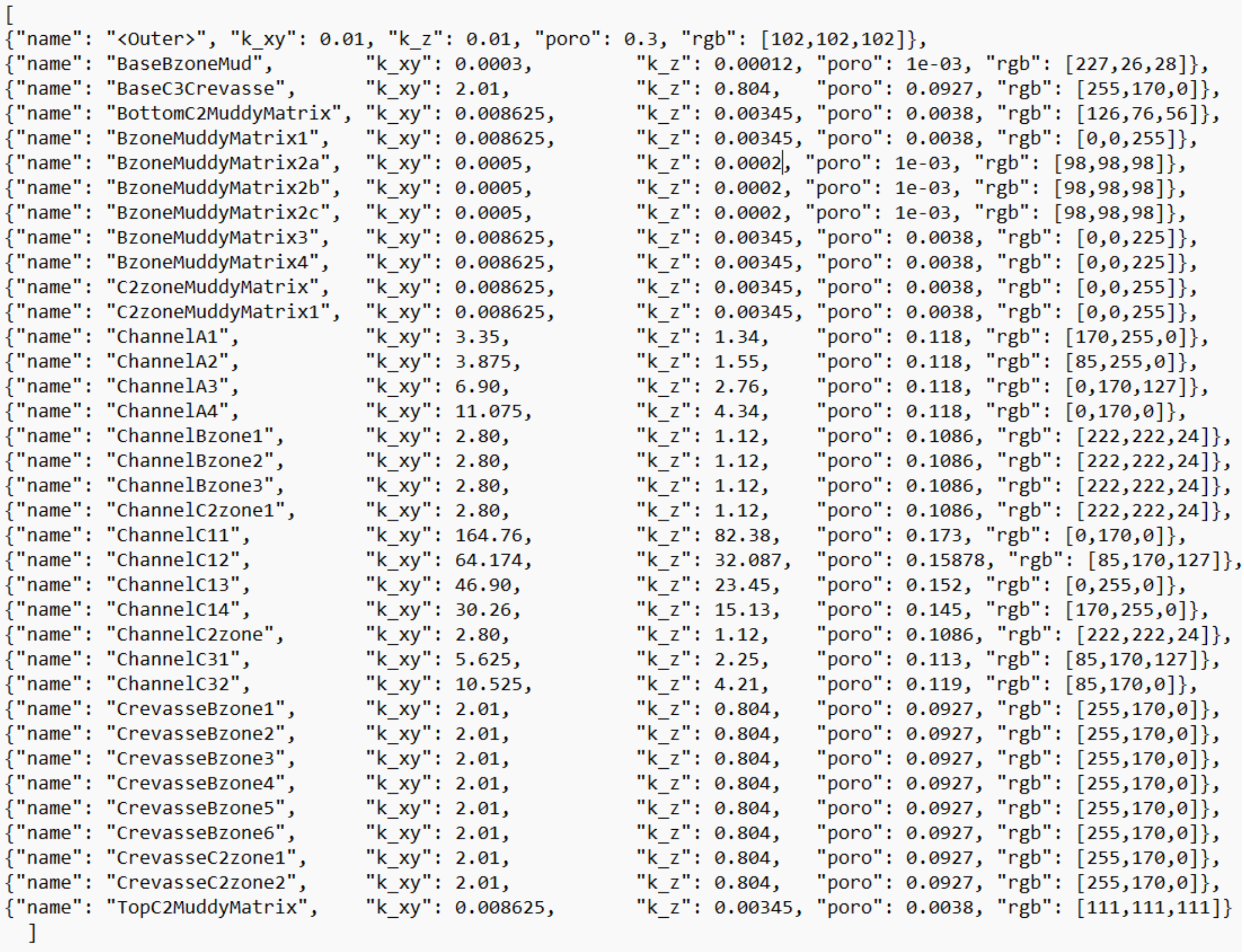

```
[
{"name": "<Outer>", "k_xy": 0.01, "k_z": 0.01, "poro": 0.3, "rgb": [102,102,102]},
{"name": "BaseBzoneMud",        "k_xy": 0.0003,          "k_z": 0.00012, "poro": 1e-03, "rgb": [227,26,28]},
{"name": "BaseC3Crevasse",      "k_xy": 2.01,            "k_z": 0.804,   "poro": 0.0927, "rgb": [255,170,0]},
{"name": "BottomC2MuddyMatrix", "k_xy": 0.008625,        "k_z": 0.00345, "poro": 0.0038, "rgb": [126,76,56]},
{"name": "BzoneMuddyMatrix1",   "k_xy": 0.008625,        "k_z": 0.00345, "poro": 0.0038, "rgb": [0,0,255]},
{"name": "BzoneMuddyMatrix2a",  "k_xy": 0.0005,          "k_z": 0.0002, "poro": 1e-03, "rgb": [98,98,98]},
{"name": "BzoneMuddyMatrix2b",  "k_xy": 0.0005,          "k_z": 0.0002, "poro": 1e-03, "rgb": [98,98,98]},
{"name": "BzoneMuddyMatrix2c",  "k_xy": 0.0005,          "k_z": 0.0002, "poro": 1e-03, "rgb": [98,98,98]},
{"name": "BzoneMuddyMatrix3",   "k_xy": 0.008625,        "k_z": 0.00345, "poro": 0.0038, "rgb": [0,0,225]},
{"name": "BzoneMuddyMatrix4",   "k_xy": 0.008625,        "k_z": 0.00345, "poro": 0.0038, "rgb": [0,0,225]},
{"name": "C2zoneMuddyMatrix",   "k_xy": 0.008625,        "k_z": 0.00345, "poro": 0.0038, "rgb": [0,0,255]},
{"name": "C2zoneMuddyMatrix1",  "k_xy": 0.008625,        "k_z": 0.00345, "poro": 0.0038, "rgb": [0,0,255]},
{"name": "ChannelA1",           "k_xy": 3.35,            "k_z": 1.34,    "poro": 0.118, "rgb": [170,255,0]},
{"name": "ChannelA2",           "k_xy": 3.875,           "k_z": 1.55,    "poro": 0.118, "rgb": [85,255,0]},
{"name": "ChannelA3",           "k_xy": 6.90,            "k_z": 2.76,    "poro": 0.118, "rgb": [0,170,127]},
{"name": "ChannelA4",           "k_xy": 11.075,          "k_z": 4.34,    "poro": 0.118, "rgb": [0,170,0]},
{"name": "ChannelBzone1",       "k_xy": 2.80,            "k_z": 1.12,    "poro": 0.1086, "rgb": [222,222,24]},
{"name": "ChannelBzone2",       "k_xy": 2.80,            "k_z": 1.12,    "poro": 0.1086, "rgb": [222,222,24]},
{"name": "ChannelBzone3",       "k_xy": 2.80,            "k_z": 1.12,    "poro": 0.1086, "rgb": [222,222,24]},
{"name": "ChannelC2zone1",      "k_xy": 2.80,            "k_z": 1.12,    "poro": 0.1086, "rgb": [222,222,24]},
{"name": "ChannelC11",          "k_xy": 164.76,          "k_z": 82.38,   "poro": 0.173, "rgb": [0,170,0]},
{"name": "ChannelC12",          "k_xy": 64.174,          "k_z": 32.087,  "poro": 0.15878, "rgb": [85,170,127]},
{"name": "ChannelC13",          "k_xy": 46.90,           "k_z": 23.45,   "poro": 0.152, "rgb": [0,255,0]},
{"name": "ChannelC14",          "k_xy": 30.26,           "k_z": 15.13,   "poro": 0.145, "rgb": [170,255,0]},
{"name": "ChannelC2zone",       "k_xy": 2.80,            "k_z": 1.12,    "poro": 0.1086, "rgb": [222,222,24]},
{"name": "ChannelC31",          "k_xy": 5.625,           "k_z": 2.25,    "poro": 0.113, "rgb": [85,170,127]},
{"name": "ChannelC32",          "k_xy": 10.525,          "k_z": 4.21,    "poro": 0.119, "rgb": [85,170,0]},
{"name": "CrevasseBzone1",      "k_xy": 2.01,            "k_z": 0.804,   "poro": 0.0927, "rgb": [255,170,0]},
{"name": "CrevasseBzone2",      "k_xy": 2.01,            "k_z": 0.804,   "poro": 0.0927, "rgb": [255,170,0]},
{"name": "CrevasseBzone3",      "k_xy": 2.01,            "k_z": 0.804,   "poro": 0.0927, "rgb": [255,170,0]},
{"name": "CrevasseBzone4",      "k_xy": 2.01,            "k_z": 0.804,   "poro": 0.0927, "rgb": [255,170,0]},
{"name": "CrevasseBzone5",      "k_xy": 2.01,            "k_z": 0.804,   "poro": 0.0927, "rgb": [255,170,0]},
{"name": "CrevasseBzone6",      "k_xy": 2.01,            "k_z": 0.804,   "poro": 0.0927, "rgb": [255,170,0]},
{"name": "CrevasseC2zone1",     "k_xy": 2.01,            "k_z": 0.804,   "poro": 0.0927, "rgb": [255,170,0]},
{"name": "CrevasseC2zone2",     "k_xy": 2.01,            "k_z": 0.804,   "poro": 0.0927, "rgb": [255,170,0]},
{"name": "TopC2MuddyMatrix",     "k_xy": 0.008625,       "k_z": 0.00345, "poro": 0.0038, "rgb": [111,111,111]}
  ]
```

Figure 96: Vertical and Horizontal permeability and the porosity values of all layers and elements

10.2 Assumptions and Justifications

Assumption 1: Horizontal boundary surfaces
In reality, well data from the L11 block indicate a trend of shallower depths of the zones toward the south and east. This trend is more pronounced in the southward direction. For modelling purposes, this depth trend has been neglected, and all zone boundaries are assumed to be horizontal.
Justification: This assumption simplifies model construction. Since the goal of this research is to test the possibility of vertical cross flow and follows a generic approach, the exclusion of tilting has no negative impact on the interpretation or conclusions.

Assumption 2: Uniform thickness across zones
No consistent trend in thickness variation has been observed within the L11 block. While minor local variations in zone thickness exist across the area due to depositional processes, accommodation space, or structural influence, the model assumes each zone has a constant thickness.
Justification: This simplification aligns with the study's generic approach and reduces model complexity without compromising the qualitative objectives of the research.

Assumption 3: One Sketched Channel Represents Multiple Stacked Channels
In the model a single sketched channel may represent multiple stacked channels deposited over different timescales

but in the same location for the A, C1 and C3 zones. These channels (sand layers) are separated by baffles (mud/clay drapes) that locally affect porosity and vertical permeability.
Justification: This heterogeneity is incorporated by varying permeability in the x, y, and z directions and porosity of the single channel. Modeling each individual channel would require multiple horizons, which causes performance issues in RRM. This assumption balances realism with technical feasibility.

Assumption 4: Uniform channel trajectory and extent
Since the depositional environment is assumed to be consistent over time per zone, elements (crevasses and channels) are assumed to follow the same trajectory and continue beyond the model boundaries.
Justification: These assumptions simplify the visualization and avoids unnecessary complexity, while still taking the dynamics of the system into account.

Assumption 5: TopA and C1 zones fully channelized with four channel types
The TopA and C1 zones are interpreted as fan environments. For modelling, they are assumed to consist entirely of channel deposits conform assumption 3: each channel may represent multiple channels of sand layers separated by baffles. Four types of channels are used to reflect varying degrees of heterogeneity induced by baffle content, ranging from moderate/good to excellent petrophysical properties.
Justification: Internal reports and well data indicate variability in baffle distribution influencing reservoir quality ([Felder, 2024]). The choice of different channel types capture local differences in reservoir quality. The volume and quality distribution of the channels in TopA and C1 are based on observed properties differences, with C1 having better reservoir properties than TopA.

Assumption 6: Two-layered channel structure C3 zone
The C3 zone is interpreted as distal fan deposits. These start with crevasse splays embedded in a low-quality matrix, followed by upward-coarsening channels. In the model, this is represented by two channel layers: the lower channels of finer sand and an upper channel of coarser sand, each with distinct reservoir properties. In this model, the base of the C3 zone is assumed to completely consist of crevasses overlaid by finer and coarser sandstones respectively.
Justification: This assumption of layered approach captures the upward improvement in reservoir properties and align with the study's generic approach and reduces model complexity without compromising the qualitative objectives of the research.

Assumption 7: Fan front zones with variable vertical connectivity
Parts of the B and C2 zones are interpreted as fan front environments, consisting of crevasses and channels embedded in a muddy matrix. Well correlations show spatial variability in the presence of channels and crevasses. Four modelling scenarios are defined based on the degree of vertical connectivity between these elements in the B and C2 zones, ranging from connectivity (three points) to no connectivity between the elements. For the elements the best observed properties (derived from the B well data and their corresponding properties in the Por-Perm excel sheet), are chosen (see Method RRM chapter for further explanation).
Justification: The use of multiple scenarios, consisting of (non)connected elements (channels and crevasses) captures the spatial variability and provides valuable insights for the goal of this research.

Assumption 8: Use of Averaged Vertical Permeability and Porosity Values
Vertical permeability (Kv) and porosity values were provided by ONE-Dyas in the form of an Excel dataset, with measurements taken at regular 0.152 m intervals. To assign reservoir properties to regions within the RRM models, average Kv and porosity values were calculated per unit. For example, if a modeled layer within the B zone corresponds to 40 measured intervals in the dataset, the average of those 40 values was used to define the Kv and porosity of that layer in the model.
Justification: By taking average values per layer or architectural element, the model attempts to stay as realistic as possible while reducing complexity. This approach captures the representative properties of each unit without overfitting to local variability, thereby simplifying the model and ensuring its usability within the generic framework of this study. Additionally, using individual values at fine scale (e.g., 0.152 m intervals) would lead to an excessively complex geological model in RRM, making both sketching and simulation computationally impractical. Averaging therefore reflects a necessary trade-off between geological detail and model performance, aligned with the capabilities and intended resolution of the software.

Assumption 9: Property Assignment Based on Channel Volume in the A and C1 Zones
In the channel-dominated A and C1 zones, four different channel types are distinguished, each with varying

volumes. For each channel type, average vertical permeability (Kv) and porosity values were calculated and assigned based on the relative volume the channel occupies within the zone. Specifically, the channel with the highest volume is assigned the highest permeability and porosity values, while the channel with the smallest volume receives the lowest values.
Justification: This approach ensures that the heterogeneity within the channel systems is represented while maintaining a manageable level of complexity. It provides a practical method to incorporate spatial variability in reservoir quality without overcomplicating the model, aligning with the simplified yet representative nature of this study.

Assumption 10: Uniform Reservoir Properties Assigned to All Interpreted Crevasses
Within the well log of the B zone, a crevasse deposit was identified at a specific depth, where notably high vertical permeability (Kv) and porosity values were measured. In the model, all interpreted crevasse elements across the relevant zones (B and C2) are assigned the same reservoir properties as observed at this location.
Justification: Using property values taken directly from the available dataset ensures that the model is grounded in real, measured data for this specific architectural element. While it's acknowledged that some variation likely exists across the field, applying a consistent set of known values provides a reliable and practical basis for the modelling. Given that both the B and C2 zones were deposited in similar fan front environments (as outlined in the Conceptual Model chapter), it is reasonable to expect that crevasse features in both zones share comparable reservoir characteristics. This makes it justifiable to apply the same property values across both zones for crevasse elements.

Assumption 11: Uniform Reservoir Properties Assigned to All Interpreted Channels
Within the well log of the C2 zone, a channel deposit was identified at a specific depth, where notably high vertical permeability (Kv) and porosity values were measured. In the model, all interpreted crevasse elements across the relevant zones (B and C2) are assigned the same reservoir properties as observed at this location.
Justification: Using property values taken directly from the available dataset ensures that the model is grounded in real, measured data for this specific architectural element. While it's acknowledged that some variation likely exists across the field, applying a consistent set of known values provides a reliable and practical basis for the modelling. Given that both the B and C2 zones were deposited in similar fan front environments (as outlined in the Conceptual Model chapter), it is reasonable to expect that channel features in both zones share comparable reservoir characteristics. This makes it justifiable to apply the same property values across both zones for channel elements.

Assumption 12: Uniform Porosity Assigned to All Top A Channel Types
In the model, all four channel types within the Top A zone have been assigned the same porosity value.
Justification: This decision was made because the variation in measured porosity across these channels is minimal. Assigning a single value avoids adding unnecessary complexity to the model while still remaining representative of the available data. It also improves clarity during analysis by reducing the number of parameters that vary within this zone.

Assumption 13: Exaggerated Element Dimensions for Modelling Purposes
In the model, architectural elements such as channels and crevasse splays are sketched slightly larger than they are likely to be.
Justification: This was done to simplify the model and ensure that key depositional features are clearly represented, even if they may be more vertically stacked or thinner in the actual subsurface. The approach allows the model to test for potential vertical crossflow between elements when they are in contact, which supports the study's focus on connectivity. Despite the simplified geometry, the model still reflects the presence of these features in the area and remains consistent with the generic modelling approach.

Assumption 14: Fixed Properties for the A, C1, and C3 Zones Across All Scenarios
In all modelling scenarios, the A, C1, and C3 zones are kept constant in terms of geometry and reservoir properties. No internal variation is introduced between scenarios.
Justification: The focus of this study is to evaluate whether vertical crossflow between the A and C1 zones (and to a lesser extent, the C3 zone) is possible through the overlying or underlying units, particularly the B and C2 zones. Given that the A and C1 zones are already known to exhibit good reservoir quality and internal connectivity, varying their properties would not significantly impact the outcome (ONE-Dyas internal information). By keeping these zones fixed, the model isolates and highlights the role of the B and C2 zones in

either enabling or restricting vertical connectivity.

Assumption 15: Consistent Mud Layer Distribution in the B Zone Across All Scenarios
In all scenarios, the consistent mud rich layers within the B and C2 zones are assumed to be laterally continuous and consistent.
Justification: This assumption is supported by porosity and vertical permeability (Kv) data from well logs, as well as well correlations from nearby wells provided by ONE-Dyas. Several intervals in the B zone display no significant fluctuations in porosity or Kv, suggesting with high confidence that no permeable architectural elements (such as channels or crevasses) are present in those intervals. Based on this evidence, it is considered reasonable to model the mud layers as continuous across the zone.

Assumption 16: Uniform water saturation across the entire model
Justification: The initial water saturation values at the start of gas production in 1990 are unknown due to missing historical data. To avoid introducing uncertain variations that could bias the simulation results, a uniform water saturation is applied throughout the model. This approach ensures consistency and simplifies interpretation, especially when testing the influence of other parameters such as capillary pressure and permeability.

Assumption 17: Constant production rate of 100,000 m^3/day during production periods
Justification: Detailed production data for the B well are incomplete or unavailable. Therefore, a representative and moderate gas production rate of 100,000 m^3/day is assumed to maintain model stability. Given that the simulation model represents a scaled-down version of the actual reservoir, using significantly higher production values would result in unrealistic pressure depletion or imbalance within the model.

Assumption 18: Only the C1 and C3 zones are perforated; the A zone is left unperforated
Justification: Although the actual well is perforated in the A, C1, and C3 zones, this setup is intentionally simplified to isolate and test the potential for stratigraphic vertical recharge. By only perforating the C1 and C3 zones, a pressure gradient can develop between A and C1, promoting potential upward flow through the B zone. This setup allows for focused investigation of stratigraphic connectivity while remaining grounded in the geological reality of the field.

Assumption 19: Zones are assigned distinct rock types based on lithological and petrophysical properties
Justification: Different zones in the model exhibit varying degrees of sand content, porosity, and permeability, justifying the use of multiple rock types. Zones A and C3 share similar sedimentary characteristics and property ranges and are therefore assigned the same rock type. The C1 zone is modeled as a separate rock type. The B and C2 zones both show high-sand and mud-rich layers; to reflect its heterogeneity, two rock types are defined for each: one for the layer with better properties and sand input and another for shale- or mud-dominated, lower-permeability intervals. This approach improves the realism of flow pathways and capillary behavior across the model.

Assumption 20: Capillary pressure curves are scaled by CMG in the base case simulations
Justification: This was done to simplify the model setup and to isolate the effects of petrophysical parameters such as permeability and porosity on flow behavior. By allowing CMG to scale the capillary pressure curves automatically, the model maintains vertical equilibrium internally without the need for detailed manual calibration. This ensures consistent initialization and allows for a clearer interpretation of the influence of other variables.

Assumption 21: Gas relative permeability (krg) remains greater than zero for all water saturations (SW $<$ 1.0) in the base case simulations
Justification: By setting the residual gas saturation (Sgr) to zero, gas mobility remains active across the full water saturation range. This allows for a clearer assessment of how changes in water saturation affect gas flow

velocity. Since krg decreases with increasing SW, this setup ensures that the impact of water saturation on gas mobility can be continuously observed without being limited by immobile gas at high saturations.

10.3 Methodology Steps

The following steps are taken in order to construct and run the simulations in this study: - Determine depositional environment of the Upper Slochteren zones (literature) - Determine present architectural elements (literature) - Determine the horizontal and vertical spatial configuration of architectural elements (literature) - Construct base model and divide the zones based on well log (RRM) - Construct and divide the model into continuous and non-continuous layers (RRM) - Construct the different scenarios based on vertical connectivity (RRM) - Assign permeability and porosity values to the different regions (RRM) - Determine the grid size (RRM) - Transfer the grid from .grdecl file to RESCUE file (Petrel) - Open RESCUE file containing information about the architecture, permeability and porosity in CMG (CMG) - Add parameters (28) - Run the models (CMG)

10.4 Pressure and Water Saturation Basecase Results CMG

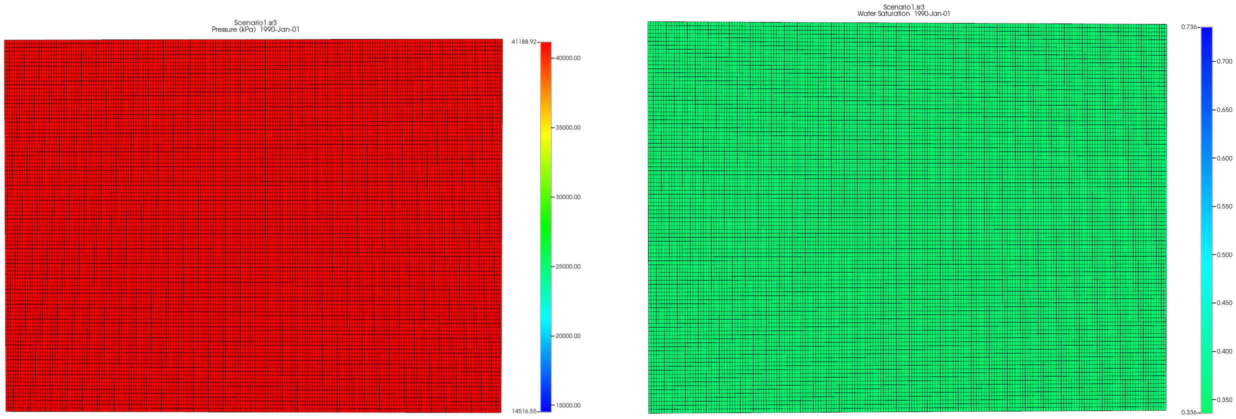

(a) Screenshot of the pressure distribution at the start of the simulation of scenario 1. The pressure distribution is equal for all scenarios at the start, thus applies to all scenarios

(b) Screenshot of the water saturation at the start of the simulation of scenario 1. The water saturation is equal for all scenarios at the start, thus applies to all scenarios

Figure 97: Screenshots of the initial pressure (a) and water saturation (b) setting in all scenarios

10.4.1 Scenario 1

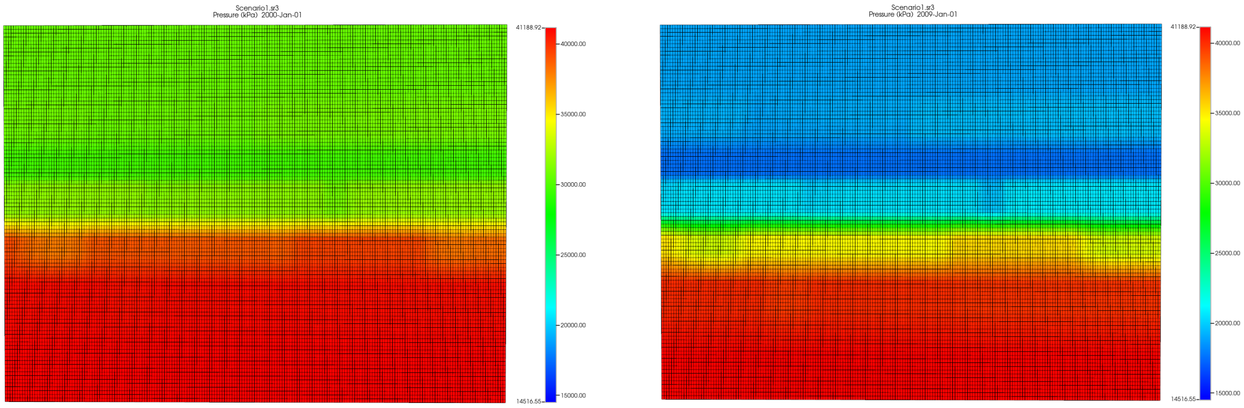

(a) Screenshot of the pressure distribution of scenario 1 at 01-01-2000.

(b) Screenshot of the pressure distribution of scenario 1 at 01-01-2009, at this date, the well is shut-in.

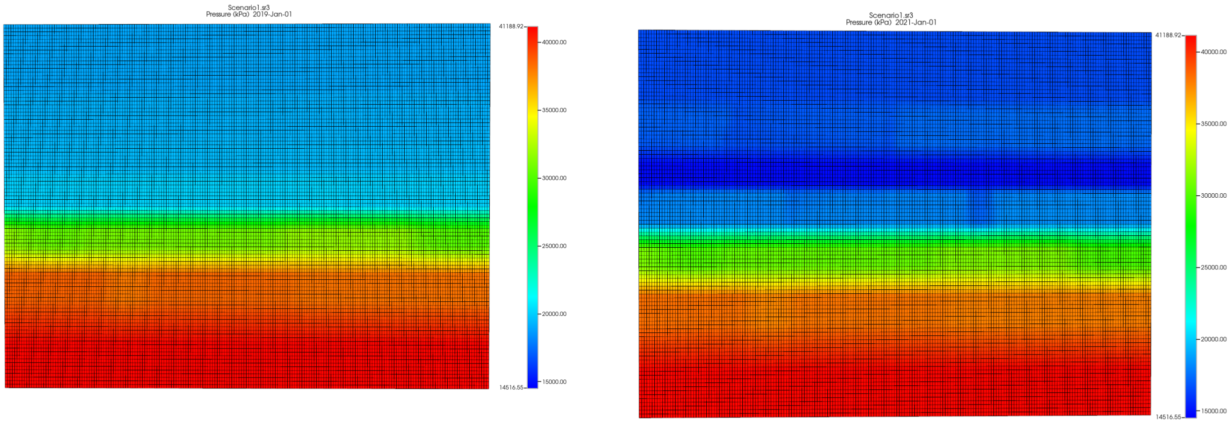

(c) Screenshot of the pressure distribution of scenario 1 at 01-01-2019, when production starts again after shut-in period of 10 years.

(d) Screenshot of the pressure distribution of scenario 1 at 01-01-2021.

Figure 98: Screenshots of the pressure distribution over time in basecase scenarios 1 in 2000 (a), 2009 (b), 2019(c), and 2021 (d)

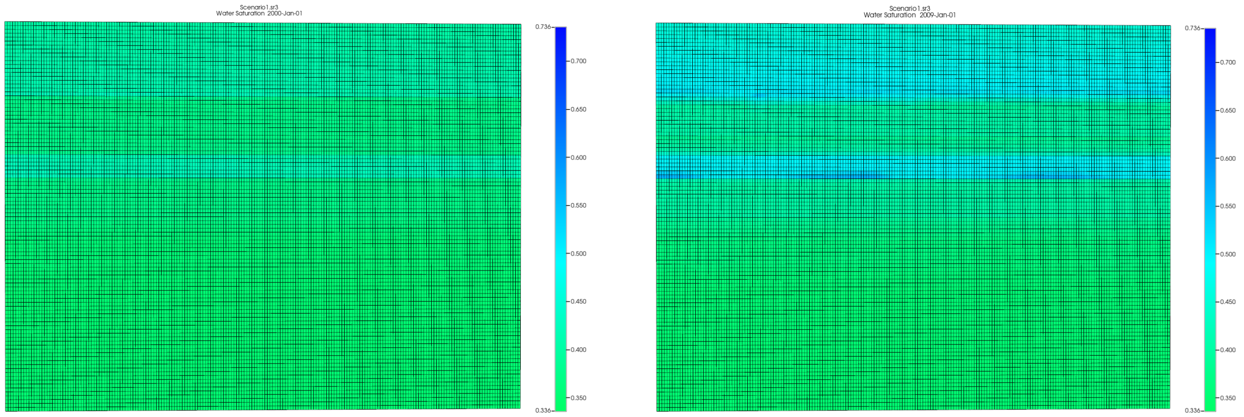

(a) Screenshot of the water saturation distribution of scenario 1 at 01-01-2000

(b) Screenshot of the water saturation distribution of scenario 1 at 01-01-2009, at this date, the well is shut-in

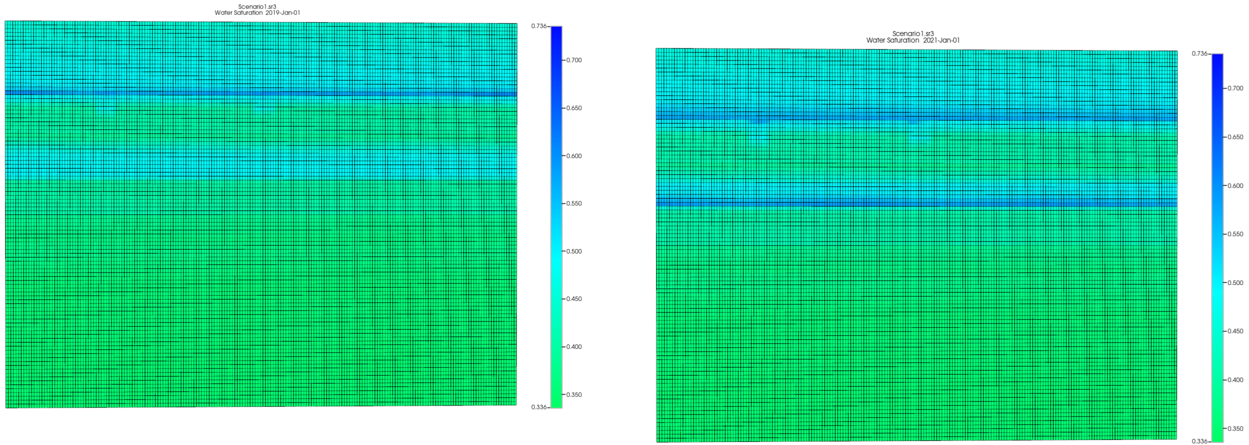

(c) Screenshot of the water saturation distribution of scenario 1 at 01-01-2019, when production starts again after shut-in period of 10 years.

(d) Screenshot of the water saturation distribution of scenario 1 at 01-01-2021.

Figure 99: Screenshots of the water saturation distribution over time in basecase scenarios 1 in 2000 (a), 2009 (b), 2019(c), and 2021 (d)

10.4.2 Scenario 2

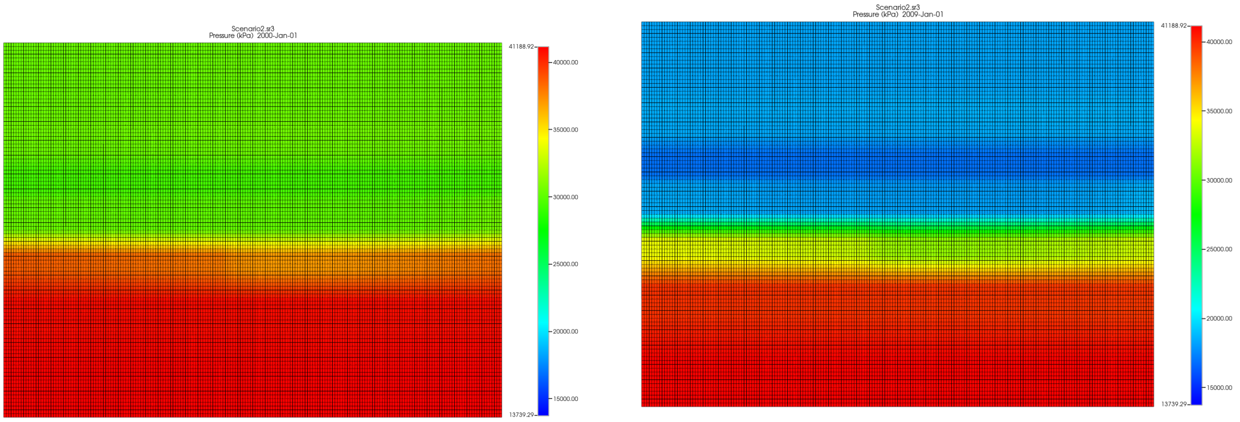

(a) Screenshot of the pressure distribution of scenario 2 at 01-01-2000.

(b) Screenshot of the pressure distribution of scenario 2 at 01-01-2009, at this date, the well is shut-in.

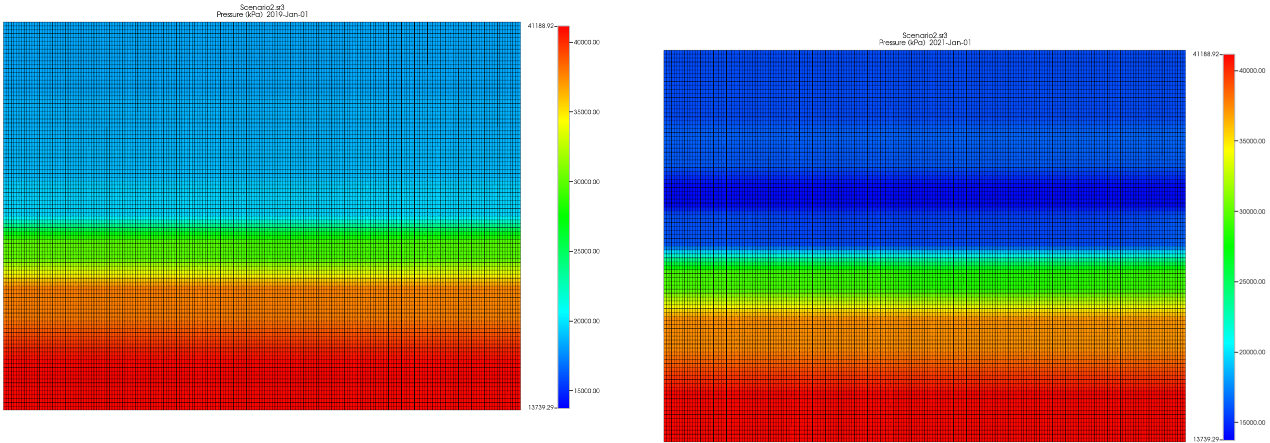

(c) Screenshot of the pressure distribution of scenario 2 at 01-01-2019, when production starts again after shut-in period of 10 years.

(d) Screenshot of the pressure distribution of scenario 2 at 01-01-2021.

Figure 100: Screenshots of the pressure distribution over time in basecase scenarios 2 in 2000 (a), 2009 (b), 2019(c), and 2021 (d)

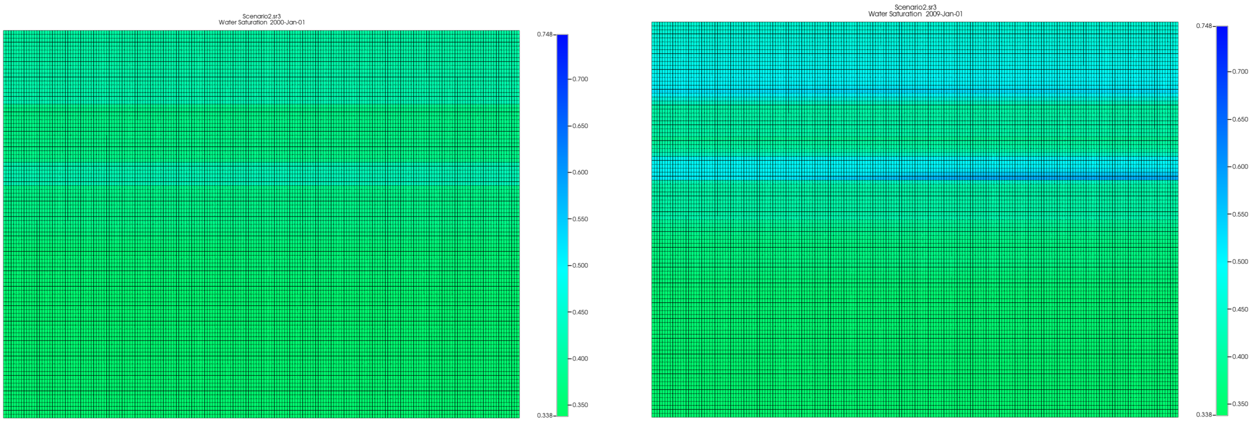

(a) Screenshot of the water saturation distribution of scenario 2 at 01-01-2000

(b) Screenshot of the water saturation distribution of scenario 2 at 01-01-2009, at this date, the well is shut-in

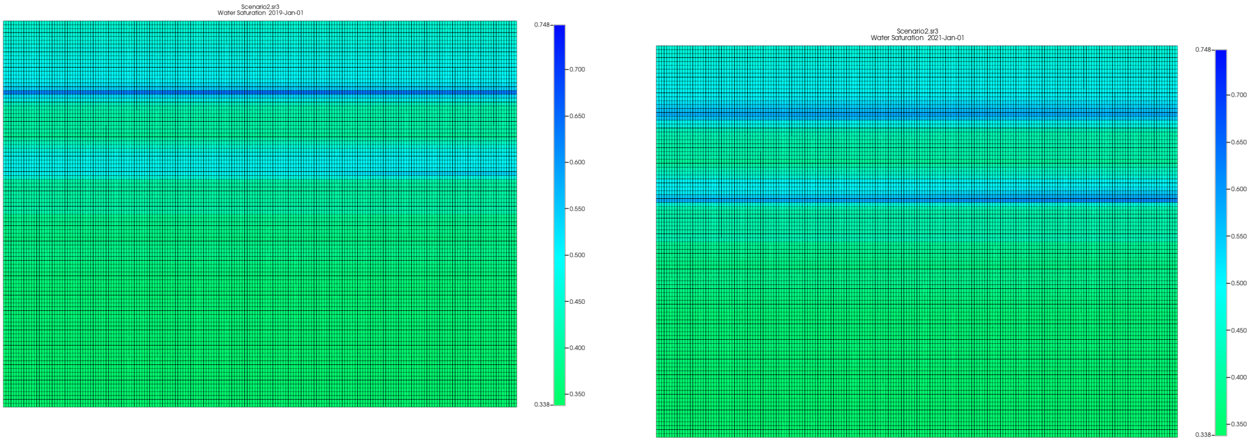

(c) Screenshot of the water saturation distribution of scenario 2 at 01-01-2019, when production starts again after shut-in period of 10 years.

(d) Screenshot of the water saturation distribution of scenario 2 at 01-01-2021.

Figure 101: Screenshots of the water saturation distribution over time in basecase scenarios 2 in 2000 (a), 2009 (b), 2019(c), and 2021 (d)

10.4.3 Scenario 3

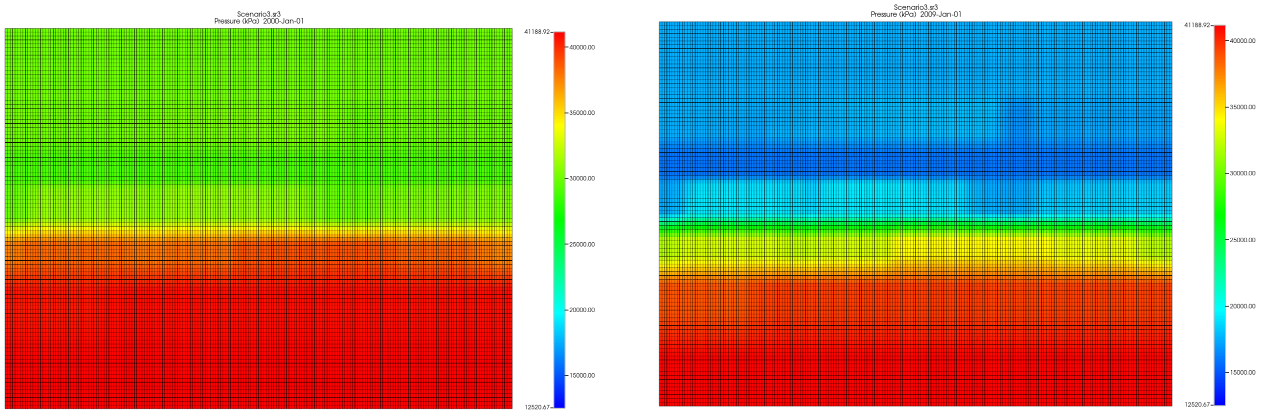

(a) Screenshot of the pressure distribution of scenario 3 at 01-01-2000.

(b) Screenshot of the pressure distribution of scenario 3 at 01-01-2009, at this date, the well is shut-in.

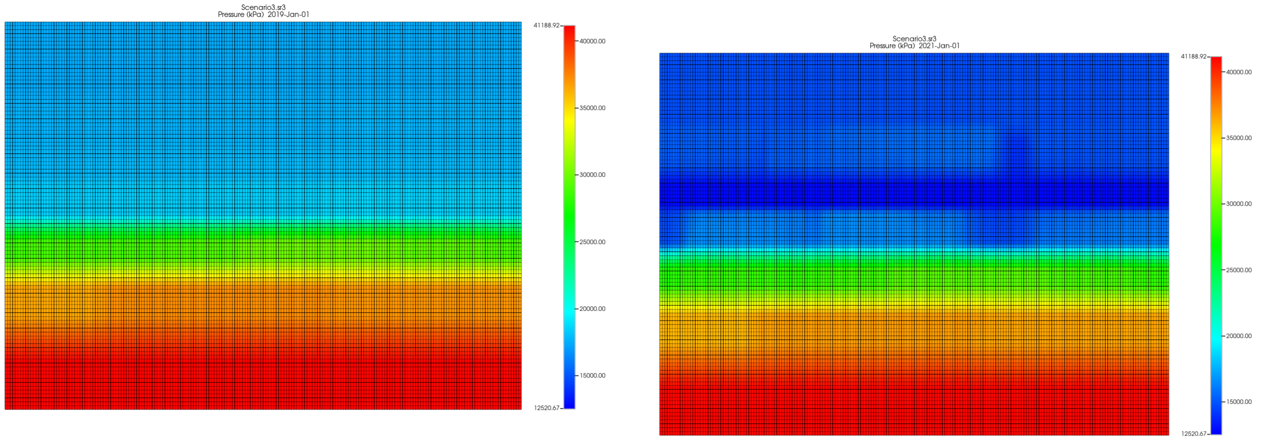

(c) Screenshot of the pressure distribution of scenario 3 at 01-01-2019, when production starts again after shut-in period of 10 years.

(d) Screenshot of the pressure distribution of scenario 3 at 01-01-2021.

Figure 102: Screenshots of the pressure distribution over time in basecase scenarios 3 in 2000 (a), 2009 (b), 2019(c), and 2021 (d)

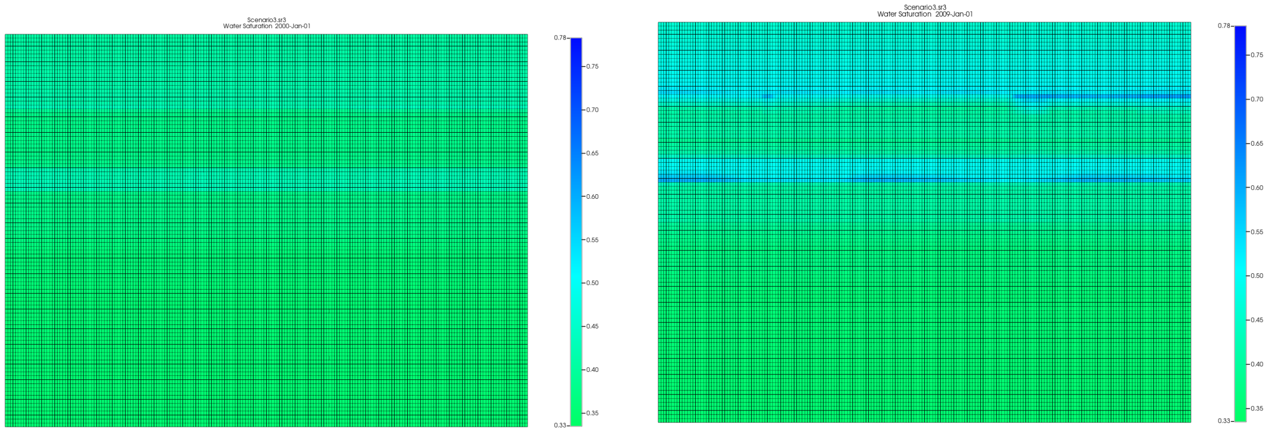

(a) Screenshot of the water saturation distribution of scenario 3 at 01-01-2000

(b) Screenshot of the water saturation distribution of scenario 3 at 01-01-2009, at this date, the well is shut-in

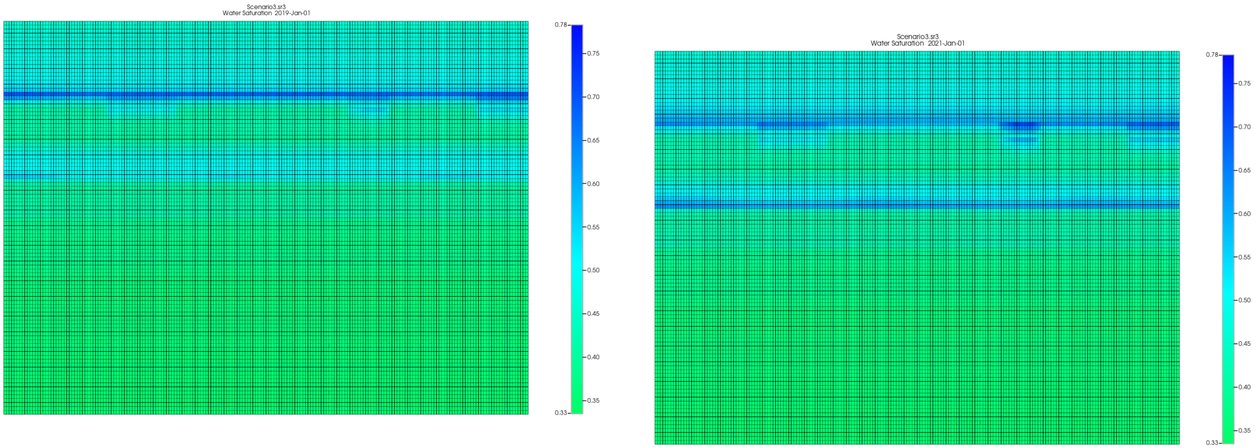

(c) Screenshot of the water saturation distribution of scenario 3 at 01-01-2019, when production starts again after shut-in period of 10 years.

(d) Screenshot of the water saturation distribution of scenario 3 at 01-01-2021.

Figure 103: Screenshots of the water saturation distribution over time in basecase scenarios 3 in 2000 (a), 2009 (b), 2019(c), and 2021 (d)

10.4.4 Scenario 4

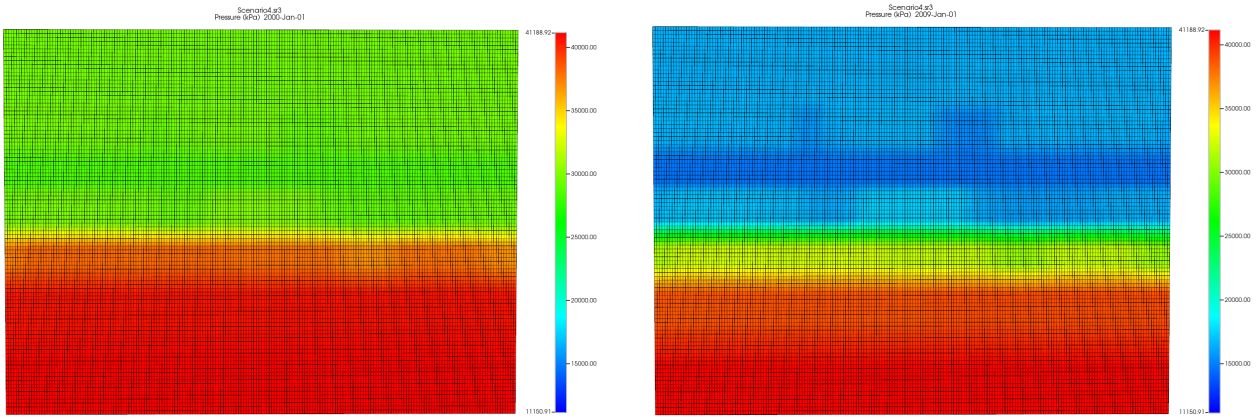

(a) Screenshot of the pressure distribution of scenario 4 at 01-01-2000.

(b) Screenshot of the pressure distribution of scenario 4 at 01-01-2009, at this date, the well is shut-in.

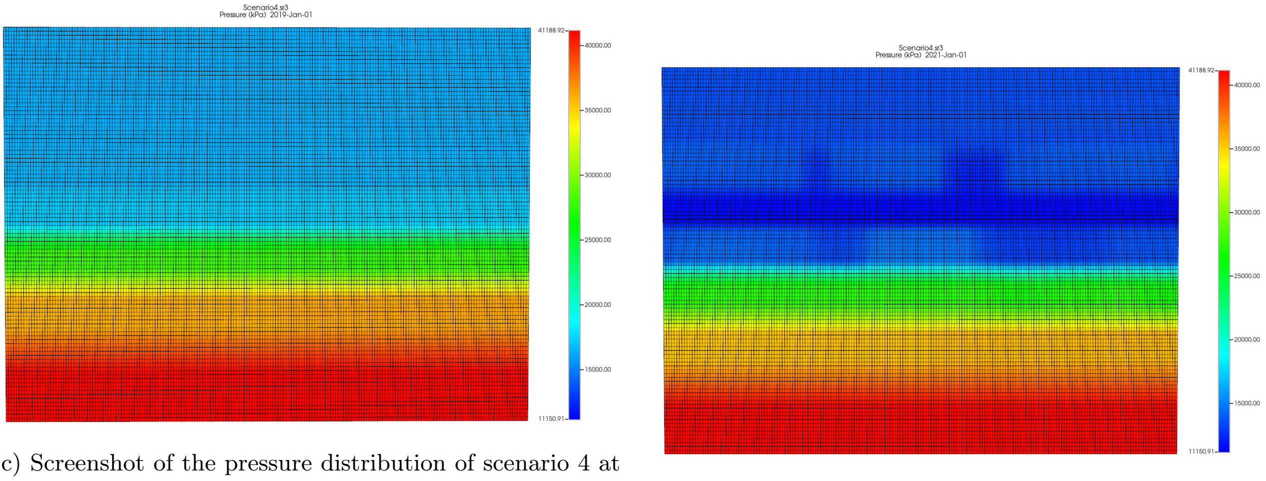

(c) Screenshot of the pressure distribution of scenario 4 at 01-01-2019, when production starts again after shut-in period of 10 years.

(d) Screenshot of the pressure distribution of scenario 4 at 01-01-2021.

Figure 104: Screenshots of the pressure distribution over time in basecase scenarios 4 in 2000 (a), 2009 (b), 2019(c), and 2021 (d)

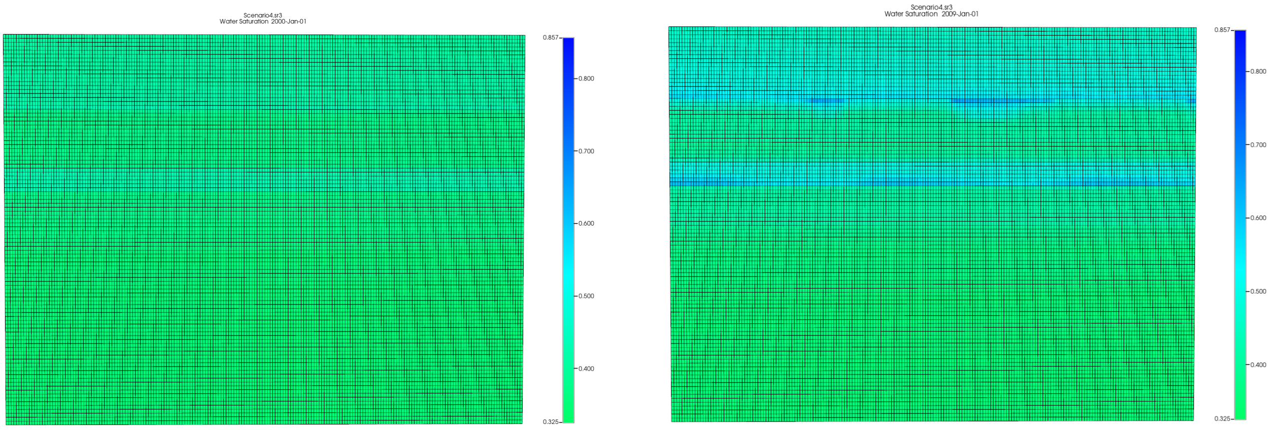

(a) Screenshot of the water saturation distribution of scenario 4 at 01-01-2000

(b) Screenshot of the water saturation distribution of scenario 4 at 01-01-2009, at this date, the well is shut-in

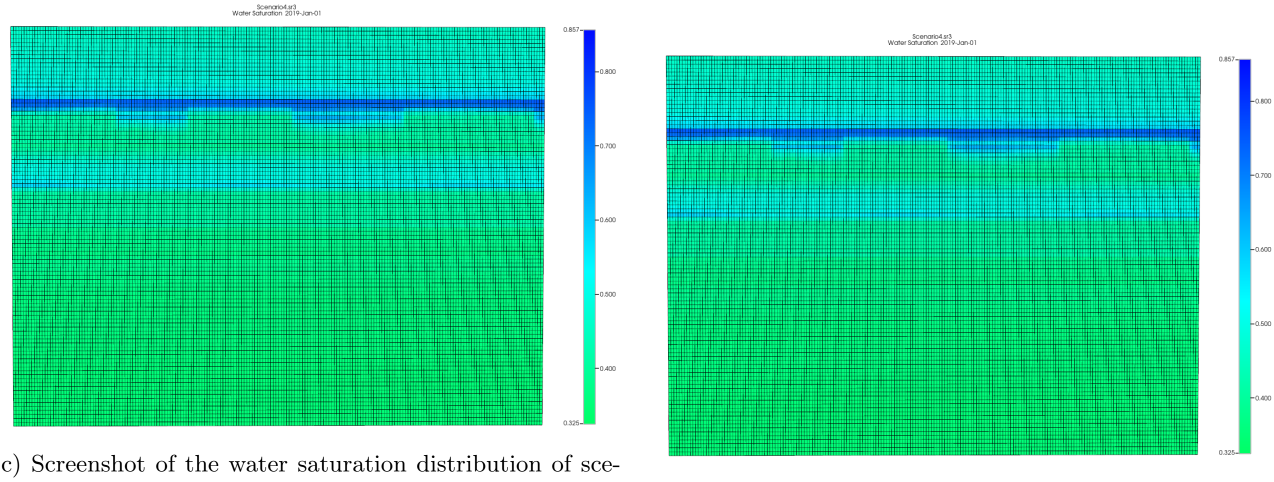

(c) Screenshot of the water saturation distribution of scenario 4 at 01-01-2019, when production starts again after shut-in period of 10 years.

(d) Screenshot of the water saturation distribution of scenario 4 at 01-01-2021.

Figure 105: Screenshots of the water saturation distribution over time in basecase scenarios 4 in 2000 (a), 2009 (b), 2019(c), and 2021 (d)